Isolated T Tauri Stars Toward the Taurus-Auriga Star Forming Region

Satoshi TAKITA

Department of Space and Astronautical Science,
School of Physical Sciences,
The Graduate University for Advanced Studies

January 4, 2011

Acknowledgements

First of all, I would like to thank my supervisor, Hirokazu Kataza, for always giving me advices and opportunity to make this kind of study. His great knowledge on astronomy and critical comments always improved my study. Without his instructive advice, I would hardly have finished this thesis. I am very grateful my sub-supervisor, Issei Yamamura for supporting my work. I thank Yoshimi Kitamura for their instructive advice on this work. I also acknowledge the collaborators, Munetaka Ueno, Akiko Kawamura, Daisuke Ishihara, Shinki Oyabu, Yoshifusa Ita, Hideaki Fujiwara, and Takafumi Kamizuka. I thank Mitsuhiko Honda, Yoshiko K. Okamoto, and Takashi Onaka for their scientific advice. I also appreciate Norio Ikeda and Chisato Yamauchi for their suggestive comments about data handling and programming techniques. And, I would like to thank all of the members of Department of Infrared Astrophysics/Institute of Space and Astronautical Science. Finally, I wish to thank my family for their support in both mental and financial ways.

Abstract

It is fundamental to investigate the origin of low-mass stars and planets in order to answer how the Sun and the Earth were formed. Many surveys of young stellar objects (YSOs) have been performed toward molecular clouds in wide wavelengths range from optical to radio wavelengths. On the other hand, substantial amount of weak-line T Tauri stars (WTTSs) have been found far away from active molecular clouds by the X-ray observations. This indicates that many isolated T Tauri stars (TTSs) are thought to be still unexplored. Therefore, unbiased survey of YSOs are required in order to understand star formation process. For this purpose, we have carried out a survey of TTSs with the all-sky survey data by the Japanese infrared astronomical satellite, AKARI.

The first step of our observational study is the survey of isolated TTSs at mid-infrared (MIR) wavelengths with the AKARI All-Sky Survey. Since TTSs exhibit infrared excess emission from circumstellar disks, we first studied previously known TTSs to perceive what colours do TTSs show. Among 516 previously known TTSs laying in a 1800-square-degree region around the Taurus star forming region, we detected 132 TTSs in the MIR. To construct more complete data sets, we also used other all-sky surveys such as 2MASS (the Two-Micron All-Sky Survey; near-infrared (NIR) wavelengths) and UCAC3 (the third US Naval Observatory (USNO) CCD Astrograph Catalogue; optical wavelengths). It is indispensable to distinguish TTSs from possible contamination of other types of objects such as Asymptotic Giant Branch (AGB) stars (carbon and OH/IR stars), post-AGB stars, planetary nebulae (PNe), as well as galaxies, that also show infrared excess emission. Using the MIR colour, we discarded most of AGB stars from the sample. We also separated most of galaxies from TTSs using the colour-magnitude diagram of optical–NIR wavelengths data. Finally, we extracted TTS candidate sources with IR excess emission, avoiding contamination from normal (main-sequence) stars, which do not present excess emission. About 40% and 5% of AKARI detected known Classical T Tauri stars (CTTSs) and Weak-line T Tauri stars (WTTSs) satisfy these criteria, respectively. On the basis of our criteria, we selected 176 out of 14 725 AKARI sources toward the Taurus region. There are 150 previously known sources, and 117 of them (about 80%) are YSOs including other star forming regions near the Taurus. The remaining 26 sources are newly found TTS candidates. We performed follow-up optical spectroscopic observations for these sources to determine their youth from Li I absorption line. We confirmed that 23 out of 27 (including 1 possible binary) sources have sufficient Li absorption to be classified as TTSs. This validate the usefulness of our criteria. From the line width of Hα emission, we classified 23 new TTSs into 15 CTTSs and 8 WTTSs. We obtained 9 new isolated CTTSs

and 6 new isolated WTTSs. There are only 8 isolated CTTSs previously, and we increased the number of them to 17.

We found that the origin of most of isolated TTSs is most probably small clouds around the Taurus molecular cloud, from their proper motions determined by UCAC3. For the 23 new TTSs, at least 5 sources seem not to be related to known star forming regions, considering their spatial distributions and directions of proper motions. Furthermore, the dispersion of known/new TTSs' proper motions is $\sim$15 km s^{-1}. This value far exceeds the typical value of $\sim$1 km s^{-1}, for the case that sources were originated from a cloud with size of $\sim$1 pc. This fact suggests that not all TTSs were born in the molecular cloud cores which were gravitationally bound to the Taurus molecular cloud. If TTSs were formed in not only the Taurus molecular cloud but also small clouds which do not relate to the Taurus, the large velocity dispersion is thought to come from the inter-cloud velocity dispersion. We investigated the HI clouds in the region, and found that the dispersion in radial velocity of the clouds is $\sim$12 km s^{-1}, comparable to the dispersion of the TTS proper motion. Considering that the molecular clouds are formed from HI clouds, inter-cloud velocity dispersion of molecular clouds is expected to be similar, and stars originated from these clouds are also expected to show large velocity dispersion.

We also verify whether there are any differences between TTSs associated to active clouds and those isolated from clouds. The CTTS/WTTS ratios of AKARI detected TTSs are 81/31 and 12/16 for inside and outside the clouds, respectively. If we consider the typical age of a CTTS ($\sim$1 Myr) and WTTS ($\sim$10 Myr), TTSs associated to the clouds seem to be relatively young. We determined disk masses using the AKARI far-infrared data, and found no remarkable difference. We further classified AKARI detected TTSs with their slopes of the SED in the NIR–MIR wavelengths into three kinds of sources; those with envelopes, with disks, and without surrounding materials. For TTSs in our sample and associated to clouds, about a quarter of them have envelopes and a few % of them are naked. On the other hand, for isolated TTSs, a few % of them have envelopes and about one third of them are naked. This also supports the idea that TTSs associated to the clouds are relatively younger than those isolated from the clouds.

We conclude that most of isolated TTSs toward the Taurus were born in isolated small clouds. Considering the fraction of known TTSs, about 30% of TTSs toward the Taurus were born as isolated. This implies that the star formation in small isolated clouds occupies significant fraction in the low-mass star formation activity. We find that circumstellar disks of isolated TTSs are more evolved than those of associated TTSs.

Contents

Chapter 1

INTRODUCTION

1.1 Scenario for Low-Mass Star Formation

Stars are the fundamental constituents of the universe, and hence understanding the star formation process is one of the most important issues in astronomy. The star formation occurs in molecular clouds which consists of molecular gas and dust. The typical clouds have size of $\sim$10–100 pc, mass of 10^3–10^5 $M_\odot$, and density of 10^2–10^3 cm^{-3}. Inside the clouds, there are relatively dense regions with densities of 10^3–10^5 cm^{-3} and sizes of $\sim$1 pc, which are called clumps. Furthermore, the clumps consists of several denser condensations, which are called molecular cloud cores or prestellar cores, with densities of 10^5–10^6 cm^{-3} and sized of $\sim$0.1 pc. New stars are thought to be born through the gravitational collapse of the cores. The overall star formation is roughly classified into the two modes of the 'isolated star formation' and the 'cluster formation'. In the first case, a star with a mass less than a few $M_\odot$ spontaneously forms from an isolated core, as in the Taurus molecular cloud. In the second case, many stars with masses of 0.1–30 $M_\odot$ simultaneously form as a cluster in a clump, as in the Orion molecular cloud. Although almost all the stars (more than 90%) in our Galaxy are thought to form as clusters (Lada et al. 1991), 'cluster formation' is less understood due to the large distance, small numbers of high mass stars, and the short lives of high mass stars.

The most successful scenario for isolated low-mass star formation is illustrated as follows (see Figure 1.1). After the collapse of molecular cloud cores, the protostellar nucleus is formed at the centre, and the inside-out collapse of the core gas is predicted to occur in the free-fall time-scale. In this earliest stage, the central protostar is classified as a Class 0 object on the basis of the shape of Spectral Energy Distribution (SED); since the Class 0 source is typically obscured by the dense circumstellar gas and dust, the stellar emission cannot penetrate the core, and as a result, the SED of the Class 0 source becomes a cold blackbody-like spectrum with a peak at sub-millimetre wavelengths. The lifetime of the Class 0

stage is estimated to be $\sim 10^4$ years, which is one order of magnitude shorter than the free-fall time of the core. At this stage, in addition to the mass infall, energetic jet and outflow are also launched.

After the infall of a major fraction of the core material towards the central protostar, the protostar is classified as a Class I object, whose lifetime is estimated to be $\sim 10^5$ years, which is comparable to the free-fall time of the core. At this stage, the protostar usually has disk-like envelopes with size of a few $\times$ 1000 AU, and outflow in the polar directions. Since the emission from the envelope is dominant, the SED of Class I becomes hotter than that of Class 0. One of the most important roles of the outflow is to carry away the angular momentum from the prestellar core to advance the mass accretion into the central protostar. On the other hand, owing to the slow rotation of the prestellar cores, a disk with radii of $\sim$100 AU form at the centre of the infalling envelope. The core material does not directly accrete to the central star, but lands on the disk through the envelope, and finally accretes on to the central star.

After almost all the core material falls into the disks or are swept away by the outflow, the central star with the disk becomes visible at optical wavelengths. This object is classified as a Classical T Tauri Star (CTTS), or a Class II object. The circumstellar disk is thought to be in the turbulent state (i.e., accretion disk), and the mass accretion to the central star continues through the disks. The SED of Class II consists of the stellar blackbody radiation and the thermal emission from its disk at Near-Infrared (NIR) to millimetre wavelengths. The lifetime of this stage is $\sim 10^6$ years.

In the next stage, the central star is classified as Weak-line T Tauri Star (WTTS) or a Class III object. During this stage, the disk material is thought to be consumed for building planets, and the disks are mostly dissipated. The SED of Class III is almost equal to the blackbody with a stellar temperature. The lifetime of WTTSs is $\sim 10^7$ years, i.e., the Kelvin-Helmholtz time-scale which is an estimate of how long a given star would shine by releasing its gravitational potential. After this stage, the central star becomes a main-sequence (MS) star, and the nuclear fusion occurs in the innermost part of the star.

1.1.1 Circumstellar Disk around TTS

The pioneering studies of the disks are the IRAS (the Infrared Astronomical Satellite) and millimetre continuum surveys towards the Taurus-Auriga region (Strom et al. 1989, Beckwith et al. 1990). Strom et al. (1989) reported about a half of CTTSs have the excess emission at the infrared wavelengths stronger than that expected from their photosphere. The excess emission is well explained as the thermal emission from the circumstellar disks heated by the central stars. This discovery demonstrated that the disks are common around young stars. Beckwith et al. (1990) also found that a similar fraction of stars have the excess emission at the 1.3 mm wavelength, and derived the disk masses ranging from

0.001 to 0.1 $M_\odot$. The mass range strongly supports the minimum-mass solar nebula, which is a total mass of solar composition material that would be needed to produce the observed material in the planets (Hayashi et al. 1985). Kitamura et al. (2002) performed an imaging survey of the protoplanetary disks around single T Tauri stars with 2 mm continuum emission. They found the radial expansion of the disks with decreasing Hα luminosity, a clock for the disk evolution, and diversity in the physical properties of the disks.

At the next WTTS phase, the disk emission becomes too weak to be detected with the current telescopes. Since the age of the WTTSs is of the order of 10 Myr, when theoretically predicted phase that the planet formation occurs, it is important to understand the disk properties around WTTSs with $\sim$10 Myr. After the launch of Spitzer (the Spitzer Space Telescope), many surveys for searching disks have been performed. The two Spitzer Legacy project, FEPS (the Formation and Evolution of Planetary Systems) and c2d (From Molecular Cores to Planet Forming Disks), have surveyed many PMS stars (Silverstone et al. 2006, Padgett et al. 2006, Cieza et al. 2007). From the FEPS survey, 5/74 young stars (3–30 Myr) have the strong (near-)IR excess, but 4 of which have the ages of 3–10 Myr (Silverstone et al. 2006). Padgett et al. (2006) and Cieza et al. (2007) observed more than 300 TTSs, and found that $\sim$20% of the WTTSs have the IR excess emission at the wavelengths of 3.6–8.0 μm, but no IR excess for the stars older than 10 Myr. Consequently, it is shown that the disk dissipation time scale is about 10 Myr.

1.2 Surveys and Spatial Distributions of YSOs

In the previous section, we showed the overview of the star and planet formation process and the classification of a Young Stellar Object (YSO) based on the SED. In this section, we mention the spatial distribution of YSOs.

Since star formation occurs in molecular clouds, many YSOs are discovered inside the clouds. Protostar was first found by its strong infrared (2.2–20 μm) emission (Mendoza & Eugenio 1966, Becklin & Neugebauser 1967). Many observations have been done for surveying protostars toward molecular clouds owing to the improvements in infrared detector technology. The IRAS discovered many infrared sources with SEDs peaking at 60–100 μm, i.e., protostars (Beichman et al. 1986). A T Tauri star was originally identified as a late-type star with strong emission lines and irregular light variations associated with dark or bright nebulosities. Most of these *classical* TTSs were discovered from Hα surveys toward dark clouds (e.g., Herbig & Bell 1988). Walter & Kuhi (1981) found another type of TTSs from an X-ray observations called as *weak-line* TTSs due to their weak Hα emission. The borderline of CTTS and WTTS is an Hα equivalent width of -10 Å. Furthermore, the Spitzer Space Telescope have found many low-luminous (or heavily embedded) protostars and TTSs, recently (e.g., Evans et al. 2009).

1.2.1 Isolated TTSs

Although many YSOs were discovered, these surveys were biased toward cloud region. However, Neuhäuser et al. (1995a) have found that substantial amount of WTTSs are sequestered in relatively wide area of $\sim 100°$ region including the Taurus-Auriga star forming region, using the X-ray observations of Roentgen Satellite (ROSAT). Many surveys of TTSs based on the ROSAT were carried out in nearby star forming regions such as the Taurus (Wichmann et al. 1996, Magazzù et al. 1997, Li & Hu 1998) and Chamaeleon (Alcala et al. 1995) (see Figure 1.2). These surveys found a large number of T Tauri stars. One of the interesting results of the X-ray selected TTS surveys is that a large number of TTSs have been found far away from the molecular clouds. This situation can be interpreted by following three ideas (Feigelson 1996).

- TTSs have moved with their proper motions of $\Delta v \sim$1 km s^{-1}, taking over the thermal velocity dispersions of the natal cloud gas. Feigelson (1996) suggested that if stars have an isotropic Gaussian velocity dispersion with $\Delta v \sim 1\,\mathrm{km\,s^{-1}}$, it is sufficient to explain the spacial distributions of the widely dispersed WTTSs. A star travelling 1 km s^{-1} in the plane of the sky can move 10 pc ($4\overset{\circ}{.}2$ at distance of 140 pc) in 10 Myr.

- TTSs were born in cloudlets or small clouds, and the cloudlets have already dissipated. Since substantial number of isolated WTTSs were known to be too young to move far away from active clouds, Feigelson (1996) suggested this second mechanism. The TW Hya group may be an example where the entire cloud has entirely disappeared.

- TTSs were dynamically ejected with high-velocity by gravitational interactions with other stars. Although this is the other idea for young stars appearing far from the cloud, it seems an unacceptable model because of the number of these kind of stars is expected too small.

So, how many stars are born in cloudlets or small clouds? If this is the case, number of isolated CTTSs should exist. Since only a few CTTSs were found, we cannot contradict that isolated CTTSs are dynamically ejected from active clouds.

1.3 Star Formation in Globules and Small Clouds

Although most star formation occurs in giant molecular clouds, numerous small clouds and Bok globules are now known to have a few young stars (Reipurth 2008). These small clouds and Bok globules are thought to be birthplaces of isolated TTSs. The distinction between a Bok globule and a small cloud is diffuse. The term 'globule' was named by Bok & Reilly (1947), for small ($\sim 10'$),

round, dense dark nebulae, which are seen in contrast against bright HII regions or background stars. Furthermore, a number of interesting star forming clouds, which are similar to Bok globules in size, also exist. Reipurth (2008) denoted these sources as 'small clouds'. In this thesis, we treat globules, small clouds, and cloudlets are the same one.

Many Bok globules are known across the sky, and small clouds are found even more commonly. Despite their numbers, these small objects are not an important contributor to the production of low-mass stars in our Galaxy, accounting for at most a few percent (Reipurth 1983). The importance of these regions lies mostly in their simplicity, which allows us to study the formation of one or a few stars without the confusion that often complicates observations of richer regions of star formation.

Observational pieces of evidences for star formation were shown as follows. Yun & Clements (1990) surveyed 248 Bok globules using IRAS coadded images and found that about 23% of Bok globules show evidence for associated point sources. Considering the sensitivity of the IRAS ($\sim$0.7 $M_\odot$) and the initial mass function, only about 20 % of the total number of stars cloud found. They therefore, noted that almost every Bok globule harbours a young star. Indeed, recent Spitzer observations discovered low-luminous protostars in many globules (e.g., Young et al. 2004). Wang et al. (1995) performed the $C^{18}O$ ($J = 2 - 1$) and H_2CO ($J_{K_{-1}K_1} = 3_{12} - 2_{11}$) line observations toward 40 Bok globules. They found that three of these globules have kinematic signatures for collapse. The sensitive NIR measurements of the background stars, as extinction, revealed the internal structure of Bok globules (e.g., Alves et al. 2001). Alves et al. (2001) found that cloud's density structure to be very well described by the equations for a pressure-confined, self-gravitating isothermal sphere that is critically stable according to the Bonnor-Ebert criteria (see Figure 1.3). From these facts, star formation in globules seems to occur ubiquitously.

1.4 Purpose of this Thesis

The main purpose of this study is to reveal that star formation in small clouds are generally occur. To testify this idea, we first expand the number of isolated CTTSs, using the AKARI All-Sky Survey. The advantages of this study against the previous studies of YSO survey, is that AKARI observed almost the whole sky. As noted before, previous YSO surveys were biased toward cloud region. Although ROSAT surveyed all-sky, the detection rate for previously known CTTSs was only $\sim$10%, and it was not complete. We, then, search the origin of the isolated TTSs from their proper motions. We also verify whether or not there are any differences between TTSs associated to active clouds and isolated from clouds.

In Chapter 2, we describe the specifications of the AKARI All-Sky Survey,

which most data used in this thesis. We show the input previously known TTSs, and how complete AKARI surveyed them. We perform a cross-correlation between the AKARI IRC Point source Catalogue, 2MASS catalogue (NIR wavelengths), and UCAC3 (optical wavelengths) to construct more complete data sets.

In Chapter 3, we present the results of the AKARI survey of previously known TTSs. We make some colour-colour and colour-magnitude diagrams for previously known TTSs using AKARI, 2MASS, and UCAC3 data, to determine what colours TTSs have. From these diagrams, we select new TTS candidate sources with similar characteristics of previously known TTSs. We also show the results of the follow-up observations of the new TTS candidates, and discuss whether or not they are TTSs.

In Chapter 4, we discuss the origin of isolated CTTSs. We also compare the properties between the TTSs associated to clouds and isolated TTSs.

In Chapter 5, we summarize this thesis.

1.5 Target Region

In this section, we introduce the Taurus-Auriga star forming region which is surveyed in this thesis.

The Taurus molecular cloud (Figure 1.4), located at a distance of $\sim$140 pc from the Sun, is one of the most typical low-mass star forming region and contains more than 300 young stars and brown dwarfs (Kenyon et al. 2008). Because of the low stellar density of only 1–10 stars pc^{-2} (e.g., Gomez et al. 1993), strong mutual influence due to outflows, jets, or gravitational effects are minimized. Furthermore, most stars in Taurus are subject to relatively modest extinction, providing access to a broad spectrum of stars at all evolutionary stages from Class 0 sources to post TTSs.

With no luminous O or B stars, the Taurus-Auriga dark clouds are mostly neutral and contain large amounts of mass, 3–4 $\times 10^4$ M$_\odot$. The observations at millimetre wavelengths showed filamentary structure, which was also observed in the optical wavelengths as extinction (e.g., Onishi et al. 2002). The radio observations reveal dense clumps and cores of molecular gas inside these structures with masses of 1–100 M$_\odot$.

The short distance and low density of Taurus also permitted spatially resolved photometry of individual stars at wide wavelength rage. By combining 12–100 μm photometry from the Infrared Astronomical Satellite (IRAS) and 1–10 μm data from ground-based telescopes, Kenyon & Hartmann (1995) performed the most comprehensive census of disks in a star-forming region at that time. They found that more than 50% of Taurus objects have IR excess emission, indicating the presence of warm circumstellar material predominantly in the form of envelopes for Class I protostars and circumstellar disks for Class II stars. The disk-bearing

stars have served as targets for a multitude of detailed observations of circumstellar disks.

The census of the stellar population of Taurus has expanded significantly since the disk study of Kenyon & Hartmann (1995), particularly at masses below 0.5 $M_\odot$. Owing to the drastic improvements of IR telescopes, for example the Spitzer Space Telescope, many Taurus members with masses below 0.01 $M_\odot$ were detected (e.g., Rebull et al. 2010, Luhman et al. 2010).

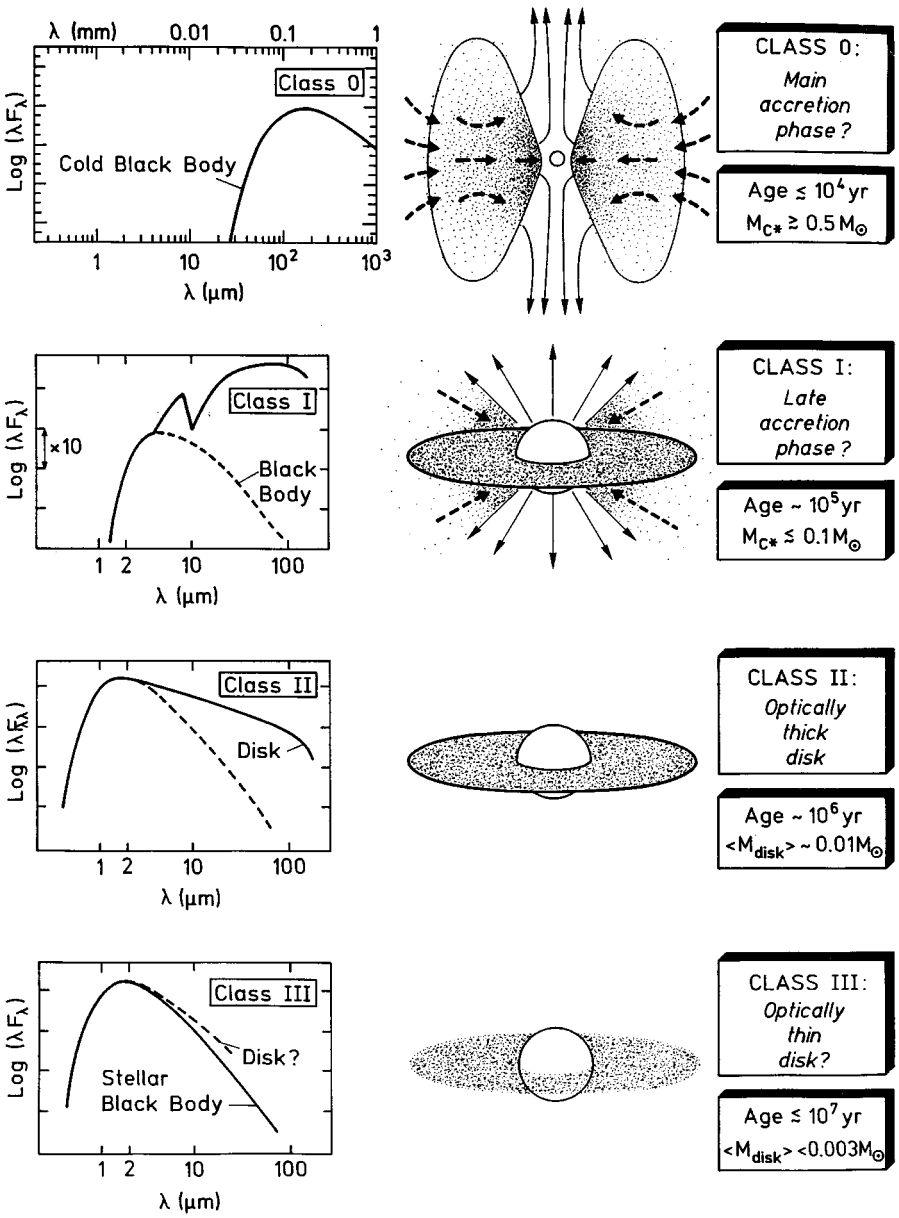

Figure 1.1: Scenario for low mass star formation as proposed by André (1994). The four classes 0, I, II, and III correspond to successive stages of evolution. The typical of visions, Spectral Energy Distributions, ages, and characteristics in each class are shown.

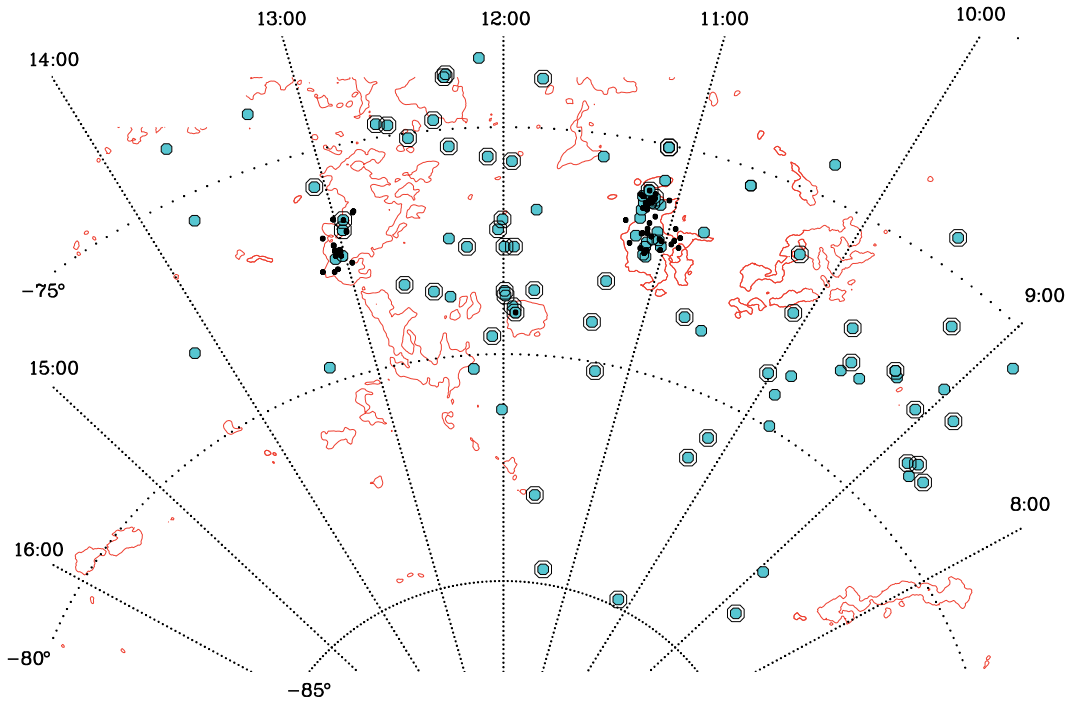

Figure 1.2: Spatial distribution of the CTTS (dots) and WTTS (shaded circles) in the Chamaeleon cloud complex. The IRAS 100 μm contour maps are overplotted (from Alcala et al. 1997).

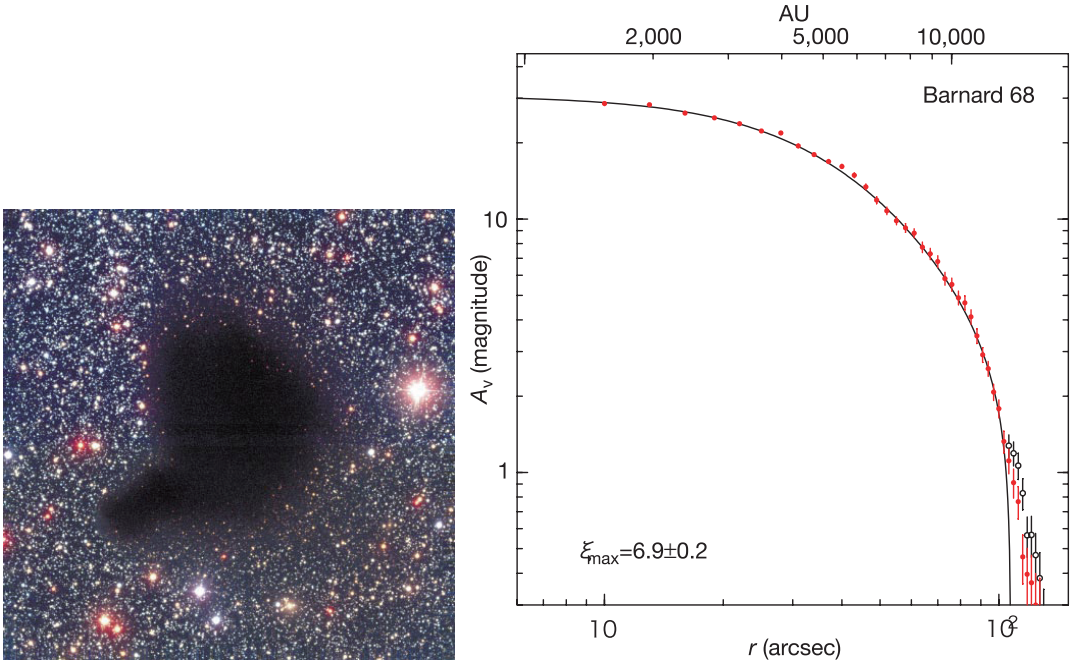

Figure 1.3: (*left*): Photograph of a Bok globule, Barnard 68. (*right*): Radial profile of visual extinction (A_V) of Barnard 68. The small circles are the data points for the averaged profile. The solid curve represents the best fit of a theoretical Bonner-Ebert sphere to the data (from Alves et al. 2001).

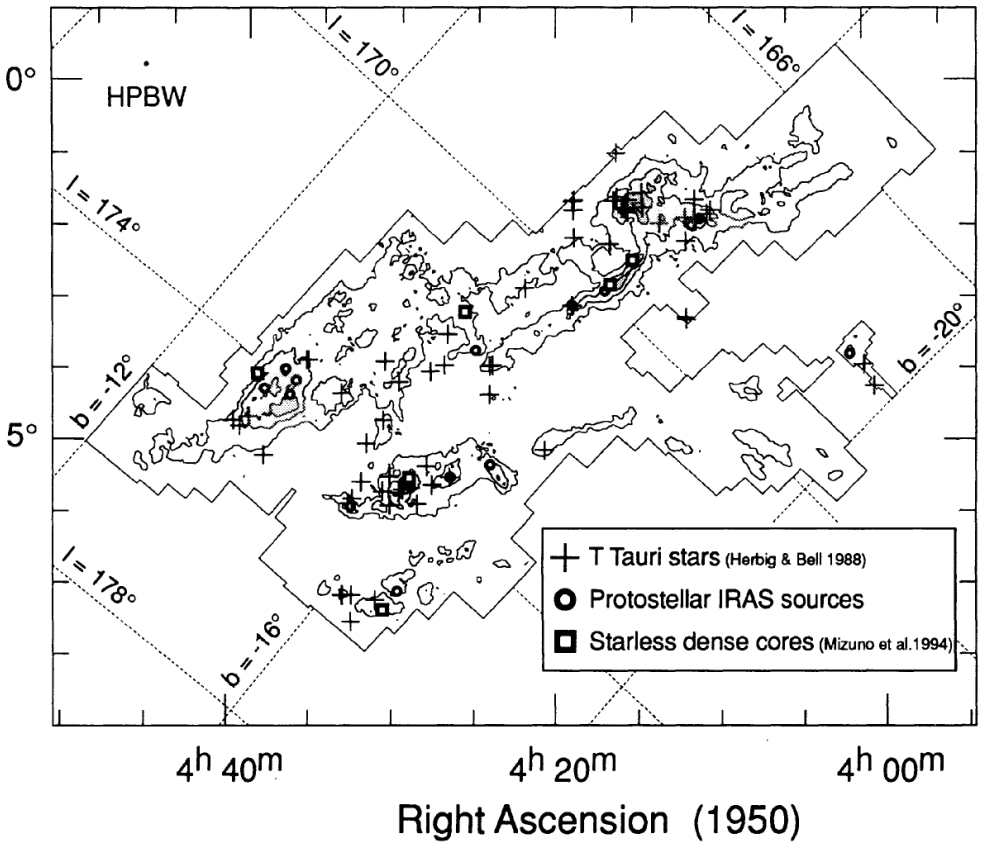

Figure 1.4: The ^{13}CO ($J = 1-0$) total intensity map of the Taurus molecular clouds. Contours are every 3.0 K km s^{-1} (from Mizuno et al. 1995).

Chapter 2

DATA SETS

2.1 AKARI

AKARI is the first Japanese infrared astronomical satellite dedicated to infrared astronomy (Murakami et al. 2007), which was launched on 2006 February 21st. After three weeks of performance verification (PV) phase (April 13th to May 7th), Phase 1 observations started on the May 8th and continued until November 9th, followed by Phase 2 observations until the exhaustion of liquid Helium on the August 26th, 2007. After the liquid Helium exhaustion, the telescope and focal plane of AKARI have still been kept less than 50K by the on-board cryocooler and Phase 3 (a.k.a. warm mission) observations started at near-infrared (NIR) wavelengths on 2008 June 1st, following second performance verification phase.

One of the major observation programs of AKARI is an all-sky survey at the mid- to far-infrared wavelengths with 6 photometric bands, and provide second-generation infrared catalogues to obtain a better spatial resolution and a wider spectral coverage than the first catalogues produced by the InfraRed Astronomcal Satellite (IRAS) mission (Neugebauer et al. 1984). AKARI has a 68.5 cm diameter cooled telescope with the following two scientific instruments of the Infrared Camera (IRC; Onaka et al. 2007, Figure 2.2) and the Far-Infrared Surveyor (FIS; Kawada et al. 2007, Figure 2.3). Its orbit is a Sun-synchronous polar orbit along the twilight zone at altitude of about 700 km. The wide fields of view (FoV; $\sim 10'$) covered by the large format arrays in these instruments makes them highly suitable for efficient surveys (see Figure 2.1). Furthermore, AKARI has the capability for imaging and spectroscopy in the wavelengths rage 2–180 μm in the pointed observation mode.

The All-Sky Survey had the highest priority in Phase 1 operations. In Phase 2 the observation plan was highly optimized for the FIS survey (not for the IRC survey) to fill the scan gaps caused in Phase 1 under constraints of carrying out the maximum number of pointed observations. No survey observations were performed in Phase 3.

2.1.1 The IRC All-Sky Survey

The IRC consists of three channels: the NIR (1.8–5.3 μm), MIR-S (5.4–13.1 μm), and MIR-L (12.4–26.5 μm). The NIR and MIR-S channels share the same FoV, while the MIR-L channel is separated about 20′ from them (see Figure 2.1). Each channel has three broad-band filters and additional dispersion elements. The photograph of the IRC is shown in Figure 2.2. Although the IRC was originally designed for imaging and spectroscopic observations in the pointed observation mode, the additional survey-type observation mode was confirmed (Ishihara et al. 2006).

The IRC All-Sky Survey was carried out with the *S9W* (9 μm) and *L18W* (18 μm) bands, and the point source catalogue (PSC) was released to the public in 2010 March. The IRC scanned 96 and 97 percent of the entire sky in *S9W* and *L18W* bands more than once during the 16 months, respectively. The IRC PSC Version-1 contains 870 973 sources (844 649 for *S9W* and 194 551 for *L18W*). The 5 σ detection limit for a point source is estimated to be 50 and 120 mJy in the *S9W* and *L18W* bands, respectively. The uncertainties in the absolute flux calibration are estimated to be 3% for the *S9W* band and 4% for the *L18W* band. The spatial resolutions are about 5″, and the position accuracies are estimated to be better than 2″. Table 2.1 gives the properties of the AKARI IRC PSC. The relative spectral response curves of the *S9W* and *L18W* bands are shown in Figure 2.4. The analysis of this paper is based on the 1st version of the IRC PSC. The details of the AKARI IRC All-Sky Survey and its data reduction processes are described in Ishihara et al. (2010), Kataza et al. (2010).

2.1.2 The FIS All-Sky Survey

The FIS has the two sets of detector arrays: the Short Wavelength array (SW) covering 50–110 μm and the Long Wavelength arrays (LW) covering 110–180 μm. Each detector has two arrays, narrow and wide bands. They share almost the same FoV. The picture of the FIS is shown in Figure 2.3.

The FIS All-Sky Survey was performed with these four bands (*N60*: 65 μm, *Wide-S*: 90 μm, *Wide-L*: 140 μm, and *N160*: 160 μm). The FIS Bright Source Catalogue (BSC) was also released to the public in 2010 March. The sky coverage of the FIS survey is 98 percent. The BSC Version-1 contains in total 427 071 sources (29 336 for *N60*, 373 819 for *Wide-S*, 117 994 for *Wide-L*, and 36 646 *N160*). The detection limit is estimated to be 3.2, 0.55, 3.8, and 7.5 Jy at *N60*, *Wide-S*, *Wide-L*, and *N160* bands, respectively. We note that in the bright sky regions such as the inner Galactic Plane, a different data sampling mode, CDS mode, was applied to the detector for the purpose to avoid saturation, and cost of higher noise level, i.e., worse detection limits. The flux uncertainties are 20%. The spatial resolution and position accuracy are determined by the data processing and are 48″ and 6″, respectively. Table 2.1 gives the properties of the

AKARI FIS BSC. The relative spectral response curves of the four FIS bands are shown in Figure 2.4. The analysis of this paper is based on the 1st version of the FIS BSC. See Yamamura et al. (2010) for more details.

Table 2.1: Properties of the AKARI Point Source Catalogue

	IRC PSC ver.1		FIS BSC ver.1			
Instrument	IRC		FIS			
Band	*S9W*	*L18W*	*N60*	*Wide-S*	*Wide-L*	*N160*
Wavelength [μm]	6–12	12–26	50–80	60–110	110–180	140–180
Band Centre [μm]	9	18	65	90	140	160
Number of sources	844 649	194 551	28 779	373 553	119 259	36 857
	870 973		427 071			
Detection limit [Jy]	0.05	0.12	3.2	0.55	3.8	7.5
Sky coverage[a] [%]	96	97	98			

[a] Sky coverage is defined as the area which was observed more than once.

2.2 Input TTSs Toward the Taurus-Auriga Region

For this study, we selected a 1800-square-degree ($2^{h}40^{m}$ < R.A. < $5^{h}40^{m}$ and 0° < Dec < 40°) part of the Taurus-Auriga region, which were used for the WTTS survey by the Roentgen satellite (ROSAT) (Wichmann et al. 1996, Magazzù et al. 1997, Li & Hu 1998). We first gathered known Taurus Young Stellar Objects (YSOs), mostly associated with the Taurus molecular cloud, from Strom et al. (1989), Beckwith et al. (1990), Güdel et al. (2007), Kenyon et al. (2008), and Rebull et al. (2010). Secondly, we selected the following TTSs from the YSOs:

- objects labelled as CTTSs or WTTSs in Güdel et al. (2007)
- objects listed in Kenyon et al. (2008) that were confirmed as Class II/III objects on the basis of the SIMBAD database and their references
- Class II/III objects including the 'new', 'probable', and 'possible' members in Rebull et al. (2010)

We note that Beckwith et al. (1990) and Strom et al. (1989) listed only TTSs. Furthermore, we added TTSs discovered by the ROSAT and distributed from the

cloud (Wichmann et al. 1996, Magazzù et al. 1997, Li & Hu 1998) [1]. In our TTS list, we considered close ($< 5''$; the spatial resolution of the AKARI IRC All-Sky Survey) binaries as a single source. We finally obtained a catalogue of 516 TTSs in the selected region. The distribution of our input TTSs is shown in Fig. 2.5.

We divide the known TTSs into two groups, TTSs which are associated to clouds, and TTSs which are isolated from clouds. We define the "cloud regions" as those where $A_V > 2$ (from Dobashi et al. 2005). Then we got 345 sources associated (within 1° from the cloud region) and 171 isolated TTSs.

We also classified them to CTTS and WTTS, for 399 sources whose equivalent width of Hα emission ($W(\mathrm{H}\alpha)$[2]) has been measured. We got 130 CTTSs ($W(\mathrm{H}\alpha) \leq -10$Å) and 269 WTTSs ($W(\mathrm{H}\alpha) > -10$Å). Table 2.2 summarizes the number of sources in our input TTSs.

Table 2.2: Numbers of Input TTSs

	associated	isolated	total
CTTS	122	8	130
WTTS	112	157	269
other	111	6	117
total	345	171	516

2.3 Catalogued Sources Toward the Taurus-Auriga Region

Since the AKARI's visibility for the Taurus region is relatively low due to the Sun-synchronous orbit of AKARI and the location of that region (near Ecliptic plane), we show the *completeness* of the sky coverage of the AKARI All-Sky Survey. For the 1800-square-degree region we selected, about 92 and 96 percent of the sky were surveyed with the *S9W* and *L18W* bands, respectively. The sky coverages with the four FIS bands are ∼99%. The difference of the coverage owe to the different field-of-view of these instruments (see Figure 2.1), and the survey operation was optimized for the FIS.

In the selected regions, there are 14 725 AKARI IRC sources (14 546 *S9W* and 2720 *L18W*), and 12 027 FIS sources (444 *N60*, 10 051 *Wide-S*, 3063 *Wide-L*, and 608 *N160*). The detection limit of the *S9W* band (50 mJy), which is the

[1]We removed one source, 1RXS J032409.7+123745, from Li & Hu (1998) list, because it seems to be a Li rich giant from its too bright luminosity (3–4 magnitudes in NIR wavelengths) as a K2 dwarf star at distance of 140 pc.

[2]Equivalent width is negative for emission line, and positive for absorption line.

most sensitive one, corresponds to 8 magnitude. Assuming the distance of 140 pc, this detection limit is consistent with a 1 Myr M0 star, a 10 Myr K5 star, or a Zero-Age-Main-Sequence F0 star (see Figure 2.6). This sensitivity is sufficient for survey of the Sun-like sources at a distance of ∼100 pc.

2.4 Archival Data

In order to verify the positional accuracy of AKARI (IRC) point sources and to construct more complete data sets of our T Tauri stars, we have used the Near-Infrared survey of the Two Micron All Sky Survey (2MASS; Skrutskie et al. 2006) and the optical survey of the USNO CCD Astrograph Catalogue (UCAC; Zacharias et al. 2010).

2.4.1 Near-Infrared data

Ita et al. (2010) [3] compared the IRC PSC with the 2MASS PSC to assess the positional accuracy of the IRC PSC, although most the AKARI's attitude in the survey mode referred the 2MASS PSC. Since the 2MASS point source catalogue is complete down to $K_S < 14.3$ mag in the absence of confusion and the detection limit of 50 mJy (or ∼8 mag) at the AKARI *S9W* band, all normal stars seen by AKARI should be prominent in the 2MASS PSC. The position quality of the 2MASS sources are estimated to be 70–80 mas over most of the magnitude range. Therefore, the 2MASS PSC is useful to assess the positional accuracy of the IRC PSC. There are 756 997 sources with S/N > 5 at the *S9W* band in the IRC PSC. They used these 756 997 'good' IRC sources, and compared to the 'good' 2MASS PSC with the K_S band magnitude of <14.3 and S/N > 5. Of the 756 997 sources, 505 290 (67%), 669 771 (88%), 708 969 (94%), 719 822 (95%), 723 215 (96%) sources have 2MASS counterparts at the radii of 1, 2, 3, 4, and 5 arcsec, respectively (Figure 2.7). They also mentioned based on sub-sample of 563 935 sources with S/N > 10 at the *S9W* band, that the positional accuracy of the IRC PSC does not have any dependency on the source brightness.

The dependency on the source density was also checked. There are 77 232 good IRC sources at high galactic latitude ($|b| > 30°$), and 71 526 (93%) sources have counterpart of 2MASS good sources within $5''$ radius. This result indicates that the positional accuracy of the IRC PSC may depend on the source density. They concluded that the positional accuracy of the IRC PSC sources is better than $3''$ for most of the sources.

We, then, compared the IRC PSC with the 2MASS PSC toward the 1800-square-degree of the Taurus region. In this regions, there are 14 725 IRC sources. We note that we did not choose the 'good' IRC sources. Of the 14 725 IRC

[3] They used the team internal released version of the IRC PSC, and the number of sources are slightly different from this study. The catalogue quality is almost the same.

sources, 14 593 (99.1%) and 14 671 (99.6%) sources have 2MASS counterparts within 3 and 5″ radius, respectively. If we limit the 'good' 2MASS sources, there are 13 675 (92.9%) and 13 746 (93.4%) sources within 3 and 5″ radius, respectively.

2.4.2 Optical data

We also compared the IRC PSC with the 3rd version of the UCAC (UCAC3). UCAC3 consists of mainly the 8–16 magnitude range in a 579–642 nm bandpass, between V and R, and contains over 100 million sources. The limiting magnitude and bright magnitude cut-off could vary about ±0.3 mag, depending on sky conditions at the observed time. The positional accuracy are estimated to be 15–20 mas for stars in the 10–14 mag range. Over 95 million stars in UCAC3 have a computed proper motion; for 45.4 million of them the proper motion is based on observations at only 2 epochs, while other 49.5 million stars have observations at least 3 epochs.

First, we compared the 'good' IRC PSC with 'good' UCAC3 sources which have magnitudes of 8–16 and S/N > 5. Of the 756 997 sources, 346 336 (46%), 419 136 (55%), 432 417 (57%), 437 013 (58%), and 439 827 (58%) sources have UCAC3 counterpart within the radii of 1, 2, 3, 4, and 5 arcsec, respectively (Figure 2.8). This relatively low cross-identification rate is caused by the limited magnitude range of the UCAC3 survey in which the most nearby (< 100 pc) stars are saturated, and distant (> 1 kpc) or heavily reddened stars have no UCAC3 entry because of the catalogue's limited sensitivity.

Of the 14 725 IRC sources toward the Taurus region, 13 667 (92.8%) and 13 723 (93.2%) sources have counterpart in the UCAC3 within 3 and 5″ radius, respectively. If we limit the 'good' UCAC3 sources by their magnitudes and S/N, there are 11 254 (76.4%) and 11 278 (76.6%) sources within 3 and 5″ radii, respectively.

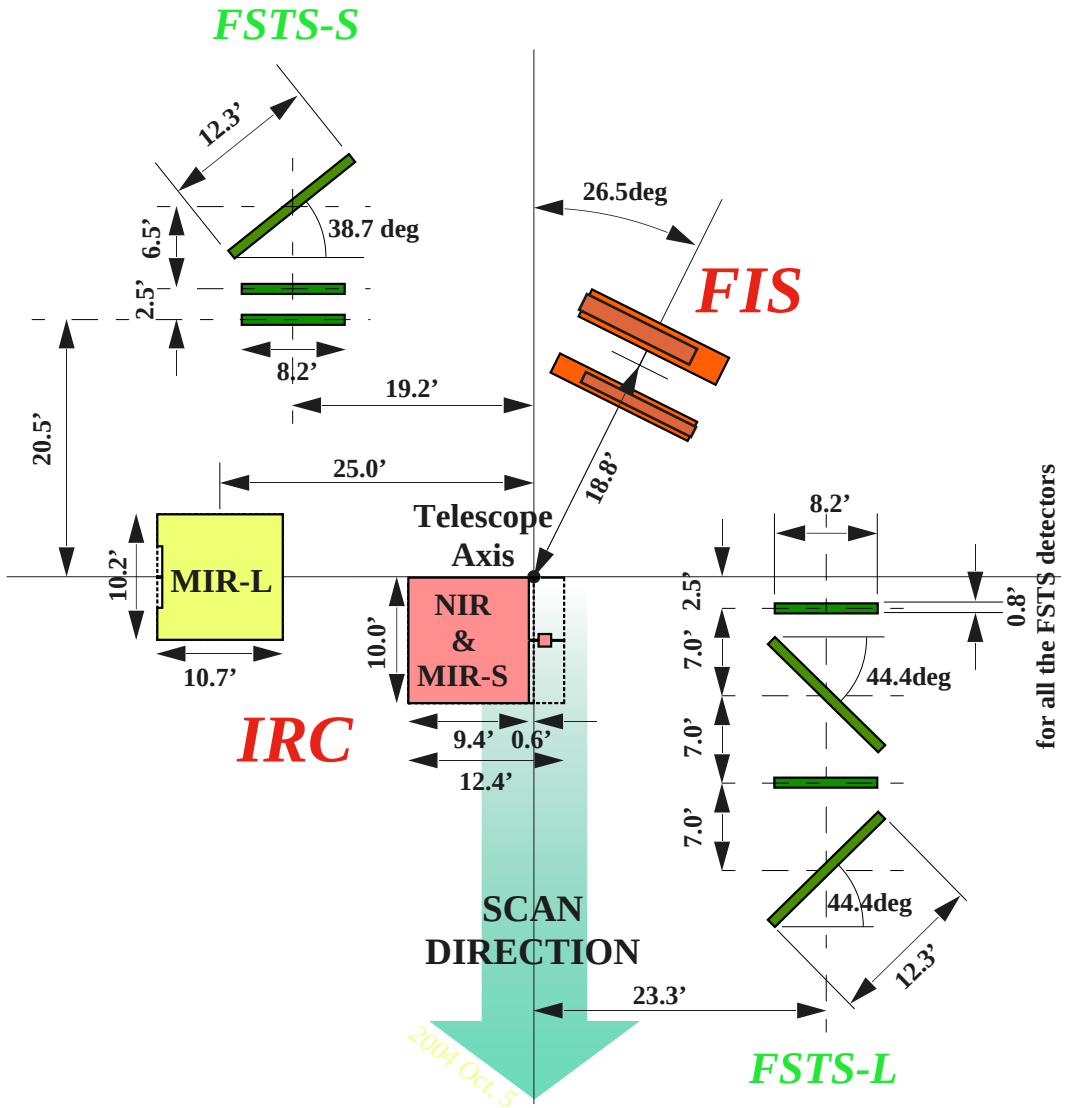

Figure 2.1: Layout of the focal-plane projected onto the sky (from Murakami et al. 2007). The FIS SW arrays are shown by the two small dark orange rectangles, and the FIS LW are the large light orange ones. The FSTS-S & -L arrays are focal-plane star trackers.

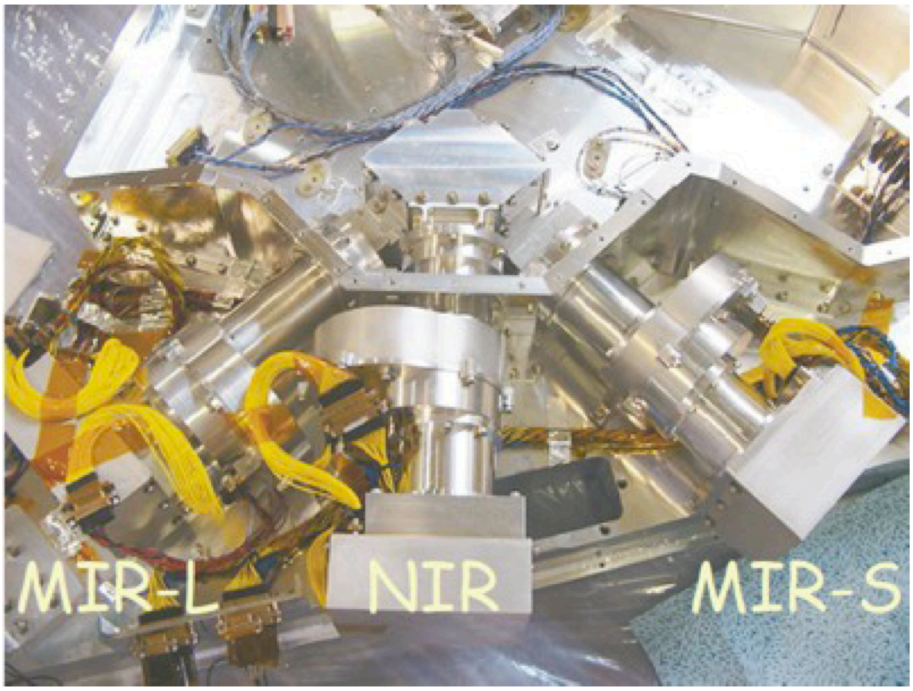

Figure 2.2: Photograph of the IRC (from Onaka et al. 2007).

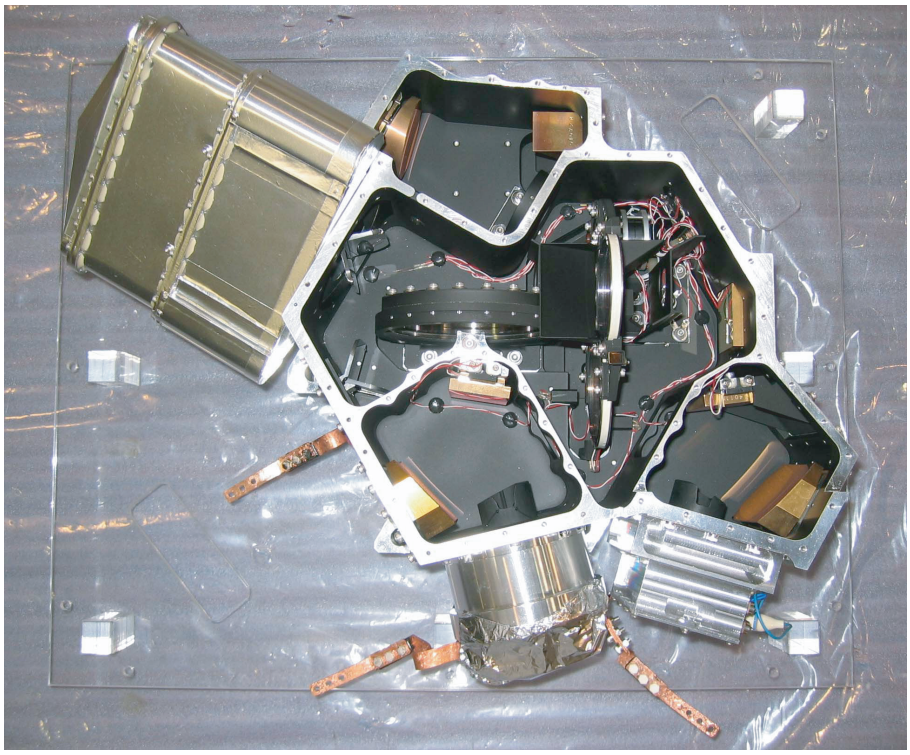

Figure 2.3: Picture of FIS at final integration (from Kawada et al. 2007). The top cover is removed to show the FIS optics.

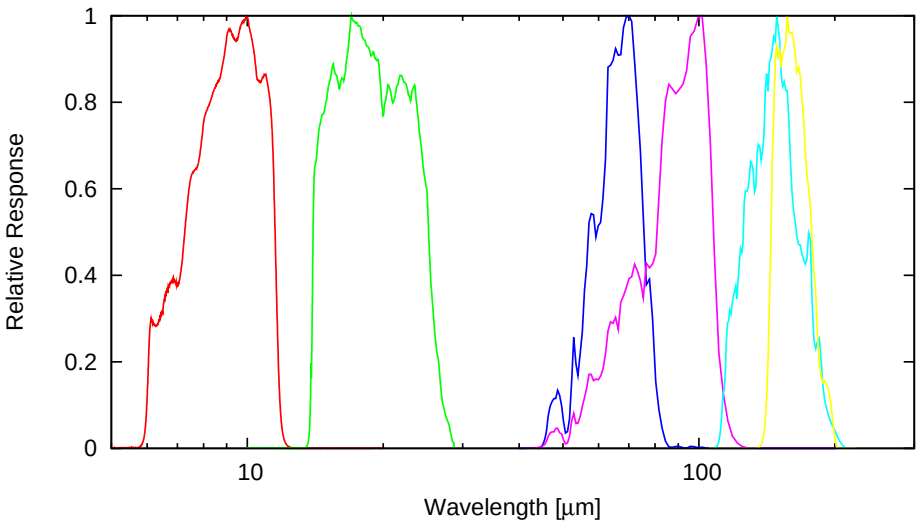

Figure 2.4: Spectral response curves of the *S9W*, *L18W*, *N60*, *Wide-S*, *Wide-L*, and *N160* bands normalized to the peak (left to right) (from Onaka et al. 2007, Kawada et al. 2007).

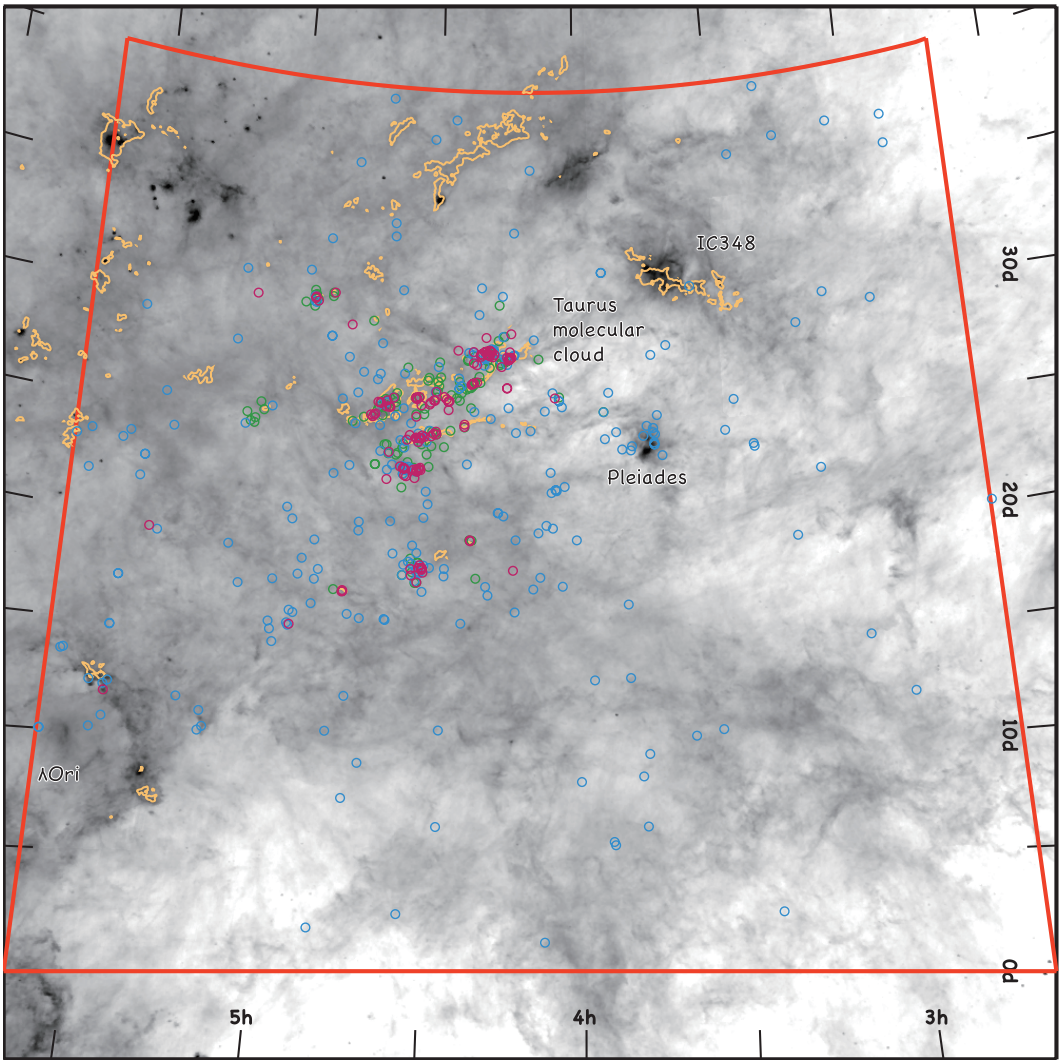

Figure 2.5: Distribution of the target TTSs. The magenta circles are CTTSs, cyan ones are WTTSs, and the green ones are TTSs whose equivalent width of Hα were not provided. The grey scale is IRAS 100 μm image, and the yellow contour indicates the extinction of $A_V = 2$ (from Dobashi et al. 2005). The red box indicates the region we searched for this study.

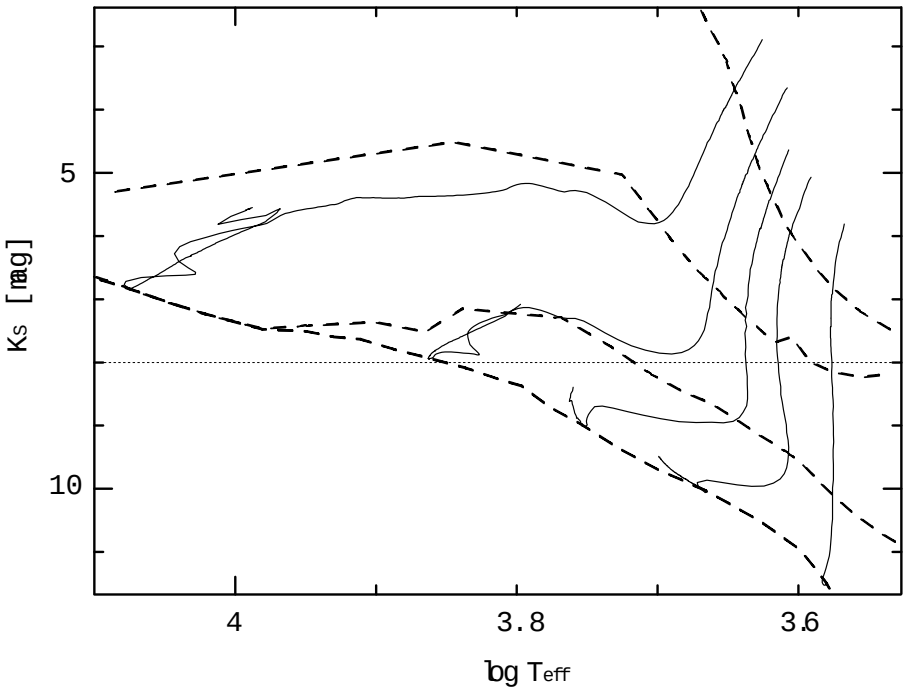

Figure 2.6: H-R diagram of the Siess et al. (2000) evolutionary tracks with distance of 140 pc. The horizontal broken curves are isochrones for 0.1, 1, 10 Myr and Zero-Age-Main-Sequence (from top to bottom). The vertical solid curves are represent mass tracks for 0.5, 0.8, 1.1, 1.6, and 3 $M_{\odot}$ (from right to left). The dotted line indicates the sensitivity of the AKARI All-Sky Survey at 9 μm band.

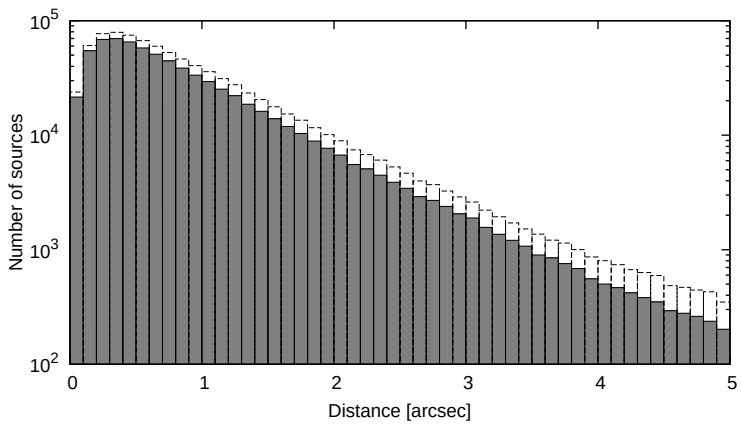

Figure 2.7: The histogram of positional differences between the AKARI IRC PSC and the 2MASS PSC for matched sources. The hatched areas represent matched sources with good IRC PSC and good 2MASS PSC. The size of the bin is 0.1 arcsec.

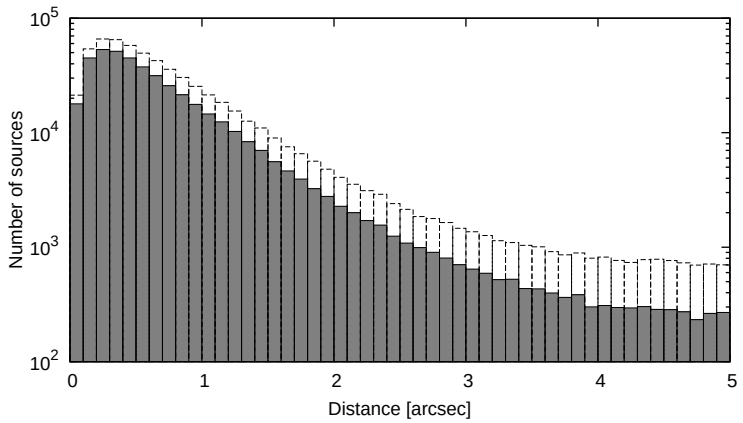

Figure 2.8: The histogram of positional differences between the AKARI IRC PSC and UCAC3 for matched sources. The hatched areas represent matched sources with good IRC PSC and good UCAC3. The size of the bin is 0.1 arcsec.

Chapter 3

RESULTS

Part of this chapter is published in the Astronomy & Astrophysics
as
"A survey of T Tauri stars with AKARI toward the Taurus-Auriga region"
by
Takita et al.

3.1 Detections of Previously Known T Tauri Stars with AKARI

Of the 516 previously known T Tauri stars (TTSs) we compiled, 503 and 508 TTSs were observed twice or more with the *S9W* and *L18W* bands, respectively. There are 10 and 8 sources, observed only once with the *S9W* and *L18W* bands, respectively, and then, 3 sources (SST Tau 042423.2+265008, CFHT-9, and IRAS 04216+2603) not observed at all in the *S9W* band. On the other hand, 511 TTSs were observed twice or more with the four FIS bands, and the remaining 5 sources were observed only once.

Table 3.1: Observed and detected numbers of the input T Tauri stars.

Band	Observed				Detected	
	0	1	>2	total		
S9W	3	10	506	516	126	132
L18W	0	8	508	516	94	
FIS	0	5	511	516	79	

We searched for 516 previously known TTSs in the AKARI IRC Point Source Catalogue, and detected 132 TTSs within 5″ searching radius, i.e., the resolution of the AKARI IRC All-Sky Survey: 126 and 94 sources were detected in the *S9W*

(9 μm) and *L18W* (18 μm) bands, respectively. Six sources were detected only in the *L18W* band: 3 sources (IRAS 04200+2759, IRAS 04295+2251, and UX Tau) were observed/detected only once in the *S9W* band, so the IRC PSC does not include these sources. The other 3 sources were not detected at all. The positions of almost all the AKARI detected sources agree well with those in the previous catalogues to within the uncertainty of 3″ (see Figure 3.1). Although the positions of GI Tau in the different catalogues have larger differences than 3″, all of them agree to within the positional accuracy of AKARI IRC PSC.

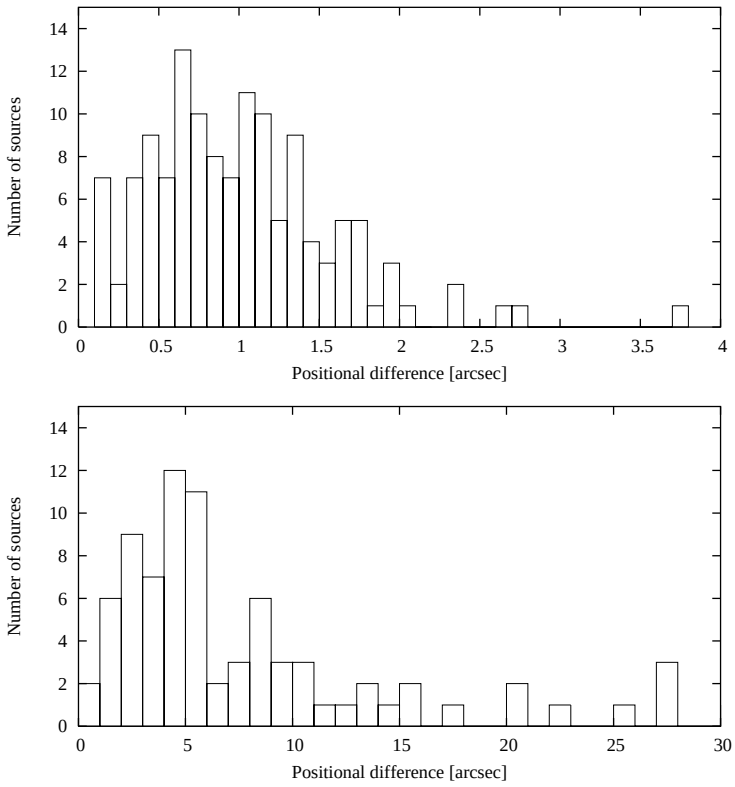

Figure 3.1: (*Top*) Histogram of the positional differences between the TTSs detected by AKARI (IRC PSC) and those in the previous catalogues. The bin size of the positional difference is 0.1 arcsec. (*Bottom*) Histogram of the positional differences between the TTSs detected by AKARI (FIS BSC) and those in the previous catalogues. The bin size of the positional difference is 1 arcsec.

We also searched for previously known TTSs in the AKARI FIS Bright Source Catalogue. In this survey, we used sources with $FQUAL$=3, which represents that the source is highly reliable. We then got 79 sources within the searching radius of 30″. For these 79 sources, 3 TTSs did not have reliable values for the flux density at the *Wide-S* (90 μm) band, which is the most sensitive band of the FIS. GV Tau and IRAS 04264+2433 were detected only once and CFHT-1 was not detected at that band, but they were detected at least twice at the *Wide-L*

(140 μm) band.

There are 15 sources which were detected by the FIS but not detected by the IRC. Six sources have angular separation of $> 5''$ (spacial resolution of the IRC) between the previous catalogue and the FIS BSC. DM Tau was detected twice in the *L18W* band, but the positions in the two independent images have a larger difference than $5''$ between each other for the current positional accuracy, and therefore, no entry in the IRC PSC. The other 5 sources (IRAS 04216+2603, IRAS 04260+2642, IRAS 04302+2247, LR1, and SST Tau J041542.7+290959) were detected only once or not detected at both the *S9W* and *L18W* bands, then these sources were not catalogued in the IRC PSC. Since these sources are bright at the 24 μm bandpass ($\sim$4 magnitude) but faint at the 8 μm bandpass ($\sim$8–9 magnitude) (Rebull et al. 2010, Luhman et al. 2010), they are thought to have inner gaps in their disks. We note that IRAS 04216+2603 was not observed in the *S9W* band at all.

For the 9 sources that have larger angular separation of $5''$ between the previous catalogue and the FIS BSC, only HD 30171 has IRC counterparts within the positional accuracy of $48''$.

The photometric data of the AKARI detected TTSs are listed in Table 3.2 and Table 3.3.

Table 3.2: AKARI (IRC), UCAC, and 2MASS photometric data for the previously known Taurus members.

IRC name[a]	Identifier	*S9W*[b] [mag]	*L18W*[c] [mag]	UCAC[d] [mag]	2MASS J [mag]	2MASS H [mag]	2MASS K_S [mag]
0311138+222457	1RXS J031113.0+222518	6.847 ± 0.154		8.359 ± 0.093	7.273 ± 0.020	7.069 ± 0.053	6.968 ± 0.027
0324065+234706	1RXS J032406.6+234714	6.008 ± 0.048		10.018 ± 1.000	7.128 ± 0.020	6.492 ± 0.020	6.267 ± 0.018
0327325+255400	1RXS J032733.2+255405	6.947 ± 0.508		9.090 ± 1.000	7.927 ± 0.032	7.550 ± 0.051	7.488 ± 0.023
0400095+081818	RXJ0400.1+0818N	7.041 ± 0.183		9.775 ± 0.048	8.281 ± 0.024	8.028 ± 0.000	7.843 ± 0.000
0404430+261856	L1489 IRS	3.745 ± 0.020	0.694 ± 0.022		14.129 ± 0.000	11.908 ± 0.000	9.859 ± 0.043
0406513+254127	RXJ0406.8+2541	6.207 ± 0.126		11.452 ± 0.058	8.767 ± 0.021	8.026 ± 0.034	7.750 ± 0.018
0413271+281624	Anon 1	6.785 ± 0.221		13.261 ± 0.171	8.826 ± 0.030	7.794 ± 0.027	7.460 ± 0.029
0413532+281124	IRAS 04108+2803 A	6.022 ± 0.116			13.639 ± 0.024	11.521 ± 0.024	10.370 ± 0.019
0413573+291820	IRAS 04108+2910	5.648 ± 0.044	3.559 ± 0.152	16.015 ± 0.316	11.310 ± 0.023	10.157 ± 0.024	9.356 ± 0.024
0414129+281212	V773 Tau	4.213 ± 0.028	2.247 ± 0.039	10.434 ± 0.033	7.494 ± 0.024	6.644 ± 0.020	6.210 ± 0.047
0414135+281249	FM Tau	5.729 ± 0.057	3.554 ± 0.036		10.329 ± 0.021	9.391 ± 0.022	8.763 ± 0.022
0414146+282758	FN Tau	5.383 ± 0.096	2.780 ± 0.039	14.151 ± 0.267	9.469 ± 0.022	8.669 ± 0.036	8.189 ± 0.018
0414170+281058	CW Tau	4.144 ± 0.043	2.324 ± 0.049	13.390 ± 0.169	9.557 ± 0.022	8.243 ± 0.027	7.127 ± 0.023
0414176+280609	CIDA-1	6.126 ± 0.126	4.187 ± 0.156		11.726 ± 0.021	10.584 ± 0.022	9.877 ± 0.021
0414263+280602	IRAS 04113+2758 A	3.525 ± 0.017	1.031 ± 0.067		12.475 ± 0.029	9.878 ± 0.033	7.777 ± 0.031
0414305+280514	MHO 3	4.049 ± 0.028	1.185 ± 0.022		11.178 ± 0.021	9.249 ± 0.022	8.243 ± 0.023
0414478+264810	CX Tau	6.227 ± 0.093	3.725 ± 0.100	13.589 ± 0.073	9.867 ± 0.022	9.054 ± 0.024	8.807 ± 0.019
0414479+275234	LkCa 3	6.860 ± 0.189		11.865 ± 0.063	8.363 ± 0.032	7.625 ± 0.023	7.423 ± 0.021
0414492+281230	FO Tau	5.719 ± 0.105	3.511 ± 0.052	15.099 ± 0.192	9.650 ± 0.021	8.568 ± 0.021	8.121 ± 0.031
0417337+282047	CY Tau	6.270 ± 0.081		13.022 ± 0.069	9.828 ± 0.020	8.970 ± 0.024	8.597 ± 0.021
0417496+282936	V410 X-ray 1	5.997 ± 0.086	4.415 ± 0.049	16.680 ± 0.515	11.020 ± 0.021	9.733 ± 0.027	9.081 ± 0.019
0418107+251957	[GBM90] L1506 1	6.537 ± 0.096		13.039 ± 0.223	10.744 ± 0.024	9.589 ± 0.022	9.032 ± 0.019
0418310+282716	V410 Tau	7.184 ± 0.111		10.366 ± 0.003	8.449 ± 0.018	7.789 ± 0.021	7.629 ± 0.026
0418311+281629	DD Tau	4.271 ± 0.027	2.366 ± 0.043	14.748 ± 0.232	9.830 ± 0.021	8.682 ± 0.020	7.878 ± 0.020
0418316+281658	CZ Tau	4.471 ± 0.033	2.461 ± 0.046	15.239 ± 0.023	10.517 ± 0.021	9.774 ± 0.022	9.362 ± 0.017

Table 3.2: continued.

IRC name[a]	Identifier	*S9W*[b] [mag]	*L18W*[c] [mag]	UCAC[d] [mag]	2MASS *J* [mag]	2MASS *H* [mag]	2MASS K_S [mag]
0418320+283115	IRAS 04154+2823	4.882 ± 0.102	2.420 ± 0.048		15.187 ± 0.048	12.369 ± 0.022	10.274 ± 0.017
0418344+283029	V410 X-ray 2		4.559 ± 0.071		13.773 ± 0.026	10.708 ± 0.022	9.215 ± 0.017
0418406+281914	V892 Tau	1.278 ± 0.016	-1.777 ± 0.016	14.846 ± 0.111	8.742 ± 0.027	7.016 ± 0.029	5.787 ± 0.016
0418470+282008	Hubble 4	6.931 ± 0.275		12.181 ± 0.093	8.560 ± 0.020	7.636 ± 0.026	7.293 ± 0.024
0418514+282026	CoKu Tau/1	5.239 ± 0.089	1.884 ± 0.022		12.866 ± 0.030	11.489 ± 0.031	10.974 ± 0.024
0419010+281942	V410 X-ray 6		4.747 ± 0.066		10.527 ± 0.022	9.597 ± 0.024	9.129 ± 0.021
0419128+282933	FQ Tau	7.175 ± 0.294		15.097 ± 0.195	10.491 ± 0.026	9.702 ± 0.024	9.313 ± 0.022
0419158+290626	BP Tau	5.335 ± 0.123	3.303 ± 0.049	11.927 ± 0.081	9.098 ± 0.037	8.220 ± 0.024	7.736 ± 0.023
0419354+282721	FR Tau	6.853 ± 0.357		16.321 ± 0.900	10.954 ± 0.021	10.374 ± 0.022	9.971 ± 0.018
0420258+281922	SST Tau 042025.8+281923	6.564 ± 0.132	4.612 ± 0.054		15.327 ± 0.039	13.422 ± 0.026	11.718 ± 0.021
0420260+280409	SST Tau 042026.0+280408	6.643 ± 0.242	3.740 ± 0.071	14.696 ± 0.190	10.612 ± 0.021	9.949 ± 0.022	9.697 ± 0.018
0421079+270220	CFHT-19	5.309 ± 0.030	2.735 ± 0.054		13.855 ± 0.024	12.062 ± 0.026	10.543 ± 0.021
0421432+193413	IRAS 04187+1927	4.274 ± 0.041	2.494 ± 0.027		10.185 ± 0.022	8.725 ± 0.024	8.021 ± 0.018
0421556+275506	DE Tau	5.382 ± 0.052	3.455 ± 0.017	12.773 ± 0.165	9.180 ± 0.022	8.273 ± 0.018	7.799 ± 0.018
0421574+282635	RY Tau	1.652 ± 0.017	-0.273 ± 0.019	10.064 ± 0.037	7.155 ± 0.019	6.128 ± 0.061	5.395 ± 0.023
0421588+281806	HD 283572	6.805 ± 0.274		8.847 ± 0.044	7.414 ± 0.029	7.008 ± 0.026	6.869 ± 0.023
0421594+193205	T Tau	1.539 ± 0.019	-1.127 ± 0.029	9.747 ± 0.071	7.240 ± 0.023	6.237 ± 0.017	5.325 ± 0.017
0422007+265733	FS Tau B	5.327 ± 0.057	2.181 ± 0.316		15.082 ± 0.082	13.351 ± 0.053	11.753 ± 0.029
0422022+265729	FS Tau A	4.453 ± 0.044	1.877 ± 0.149	13.796 ± 0.900	10.705 ± 0.027	9.244 ± 0.026	8.178 ± 0.017
0422167+265456	CFHT-21	5.699 ± 0.065	3.793 ± 0.076	13.575 ± 1.000	11.577 ± 0.019	10.037 ± 0.022	9.011 ± 0.021
0422478+264552	IRAS 04196+2638	5.759 ± 0.099	4.330 ± 0.053		11.589 ± 0.022	10.147 ± 0.025	9.287 ± 0.019
0423077+280557	IRAS 04200+2759		3.998 ± 0.140		13.179 ± 0.021	11.600 ± 0.024	10.413 ± 0.018
0423354+250300	FU Tau	6.199 ± 0.024			10.781 ± 0.026	9.945 ± 0.027	9.324 ± 0.024
0423391+245613	FT Tau	6.030 ± 0.071	3.809 ± 0.128	14.791 ± 0.174	10.192 ± 0.026	9.123 ± 0.027	8.596 ± 0.021
0424570+271156	IP Tau	6.019 ± 0.039		12.046 ± 0.900	9.781 ± 0.021	8.893 ± 0.017	8.349 ± 0.018
0426535+260654	FV Tau	4.086 ± 0.027	2.116 ± 0.066	14.135 ± 0.900	9.917 ± 0.022	8.325 ± 0.024	7.442 ± 0.020

Table 3.2: continued.

IRC name[a]	Identifier	*S9W*[b] [mag]	*L18W*[c] [mag]	UCAC[d] [mag]	2MASS *J* [mag]	2MASS *H* [mag]	2MASS K_S [mag]
0426573+260629	KPNO-13	7.081 ± 0.157			11.281 ± 0.022	10.172 ± 0.022	9.580 ± 0.021
0427025+260531	DG Tau B	5.336 ± 0.027	1.838 ± 0.051		16.516 ± 0.141	13.525 ± 0.000	12.038 ± 0.000
0427028+254222	DF Tau	4.272 ± 0.054	2.644 ± 0.074	11.703 ± 0.075	8.171 ± 0.026	7.256 ± 0.023	6.734 ± 0.024
0427046+260616	DG Tau A	2.995 ± 0.017	0.369 ± 0.026		8.691 ± 0.018	7.722 ± 0.031	6.992 ± 0.020
0427572+261918	IRAS 04248+2612	6.750 ± 0.105	3.307 ± 0.045		13.235 ± 0.053	11.795 ± 0.047	11.026 ± 0.040
0429208+274207	IRAS 04262+2735	4.379 ± 0.036	3.326 ± 0.065	15.095 ± 1.000	8.550 ± 0.026	7.461 ± 0.016	7.015 ± 0.017
0429217+270126	IRAS 04263+2654	6.545 ± 0.149	4.190 ± 0.107		10.801 ± 0.022	9.496 ± 0.022	8.725 ± 0.017
0429237+243301	GV Tau	1.579 ± 0.023	-1.163 ± 0.016		11.544 ± 0.025	9.587 ± 0.023	8.054 ± 0.024
0429300+243955	IRAS 04264+2433	5.838 ± 0.065	2.047 ± 0.056		13.728 ± 0.036	11.982 ± 0.031	11.135 ± 0.027
0429360+243554	J04293606+2435556	6.573 ± 0.041			10.780 ± 0.019	9.392 ± 0.020	8.659 ± 0.020
0429415+263258	DH Tau	6.332 ± 0.201	4.073 ± 0.070	13.462 ± 1.000	9.767 ± 0.021	8.824 ± 0.026	8.178 ± 0.026
0429515+260644	IQ Tau	5.274 ± 0.068	3.574 ± 0.070	13.890 ± 0.226	9.415 ± 0.020	8.417 ± 0.023	7.779 ± 0.023
0430039+181348	UX Tau C		3.478 ± 0.038		8.623 ± 0.023	7.960 ± 0.018	7.551 ± 0.021
0430296+242644	FX Tau	5.505 ± 0.079	3.556 ± 0.125	12.230 ± 0.900	9.388 ± 0.024	8.398 ± 0.018	7.924 ± 0.016
0430442+260124	DK Tau	4.191 ± 0.030	2.399 ± 0.033	11.986 ± 0.071	8.719 ± 0.030	7.758 ± 0.024	7.096 ± 0.016
0430502+230008	IRAS 04278+2253	2.103 ± 0.019	0.198 ± 0.020	15.580 ± 0.364	8.778 ± 0.024	7.040 ± 0.015	5.855 ± 0.023
0430513+244221	ZZ Tau	6.831 ± 0.153		14.544 ± 1.000	9.495 ± 0.021	8.695 ± 0.029	8.441 ± 0.021
0430517+244147	ZZ Tau IRS	5.883 ± 0.069	2.903 ± 0.103		12.842 ± 0.023	11.435 ± 0.026	10.314 ± 0.023
0431341+180804	L1551 IRS5	2.794 ± 0.026			13.708 ± 0.060	11.505 ± 0.052	9.822 ± 0.035
0431361+181344	LkHa 358	5.437 ± 0.170			12.792 ± 0.032	10.922 ± 0.029	9.687 ± 0.021
0431384+181357	HL Tau	2.697 ± 0.030	-0.231 ± 0.058		10.624 ± 0.042	9.171 ± 0.046	7.410 ± 0.017
0431400+181357	XZ Tau	3.421 ± 0.079		13.678 ± 0.124	9.385 ± 0.027	8.148 ± 0.040	7.291 ± 0.024
0431505+242418	HK Tau	6.255 ± 0.019	3.428 ± 0.060	13.588 ± 0.900	10.451 ± 0.022	9.253 ± 0.022	8.593 ± 0.018
0431578+182137	V710 Tau	5.999 ± 0.282	4.013 ± 0.194	13.560 ± 1.000	9.279 ± 0.032	9.107 ± 0.030	8.654 ± 0.025
0432154+242859	Haro 6-13	4.501 ± 0.093	1.604 ± 0.061		11.237 ± 0.024	9.319 ± 0.020	8.101 ± 0.029
0432303+173139	GG Tau A	4.540 ± 0.111	2.599 ± 0.051	11.785 ± 0.019	8.674 ± 0.035	7.815 ± 0.026	7.364 ± 0.018

Table 3.2: continued.

IRC name[a]	Identifier	*S9W*[b] [mag]	*L18W*[c] [mag]	UCAC[d] [mag]	2MASS J [mag]	2MASS H [mag]	2MASS K_S [mag]
0432317+242002	FZ Tau	4.138 ± 0.119	2.417 ± 0.030	13.352 ± 0.900	9.895 ± 0.022	8.400 ± 0.029	7.347 ± 0.017
0432320+225726	IRAS 04295+2251		1.947 ± 0.068		14.889 ± 0.044	11.982 ± 0.036	10.141 ± 0.024
0432429+255231	UZ Tau A	4.085 ± 0.022	2.247 ± 0.022	10.985 ± 1.000	9.136 ± 0.000	8.117 ± 0.000	7.354 ± 0.033
0432491+225303	JH112	5.189 ± 0.019	3.086 ± 0.047	15.093 ± 0.172	10.238 ± 0.027	8.995 ± 0.032	8.169 ± 0.023
0433062+240933	GH Tau	5.483 ± 0.137	3.804 ± 0.159	12.584 ± 1.000	9.109 ± 0.021	8.234 ± 0.027	7.794 ± 0.021
0433066+240955	V807 Tau	5.198 ± 0.089	3.638 ± 0.073	11.197 ± 1.000	8.146 ± 0.023	7.357 ± 0.026	6.960 ± 0.016
0433190+224633	IRAS 04303+2240	3.695 ± 0.060	2.000 ± 0.035	17.446 ± 1.000	11.103 ± 0.020	9.209 ± 0.023	7.673 ± 0.027
0433329+180059	HD 28867	5.092 ± 0.096	3.885 ± 0.256	6.466 ± 0.093	5.915 ± 0.035	5.813 ± 0.029	5.786 ± 0.023
0433341+242114	GI Tau	3.998 ± 0.127	1.848 ± 0.043	13.488 ± 1.000	9.341 ± 0.020	8.418 ± 0.021	7.888 ± 0.023
0433346+242106	GK Tau	4.478 ± 0.089		12.044 ± 1.000	9.053 ± 0.027	8.108 ± 0.026	7.468 ± 0.021
0433367+260949	IS Tau	5.662 ± 0.056	3.970 ± 0.047		10.323 ± 0.021	9.293 ± 0.023	8.642 ± 0.018
0433390+252038	DL Tau	4.749 ± 0.091	2.673 ± 0.041	12.894 ± 0.112	9.630 ± 0.021	8.679 ± 0.027	7.960 ± 0.021
0433394+175152	HN Tau	4.538 ± 0.061	2.574 ± 0.046	13.290 ± 0.124	10.699 ± 0.026	9.471 ± 0.027	8.384 ± 0.021
0433446+261500	SST Tau 043344.6+261500	6.791 ± 0.116			11.639 ± 0.021	10.385 ± 0.022	9.744 ± 0.018
0433519+225030	CI Tau	5.034 ± 0.093	2.926 ± 0.024	13.157 ± 0.142	9.480 ± 0.020	8.431 ± 0.040	7.793 ± 0.020
0433546+261326	IT Tau	5.661 ± 0.091	3.911 ± 0.169	13.073 ± 0.900	9.866 ± 0.025	8.591 ± 0.036	7.860 ± 0.026
0434554+242852	AA Tau	5.439 ± 0.017	3.556 ± 0.025	12.373 ± 1.000	9.433 ± 0.024	8.546 ± 0.023	8.047 ± 0.024
0435273+241458	DN Tau	5.816 ± 0.063	3.647 ± 0.120	12.171 ± 0.087	9.139 ± 0.021	8.342 ± 0.027	8.015 ± 0.021
0435410+241108	CoKu Tau/3	5.129 ± 0.072	3.664 ± 0.043		10.731 ± 0.026	9.197 ± 0.026	8.411 ± 0.024
0435473+225021	HQ Tau	4.208 ± 0.064		11.788 ± 0.144	8.655 ± 0.024	7.731 ± 0.016	7.135 ± 0.021
0435528+225422	HP Tau	4.383 ± 0.090	2.049 ± 0.031	14.090 ± 0.201	9.549 ± 0.022	8.469 ± 0.065	7.625 ± 0.024
0435568+225436	Haro 6-28	6.885 ± 0.072		15.986 ± 1.000	11.142 ± 0.022	10.055 ± 0.022	9.531 ± 0.020
0437514+262358	HT Tau	6.423 ± 0.143		12.859 ± 1.000	8.635 ± 0.026	7.542 ± 0.018	7.129 ± 0.018
0438285+261048	DO Tau	3.965 ± 0.050	1.706 ± 0.062		9.470 ± 0.022	8.243 ± 0.033	7.303 ± 0.017
0438352+261038	HV Tau	7.162 ± 0.264			9.227 ± 0.023	8.284 ± 0.026	7.906 ± 0.024
0439174+224753	VY Tau A	6.376 ± 0.123		13.385 ± 0.081	9.970 ± 0.023	9.260 ± 0.021	8.958 ± 0.020

Table 3.2: continued.

IRC name[a]	Identifier	*S9W*[b] [mag]	*L18W*[c] [mag]	UCAC[d] [mag]	2MASS *J* [mag]	2MASS *H* [mag]	2MASS K_S [mag]
0439178+222103	LkCa 15	5.834 ± 0.109	4.117 ± 0.123	11.875 ± 0.128	9.424 ± 0.020	8.600 ± 0.018	8.163 ± 0.018
0439208+254501	GN Tau B	5.405 ± 0.149	3.515 ± 0.027	15.465 ± 0.900	10.196 ± 0.025	8.893 ± 0.026	8.060 ± 0.027
0439557+254501	IC2087 IRS	2.631 ± 0.077	0.839 ± 0.084		10.668 ± 0.023	8.052 ± 0.018	6.275 ± 0.018
0440080+260524	IRAS 04370+2559	5.278 ± 0.237	3.081 ± 0.361		12.406 ± 0.023	10.248 ± 0.029	8.869 ± 0.018
0441168+283959	CoKu Tau/4		3.532 ± 0.069	14.771 ± 0.135	10.163 ± 0.030	9.077 ± 0.024	8.656 ± 0.019
0441387+255624	IRAS 04385+2550	5.488 ± 0.046	2.745 ± 0.039		11.849 ± 0.023	10.123 ± 0.022	9.200 ± 0.018
0442077+252310	V955 Tau A	4.937 ± 0.041	3.270 ± 0.018		9.811 ± 0.022	8.601 ± 0.021	7.942 ± 0.016
0442210+252033	CIDA-7	7.088 ± 0.058			11.397 ± 0.023	10.575 ± 0.022	10.169 ± 0.018
0442376+251537	DP Tau	4.898 ± 0.058	2.641 ± 0.056	15.058 ± 0.900	10.995 ± 0.021	9.689 ± 0.017	8.760 ± 0.016
0446530+165959	DQ Tau	5.093 ± 0.031	2.820 ± 0.065	13.253 ± 0.180	9.511 ± 0.021	8.544 ± 0.020	7.981 ± 0.021
0446590+170238	Haro 6-37 A	4.597 ± 0.019	2.747 ± 0.064	13.655 ± 1.000	9.239 ± 0.028	7.991 ± 0.021	7.310 ± 0.024
0447062+165842	DR Tau	3.552 ± 0.020		12.187 ± 0.410	8.845 ± 0.024	7.799 ± 0.053	6.874 ± 0.017
0447485+292511	DS Tau	5.621 ± 0.085	4.245 ± 0.050	12.490 ± 0.165	9.465 ± 0.018	8.597 ± 0.033	8.036 ± 0.029
0451473+304712	UY Aur A	3.479 ± 0.018	1.152 ± 0.016	12.151 ± 0.137	9.134 ± 0.020	7.987 ± 0.016	7.239 ± 0.018
0452066+304717	IRAS 04489+3042	5.826 ± 0.067	3.246 ± 0.041		14.426 ± 0.030	12.021 ± 0.021	10.383 ± 0.018
0452096+303744	Haro 6-39	7.023 ± 0.181	4.539 ± 0.110		13.254 ± 0.021	12.117 ± 0.018	11.187 ± 0.018
0455095+182629	HD 31281	7.221 ± 0.257		9.105 ± 0.088	7.974 ± 0.027	7.681 ± 0.017	7.609 ± 0.029
0455110+302159	GM Aur	6.793 ± 0.063	3.338 ± 0.131		9.341 ± 0.018	8.603 ± 0.024	8.283 ± 0.017
0455458+303303	AB Aur	1.185 ± 0.016	-0.841 ± 0.026	7.543 ± 0.157	5.936 ± 0.018	5.062 ± 0.020	4.230 ± 0.016
0455560+303622	XEST26-062	6.521 ± 0.154	4.230 ± 0.089	15.339 ± 0.054	10.471 ± 0.021	9.660 ± 0.018	9.267 ± 0.019
0455593+303401	SU Aur	3.445 ± 0.016	0.671 ± 0.017	9.057 ± 0.027	7.199 ± 0.020	6.558 ± 0.020	5.990 ± 0.023
0457065+314250	RXJ0457.0+3142	6.108 ± 0.055		10.002 ± 0.081	7.486 ± 0.021	6.756 ± 0.018	6.538 ± 0.023
0503066+252319	V836 Tau	6.378 ± 0.297		13.817 ± 0.203	9.913 ± 0.023	9.077 ± 0.029	8.595 ± 0.019
0505228+253131	CIDA-9	6.337 ± 0.062	4.870 ± 0.021	16.870 ± 1.000	12.808 ± 0.035	11.913 ± 0.043	11.161 ± 0.029
0507495+302404	RW Aur A	3.453 ± 0.047	1.620 ± 0.036	9.878 ± 0.076	8.378 ± 0.024	7.621 ± 0.038	7.020 ± 0.018
0529083+115212	1RXS J052908.4+115207	2.605 ± 0.017	0.168 ± 0.024	9.443 ± 0.049	7.698 ± 0.030	7.103 ± 0.029	6.590 ± 0.029

Table 3.2: continued.

IRC name[a]	Identifier	*S9W*[b] [mag]	*L18W*[c] [mag]	UCAC[d] [mag]	2MASS J [mag]	2MASS H [mag]	2MASS K_S [mag]
0529406+291110	1RXS J052940.9+291058	5.039 ± 0.037		6.260 ± 0.265	5.314 ± 0.020	5.208 ± 0.252	5.028 ± 0.021
0536516+232605	1RXS J053652.7+232600	6.789 ± 0.209		8.591 ± 0.032	7.328 ± 0.029	7.022 ± 0.021	6.913 ± 0.020
0537184+133452	1RXS J053718.4+133453	7.056 ± 0.016		9.377 ± 0.030	8.105 ± 0.024	7.720 ± 0.020	7.593 ± 0.020

[a] The source must be referred to in the literatures by its full name: AKARI-IRC-V1 J0123456+765432, where V1 refers to the version code.

[b] The zero-magnitude flux density is 56.262 Jy for the *S9W* band.

[c] The zero-magnitude flux density is 12.001 Jy for the *L18W* band.

[d] The UCAC magnitude is derived from aperture photometry.

Table 3.3: AKARI (FIS) photometric data for the previously known Taurus members.

FIS name[a]	Identifier	FLUX65 [Jy]	FLUX90 [Jy]	FLUX140 [Jy]	FLUX160 [Jy]
0413547+281129	IRAS 04108+2803 A	5.85 ± 0.40	7.39 ± 0.50	9.40 ± 2.45	7.58 ± 1.66
0413580+291818	IRAS 04108+2910		0.39 ± 0.04		
0414129+281229	V773 Tau		0.85 ± 0.07		
0414148+282801	FN Tau		1.31 ± 0.09		
0414172+281102	CW Tau		1.63 ± 0.12		
0414263+280559	IRAS 04113+2758 A	10.65 ± 0.79	13.11 ± 0.31		12.56 ± 0.88
0415425+290959	SST Tau 041542.7+290959		1.26 ± 0.06		
0418323+283112	IRAS 04154+2823		1.95 ± 0.10		
0418410+281921	V892 Tau	57.20 ± 1.67	39.04 ± 1.64		
0418415+282721	LR1		1.09 ± 0.10		
0419025+281922	V410 X-ray 6		0.28 ± 0.05		
0420268+280409	SST Tau 042026.0+280408		0.42 ± 0.02		
0421557+275509	DE Tau		1.10 ± 0.09		
0422013+265730	FS Tau B	6.83 ± 0.46	7.98 ± 0.54	8.02 ± 2.53	5.41 ± 1.10
0422551+282348	NSV 1577		2.23 ± 0.04	3.05 ± 0.98	
0423078+280553	IRAS 04200+2759		0.45 ± 0.09		
0423394+245618	FT Tau		0.84 ± 0.04		
0424446+261016	IRAS 04216+2603		1.07 ± 0.07		
0426528+260704	FV Tau		1.70 ± 0.15	3.37 ± 5.16	5.57 ± 0.99
0427042+260616	DG Tau A	21.26 ± 0.77	23.99 ± 0.86	37.03 ± 7.30	
0427569+261922	IRAS 04248+2612	4.23 ± 1.05	5.20 ± 0.52	13.27 ± 3.97	18.05 ± 2.29
0429051+264910	IRAS 04260+2642		1.30 ± 0.16		
0429236+243315	GV Tau			46.70 ± 7.25	

Table 3.3: continued.

FIS name[a]	Identifier	FLUX65 [Jy]	FLUX90 [Jy]	FLUX140 [Jy]	FLUX160 [Jy]
0429304+243950	IRAS 04264+2433			4.75 ± 0.62	
0429516+260649	IQ Tau		0.71 ± 0.07		
0430446+260122	DK Tau		0.98 ± 0.13		
0430506+230010	IRAS 04278+2253	6.04 ± 0.11	6.17 ± 0.07	7.83 ± 0.75	
0430516+244145	ZZ Tau IRS		2.60 ± 0.22		
0431507+242423	HK Tau		2.59 ± 0.15		
0432154+242900	Haro 6-13	5.56 ± 0.15	7.15 ± 0.59	11.87 ± 1.31	11.66 ± 3.08
0432315+241959	FZ Tau		1.12 ± 0.08		
0432319+225730	IRAS 04295+2251	3.66 ± 0.89	3.90 ± 0.17	5.61 ± 2.42	7.38 ± 1.54
0432422+255226	UZ Tau A		2.24 ± 0.36		
0433065+240951	V807 Tau		1.05 ± 0.20		
0433141+261449	IRAS 04301+2608		0.43 ± 0.05		
0433162+225321	IRAS 04302+2247	5.31 ± 0.14	8.36 ± 0.29	12.49 ± 1.52	
0433188+224634	IRAS 04303+2240		1.21 ± 0.01		
0433346+242111	GK Tau	1.94 ± 0.15	1.44 ± 0.21		
0433391+252039	DL Tau		1.27 ± 0.11		
0433520+225032	CI Tau		2.31 ± 0.23	4.37 ± 0.12	
0433546+261336	IT Tau		0.33 ± 0.03		
0434170+225042	CFHT-1			1.96 ± 0.23	
0434554+242853	AA Tau		1.19 ± 0.06		
0435274+241459	DN Tau		0.76 ± 0.11		
0435472+225030	HQ Tau		1.21 ± 0.09		
0435529+225428	HP Tau	6.59 ± 0.58	10.27 ± 0.39	15.16 ± 2.39	13.27 ± 1.96
0436488+241320	HD 283759		0.74 ± 0.09		

Table 3.3: continued.

FIS name[a]	Identifier	FLUX65 [Jy]	FLUX90 [Jy]	FLUX140 [Jy]	FLUX160 [Jy]
0438289+261049	DO Tau	4.53 ± 0.32	5.16 ± 0.12	4.99 ± 1.37	
0439177+222101	LkCa 15		1.27 ± 0.15		
0439557+254507	IC2087 IRS	7.20 ± 0.55	10.55 ± 0.90	10.71 ± 2.65	21.89 ± 1.92
0441388+255623	IRAS 04385+2550		3.00 ± 0.12		
0442073+252306	LkHa332/G1		2.93 ± 0.09	6.88 ± 2.88	
0442206+252041	CIDA-7		0.54 ± 0.05		
0442380+251531	DP Tau		0.60 ± 0.05		
0443026+252012	GO Tau		0.60 ± 0.10		
0346298+242554	1RXS J034629.2+242605		0.82 ± 0.10		
0529082+115224	1RXS J052908.4+115207	32.46 ± 6.60	24.59 ± 1.15	19.40 ± 1.54	
0455460+303320	AB Aur		98.55 ± 1.57	48.54 ± 6.90	76.53 ± 11.78
0505225+253132	CIDA-9		0.57 ± 0.12		
0441168+284001	CoKu Tau/4		1.21 ± 0.16		
0433488+181014	DM Tau		0.68 ± 0.14		
0446528+170004	DQ Tau		1.28 ± 0.05		
0447064+165844	DR Tau	4.66 ± 0.46	5.91 ± 0.41		
0432303+173138	GG Tau A	2.21 ± 0.40	4.49 ± 0.23	9.00 ± 0.42	
0455108+302200	GM Aur		2.90 ± 0.23		
0446593+170241	Haro 6-37 A		1.07 ± 0.10		
0445512+155536	HD 30171		1.34 ± 0.15		
0431382+181408	HL Tau	68.59 ± 3.93	75.93 ± 3.32	67.33 ± 13.85	89.12 ± 10.80
0433392+175151	HN Tau		0.83 ± 0.10		
0421429+193420	IRAS 04187+1927		0.68 ± 0.09	3.76 ± 0.66	
0452068+304717	IRAS 04489+3042	1.91 ± 0.17	2.28 ± 0.14		

Table 3.3: continued.

FIS name[a]	Identifier	FLUX65 [Jy]	FLUX90 [Jy]	FLUX140 [Jy]	FLUX160 [Jy]
0404433+261904	L1489 IRS	44.22 ± 3.52	40.39 ± 1.04	46.51 ± 12.85	60.75 ± 8.54
0431341+180819	L1551 IRS5		463.24 ± 7.12	282.65 ± 50.14	
0507494+302410	RW Aur A	2.10 ± 0.14	2.41 ± 0.20		
0531465+121748	RXJ0531.8+1218		0.76 ± 0.09		
0455593+303403	SU Aur	9.89 ± 0.81	8.80 ± 0.75	10.23 ± 2.58	
0421592+193216	T Tau	120.71 ± 3.91	97.35 ± 26.51	103.00 ± 10.17	112.87 ± 9.80
0430043+181347	UX Tau C	2.82 ± 0.30	2.56 ± 0.19	4.15 ± 0.72	
0451475+304711	UY Aur A	5.49 ± 0.37	7.16 ± 0.16	5.06 ± 2.27	

[a] The source must be referred to in the literatures by its full name: AKARI-FIS-V1 J0123456+765432, where V1 refers to the version code.

3.1.1 Comparisons to the traditional IRAS survey

In the 132 IRC detected TTSs, 46 sources have no counterparts in the IRAS PSC with *FQUAL12* = 3 or *FQUAL25* = 3, within the positional accuracy of 60″, the IRAS spatial resolution. These 'new detections' are achieved because of the higher sensitivity and spatial resolution of AKARI compared to IRAS. Figure 3.2 shows that the detection limit for the previously known Taurus TTSs in the *S9W* band has been improved: IRAS was able to detect almost all the TTSs with brighter than 6 and 4 magnitudes at *S9W* and *L18W* band, respectively, but only about a quarter of the fainter sources. Figure 3.3 shows the $(K_S - S9W)$ vs. $(S9W)$ colour-magnitude diagram of the AKARI detected sources. About half of the sources not detected by IRAS have relatively blue colours at $K_S - S9W < 1$. In contrast, most of the IRAS-detected TTSs have relatively red colours at $K_S - S9W > 2$. A gap appears to exist at $K_S - S9W \sim 1$. The sources with $K_S - S9W < 1$ are most likely to be WTTSs, because they are known to have weak Hα emission (except for HT Tau, whose Hα equivalent width is not given) and are located near the periphery of the clouds or outside the clouds. AKARI has succeeded in detecting WTTSs with weak excess emission in the sensitive *S9W* band.

On the other hand, 6 TTSs are not catalogued in the IRC PSC to within a 5″ searching radius, but are catalogued in the IRAS PSC to within 60″ radius at the MIR wavelengths. Of these sources, 3 have AKARI counterparts within the positional accuracy of the IRAS. The remaining 3 sources are IRAS 04216+2603, IRAS 04302+2247, and DM Tau. The reasons that these were not detected with the IRC are noted previously.

Next, we compared the FIR sources. In the 79 FIS detected TTSs, 19 sources have no counterpart in the IRAS PSC at FIR wavelengths, within the positional accuracy of 60″. There were 6 TTSs which have IRAS FIR measurements but no FIS ones within 60″. Of these 6 sources, RY Tau was observed only once. The remaining 5 sources have IRAS measurements as weak as $\lesssim 1$ Jy at 60 μm band, and no measurements at 100 μm band with good quality. These sources were thought to be too faint at the FIS bands.

3.1.2 Comparisons to the Spitzer data

Although Spitzer did not make survey the entire region we searched, it observed many sources inside the Taurus molecular cloud and some other sources outside the cloud (e.g., Rebull et al. 2010). Since Spitzer observations have better sensitivity than the AKARI All-Sky Survey, Spitzer has discovered more faint sources as shown in Figure 3.4, which shows the histogram of the IRAC4 band (8 μm) magnitudes of the detected TTSs with Spitzer. The AKARI All-Sky Survey should be able to detect more than ∼90% of the sources of magnitude brighter than 7.5 magnitude in the IRAC4 band, which agrees well with the

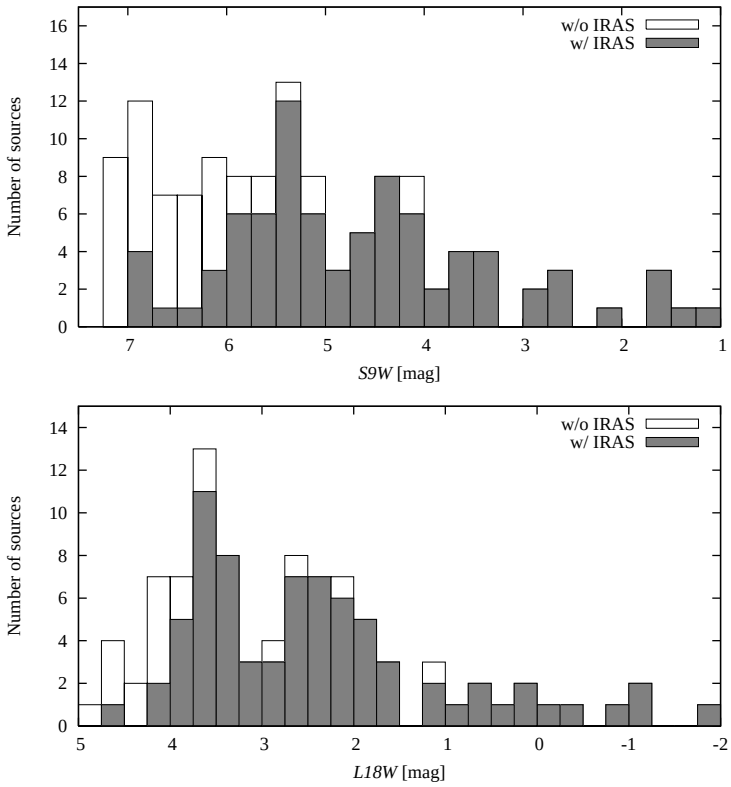

Figure 3.2: Histogram of the *S9W* (*top*) and *L18W* (*bottom*) magnitudes of the TTSs detected with AKARI. The filled and open bars indicate the sources that were detected and not detected with IRAS, respectively. The size of the magnitude bin is 0.25 magnitude.

detection limit of the AKARI *S9W* band of 8 magnitude.

3.2 Selection of AKARI TTS candidates

T Tauri stars were usually found as emission line stars from spectroscopic observations. These observations were limited toward the molecular clouds, and not carried out far from the clouds. After the launch of the X-ray satellite, Einstein Observatory, TTSs were known to have X-ray emission (e.g., Feigelson & DeCampli 1981). The Roentgen Satellite (ROSAT) have revealed that the substantial fraction of WTTSs exist far away from the giant molecular cloud and relatively isolated. The ROSAT detection rate for previously known TTSs are ∼11 % and ∼66 % for CTTSs and WTTSs, respectively (Neuhäuser et al. 1995b). This is because CTTSs have weaker X-ray luminosity than WTTSs, and thus, the survey of the isolated CTTSs was not sufficient.

In this section, we discuss methods for extracting TTS candidates from the AKARI All-Sky data by comparing previously known TTSs with contaminating

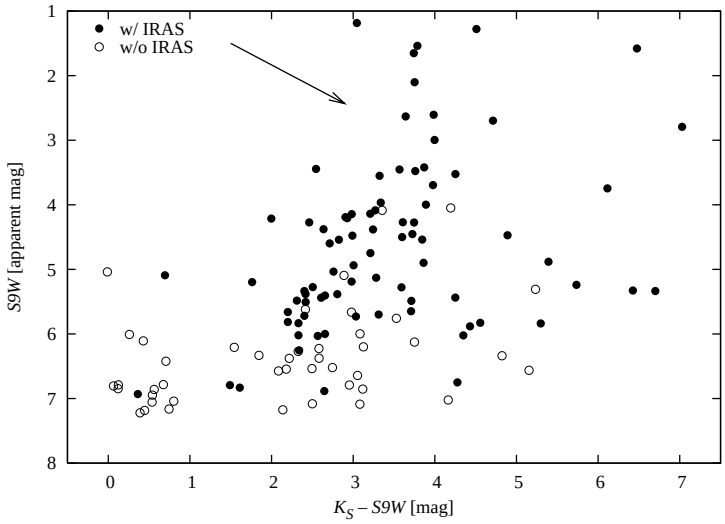

Figure 3.3: $(K_S - S9W)$ vs. $(S9W)$ colour-magnitude diagram of the AKARI-detected PMS stars. The filled and open circles indicate the sources that were detected and not detected with IRAS, respectively. The arrow shows the interstellar extinction vector of $A_V = 20$ mag, using the Weingartner & Draine (2001) Milky Way model of $R_V = 3.1$.

samples. We use the IRC PSC V1, because the sensitivities and the spacial resolutions of the IRC are much better than those of the FIS.

3.2.1 Other types of sources in the whole sky

Since the following types of sources are known to have similar colours to those of the TTSs, we should be able to determine the colour properties of the sources. We considered the four additional catalogues of

1. asymptotic giant branch (AGB) stars of 126 carbon and 563 OH/IR stars (Le Bertre et al. 2003),
2. 326 post-AGB stars (Szczerba et al. 2007),
3. 1143 planetary nebulae (PNe) (Acker et al. 1994), and
4. 2907 extragalactic objects of brighter flux density than 100 mJy in the IRAS 12 μm band (the NASA Extragalactic Database).

In contrast to the TTS case, we examined these sources in the whole sky because of a small number of the sources towards the Taurus-Auriga region.

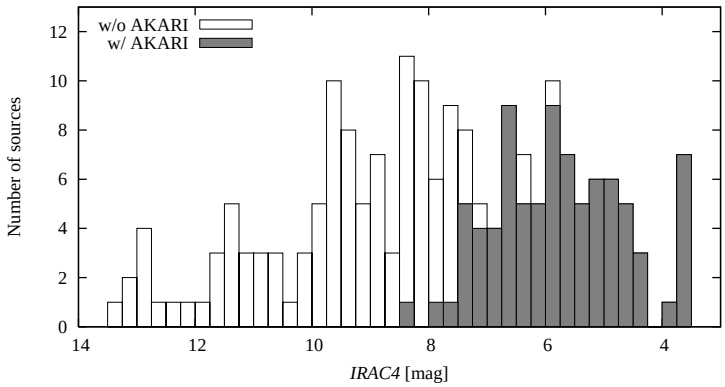

Figure 3.4: Histogram of the *IRAC4* magnitudes of the PMS stars listed in Table 4 by Rebull et al. (2010). The filled and open bars indicate the sources that were detected and not detected with AKARI, respectively. The bin size is 0.25 magnitude.

3.2.2 Removal of AGB stars

Figure 3.5 shows the $(K_S - S9W)$ vs. $(J - K_S)$ and $(K_S - L18W)$ vs. $(J - K_S)$ colour-colour diagrams, where the *S9W* and *L18W* excess emission can be clearly recognized. The other types of the sources, which are stars surrounded with dust, also have significant IR excess emission. Therefore, we need to separate these sources from TTSs in the IRC-PSC.

We first separate almost all carbon and OH/IR stars from the TTSs in the $(S9W - L18W)$ vs. $(J - K_S)$ colour-colour diagram shown in Figure 3.6. Since an AGB star typically has hot (several $\times$ 100 K) dust near its photosphere, the $(S9W - L18W)$ colour, which represents the dust temperature, becomes *blue*. On the other hand, the majority of the dust around a TTS is cold ($\lesssim$ 100–300 K) and the MIR colour is *red*. To remove carbon and OH/IR stars, we propose the first criterion to be

$$J - K_S \leq 7.7 \times (S9W - L18W) - 8.5. \tag{3.1}$$

From this criterion, we remove 12 out of 14 carbon and 4 out of 5 OH/IR stars, which locate in the studied region. However, since post-AGB stars, PNe, and galaxies also have cold dust, they show *red* MIR colour. Thus, we only remove 1 galaxy, laid inside the region. We note that this criterion is valid for the sources that were detected in both the *S9W* and *L18W* bands. We do not remove the sources that were detected in only one band. Although we removed one previously known TTS, IRAS 04262+2735, from this criterion, this source is a *possible new member* from Rebull et al. (2010). After this criterion, the contamination rate, from other types of IR excess sources, reduced from 34 % to 28 % inside the studied region (see Table 3.4).

3.2.3 Removal of post-AGB stars, PNe, and galaxies

Secondly, we can separate post-AGB stars, PNe, and galaxies from TTSs in the $(UCAC - J)$ vs. $(UCAC)$ colour-magnitude diagram. Owing to the low luminosities of PNe (white dwarfs) and galaxies at the visible wavelengths, we can remove all 6 PNe and 36 out of 38 galaxies toward the Taurus region, by the applying the 2nd criterion

$$UCAC \leq 1.5 \times (UCAC - J) + 10. \tag{3.2}$$

We can also remove 2 out of 5 post-AGB stars using this criterion. Considering the detection limits of the IRC PSC and the UCAC, this method seems effective only for extracting nearby ($\lesssim$ 100 pc) young sources. We note that we never identify TTSs with their edge-on disks, because they are not optically visible. From this criterion, two TTSs, CFHT-BD-Tau 21 and CIDA 9, are removed because of relatively low luminosity, and other 45 sources do not have UCAC photometry. The contamination rate becomes 9 % (see Table 3.4).

3.2.4 Selection of TTSs

Figure 3.8 shows the same colour-colour diagrams as in Figure 3.5, but for the remaining sources that could not be removed by the criteria (3.1) and (3.2); most of the remaining sources with the excess emission are the TTSs. Finally, we propose the following two criteria to select most of the TTSs affected by less contamination than other types of sources:

$$-11.5 \leq (J - K_S) - 2.5 \times (K_S - S9W) \leq -2.5 \quad \&\& \, 0.5 \leq J - K_S \leq 3.5, \tag{3.3}$$

$$-12 \leq (J - K_S) - 1.9 \times (K_S - L18W) \leq -5 \quad \&\& \, 0.5 \leq J - K_S \leq 3.5. \tag{3.4}$$

We note that we are unable to identify TTSs that have weak MIR excess emission, because they are contaminated by field normal stars. Consequently, only 2 post-AGB stars and 1 galaxy are remained. Of the 132 AKARI-detected known TTSs, 68 sources (51 CTTSs and 13 WTTSs, the remaining 4 sources have no Hα measurement) pass these criteria. The final contamination rate is 4 % (see Table 3.4). Since there are 130 CTTSs and 269 WTTSs in the original 516 previously known TTSs, the selection rate is ~40% for the CTTS and ~5% for the WTTS, and our selection are biased to the CTTSs.

Table 3.4: Number of IR excess sources and the contamination rate, toward the Taurus region, with our criteria, applying sequentially

	initial number	criterion 1	criterion 2	criterion 3
TTS	132	131	84	68
carbon star	14	2	2	0
OH/IR star	5	1	1	0
post-AGB star	5	5	3	2
Planetary Nebula	6	6	0	0
galaxy	39	38	2	1
contamination rate	34 %	28 %	9 %	4 %

3.3 New TTS candidates

3.3.1 Evaluation of the criteria

On the basis of our criteria, we selected 176 sources out of 14 725 AKARI IRC sources, which are distributed in the area between $2^{h}40^{m}$ and $5^{h}40^{m}$ in right ascension and between 0° and 40° in declination. To verify our criteria, we searched for these sources in SIMBAD with a 10″ searching radius. In the 176 selected sources, 150 sources were found in the SIMBAD database: there were 117 YSOs, 4 Be stars, 10 AGB stars, 1 galaxy, and 18 other types of objects (variable or emission line stars). We note that one TTS, 2MASS J04135737+2918193 have angular separation of $\sim 14''$ between the IRC PSC and the SIMBAD. However, this value becomes $\sim 1''$ when we compare with the 2MASS PSC. Since ∼80 % of the SIMBAD-identified sources were YSOs, we assume the TTS-identification probability based on our criteria to be 80 %, though that is of course affected by the completeness of the SIMBAD database. The difference of probability between the one we determined in previous section and the one from the SIMBAD database seems to come from the incompleteness of other types of sources with IR excess emission, we used. We also note that this probability would be changed by the region. Of the remaining 26 sources, 7 sources have SIMBAD entry but no information nor researches were given. The other 19 sources could not be found. We, then, considered these 26 sources as new TTS candidates. Figure 3.9 shows the distribution of the previously known YSOs and the 26 new TTS candidates, which were selected by our criteria.

3.3.2 Comparison with other methods

Many astronomers have discussed the criteria to extract YSO candidates from their surveyed data. Evans et al. (2009) and Rebull et al. (2010) surveyed YSOs in nearby clouds using Spitzer. Evans et al. (2009) surveyed 5 clouds (15.5 deg^2

region in total) and listed ∼1000 YSO candidates based on the colour-magnitude and colour-colour diagrams by 2MASS and Spitzer. They showed that there might be 51 galaxies among their YSO candidates. However, since their surveyed areas are highly embedded ($A_V > 2$) and located at high Galactic latitudes, they paid less attention to AGB stars. Rebull et al. (2010) surveyed a ∼44 deg^2 region of the Taurus molecular cloud, and listed 148 new candidate Taurus members based on colours and magnitudes drawn from the 2MASS and Spitzer datasets and the images of SDSS and CFHT. Of these 148 new candidates, they performed follow-up spectroscopic observations of about a half of the sources, and confirmed 47 new Taurus members, 7 extragalactic objects, and 1 Be star; additional follow-up observations shall also be performed for the remaining 93 sources.

These two studies have higher (973/1024, Evans et al. 2009; 47/55, Rebull et al. 2010) YSO-identification probabilities than our probability of ∼80 %. This is mainly because we have data for only 2 bands at 9 μm and 18 μm wavelengths; they have more than 4 bands for 3–24 μm wavelengths in many cases. Furthermore, because the detection limits of the AKARI All-Sky Survey shallower than those of the pointed observations of Spitzer, it is difficult to detect MIR faint objects. However, since AKARI has observed almost the whole sky, we have been able to identify TTS candidates towards all nearby star-forming regions.

3.3.3 Characteristics of the New TTS Candidates

Considering that we have 26 new TTS candidates and the YSO-identification probability is ∼80%, we would expect to find ∼20 new TTSs. The infrared properties of the 26 TTS candidates are listed in Table 3.5.

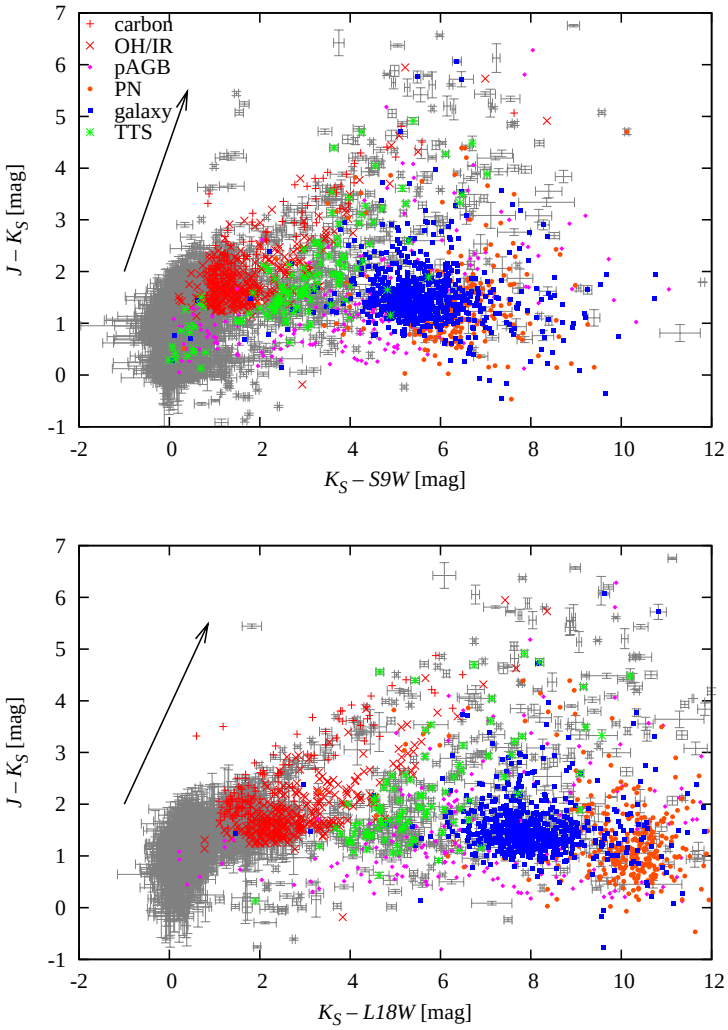

Figure 3.5: *Top*: $(K_S - S9W)$ vs. $(J - K_S)$ colour-colour diagram. The grey dots with error bars indicate all the AKARI point sources in the selected Taurus-Auriga region. The red plus and cross symbols show carbon and OH/IR stars in the whole sky, respectively. The magenta diamonds, the orange circles, and the blue squares are post-AGB stars, PNe, and extragalactic objects in the whole sky, respectively. The green stars mean the TTSs in the Taurus-Auriga region. The arrow shows the interstellar extinction vector of $A_V = 20$ mag, estimated from the Weingartner & Draine (2001) Milky Way model of $R_V = 3.1$. *Bottom*: $(K_S - L18W)$ vs. $(J - K_S)$ colour-colour diagram. The symbols and arrow are the same as in the *top* panel.

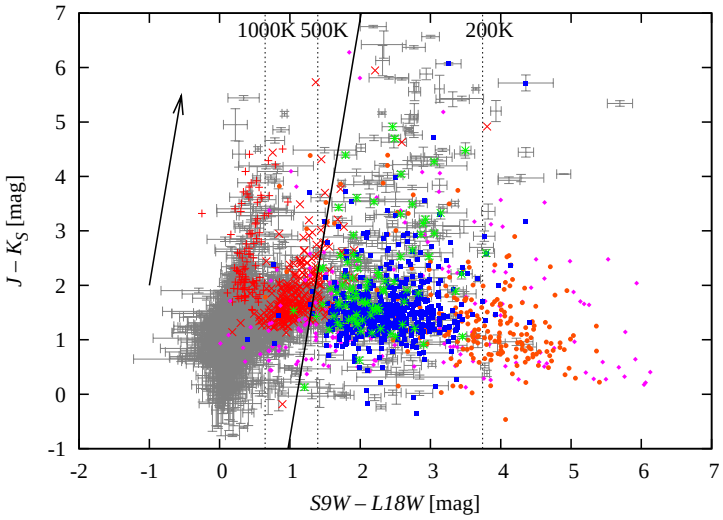

Figure 3.6: $(S9W - L18W)$ vs. $(J - K_S)$ colour-colour diagram. The symbols and arrow are the same as in Figure 3.5. The black solid line indicates our criterion (1). The black broken lines indicate $S9W - L18W$ colours of 200, 500, and 1000 K blackbody.

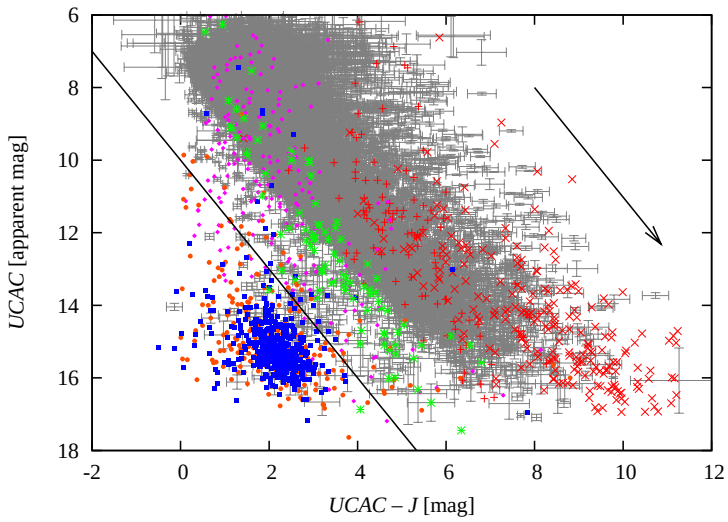

Figure 3.7: $(UCAC - J)$ vs. $(UCAC)$ colour-magnitude diagram. The symbols are the same as in Figure 3.5. The arrow shows the interstellar extinction vector of $A_V = 5$ mag, estimated from the Weingartner & Draine (2001) Milky Way model of $R_V = 3.1$. The black line indicates our criterion (2).

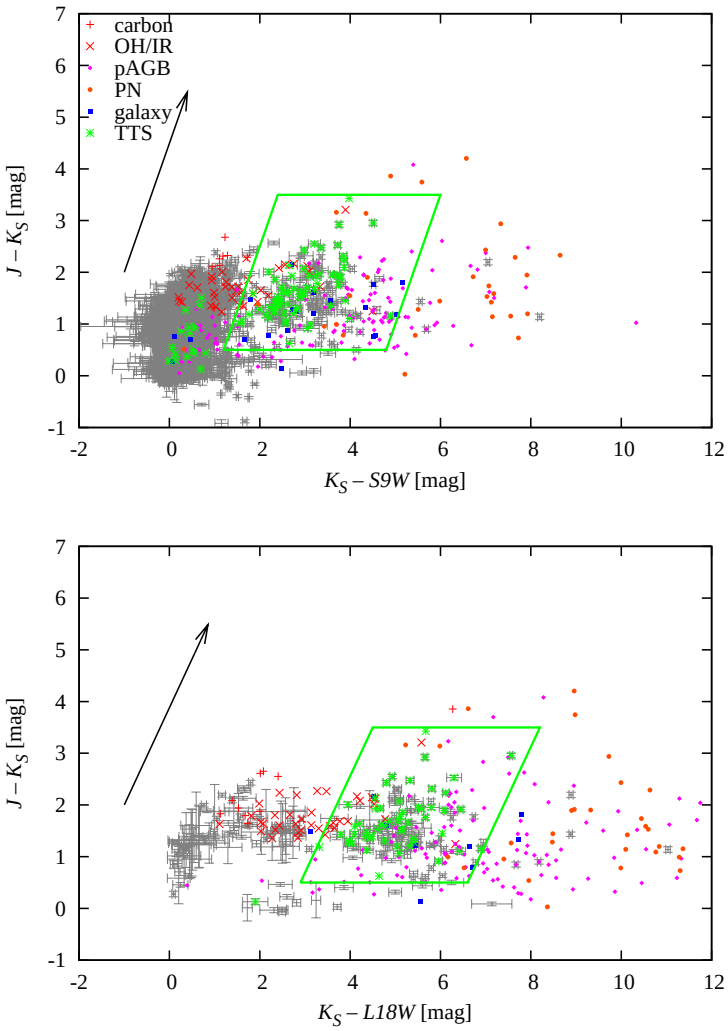

Figure 3.8: Colour-colour diagrams, the same as in Figure 3.5, but for the selected sources with the criteria (3.1) and (3.2) in the text. The green parallelograms indicates our criteria (3) and (4).

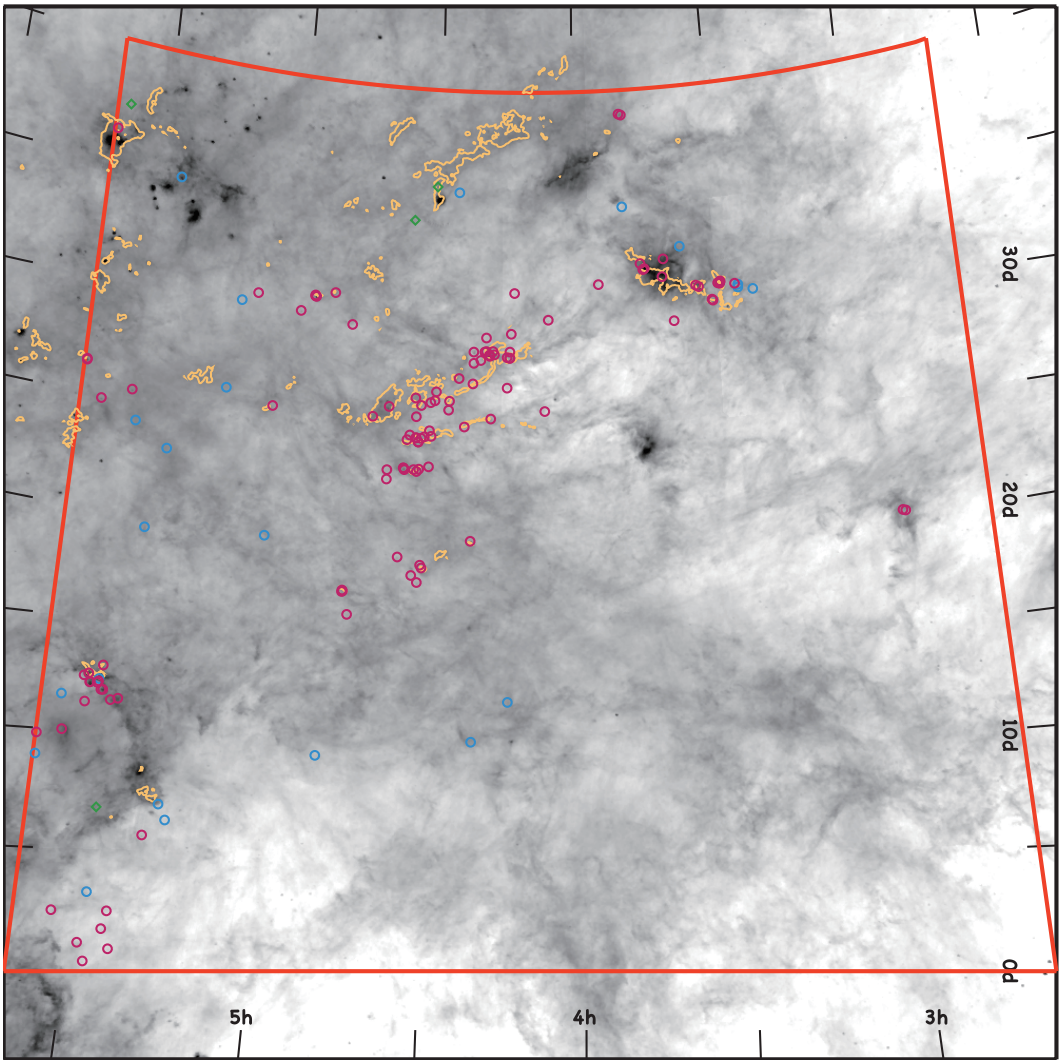

Figure 3.9: The spacial distribution of the TTSs, which were selected by out criteria. The magenta circles are previously known YSOs, and the cyan ones are the new TTSs. The green diamonds are sources selected as new TTS candidates, but not TTSs. The grey scale is IRAS 100 μm map, and the contour represents the extinction of $A_V = 2$ (Dobashi et al. 2005).

Table 3.5: AKARI, UCAC, and 2MASS photometric data for the new TTS candidates.

IRC name[a]	*S9W*[b] [mag]	*L18W*[c] [mag]	UCAC[d] [mag]	2MASS J [mag]	2MASS H [mag]	2MASS K_S [mag]
0322025+305129	5.761 ± 0.077		10.027 ± 0.022	8.227 ± 0.018	7.850 ± 0.020	7.663 ± 0.020
0325067+310652	6.473 ± 0.111	3.546 ± 0.125	12.613 ± 0.060	9.684 ± 0.022	8.930 ± 0.021	8.438 ± 0.018
0325125+305922	6.589 ± 0.154		13.913 ± 0.086	10.243 ± 0.021	9.414 ± 0.021	9.067 ± 0.020
0337114+330303	6.441 ± 0.109	4.488 ± 0.108	13.630 ± 0.212	10.631 ± 0.023	9.746 ± 0.021	9.223 ± 0.018
0349290+345800	6.227 ± 0.097	4.400 ± 0.242	13.742 ± 0.114	10.933 ± 0.022	10.082 ± 0.016	9.504 ± 0.018
0414187+115812	6.330 ± 0.180	4.291 ± 0.194	12.456 ± 0.104	10.128 ± 0.022	9.554 ± 0.022	9.205 ± 0.018
0421156+100722	6.732 ± 0.101		11.685 ± 0.064	9.107 ± 0.020	8.409 ± 0.047	8.168 ± 0.026
0425412+353718		3.786 ± 0.254	13.669 ± 0.112	11.172 ± 0.021	10.545 ± 0.022	10.069 ± 0.017
0430375+355031	6.264 ± 0.178	3.827 ± 0.241	16.213 ± 0.372	10.027 ± 0.021	8.874 ± 0.018	8.052 ± 0.019
0435254+341901	6.208 ± 0.063	4.073 ± 0.163	15.805 ± 0.339	11.566 ± 0.022	10.339 ± 0.028	9.503 ± 0.021
0450190+092328	4.337 ± 0.033	2.876 ± 0.032	12.323 ± 0.900	7.118 ± 0.024	6.253 ± 0.024	5.970 ± 0.024
0502405+192237	4.908 ± 0.029	2.959 ± 0.086	13.449 ± 0.224	8.119 ± 0.030	7.013 ± 0.017	6.576 ± 0.017
0511021+295926	6.684 ± 0.138	4.367 ± 0.045	13.091 ± 0.057	10.063 ± 0.035	9.320 ± 0.041	9.022 ± 0.032
0512342+255847	6.145 ± 0.206		13.313 ± 0.129	10.462 ± 0.022	9.706 ± 0.022	9.411 ± 0.018
0516039+061852	6.807 ± 0.080		14.728 ± 0.112	11.286 ± 0.022	10.463 ± 0.027	9.978 ± 0.018
0517259+070022	5.130 ± 0.045	3.156 ± 0.036	11.000 ± 0.026	9.469 ± 0.039	8.941 ± 0.055	8.424 ± 0.034
0522456+225444		2.467 ± 0.063	13.459 ± 0.114	9.641 ± 0.022	8.693 ± 0.026	8.391 ± 0.017
0525113+191547	6.331 ± 0.101		14.599 ± 0.143	11.309 ± 0.021	10.416 ± 0.026	9.918 ± 0.018
0525519+345228	3.100 ± 0.077	1.520 ± 0.122	14.503 ± 0.155	9.621 ± 0.022	8.499 ± 0.020	7.745 ± 0.023
0527433+031309	7.023 ± 0.067	4.304 ± 0.066	12.163 ± 0.096	10.378 ± 0.023	9.849 ± 0.024	9.708 ± 0.025
0527493+064638	3.568 ± 0.119		14.185 ± 0.231	8.312 ± 0.026	7.290 ± 0.057	6.462 ± 0.021
0529091+235902	5.960 ± 0.116	4.267 ± 0.107	14.452 ± 0.120	11.259 ± 0.024	10.368 ± 0.020	9.784 ± 0.018
0529592+121947		4.078 ± 0.188	12.949 ± 0.119	10.593 ± 0.020	9.836 ± 0.021	9.391 ± 0.018

Table 3.5: continued.

IRC name[a]	*S9W*[b] [mag]	*L18W*[c] [mag]	UCAC[d] [mag]	2MASS J [mag]	2MASS H [mag]	2MASS K_S [mag]
0536009+113339	6.718 ± 0.072		11.543 ± 0.091	9.863 ± 0.026	9.263 ± 0.022	8.980 ± 0.023
0537531+372456	5.511 ± 0.070	3.949 ± 0.035	15.577 ± 0.228	10.543 ± 0.022	9.827 ± 0.026	9.313 ± 0.024
0539023+085612	6.947 ± 0.039		11.170 ± 0.037	9.744 ± 0.024	9.157 ± 0.024	8.736 ± 0.021

[a] The source must be referred to in the literatures by its full name: AKARI-IRC-V1 J0123456+765432, where V1 refers to the version code.

[b] The zero-magnitude flux density is 56.262 Jy for the *S9W* band.

[c] The zero-magnitude flux density is 12.001 Jy for the *L18W* band.

[d] The UCAC magnitude is derived from aperture photometry.

IRAS measurements of the new TTS candidates

Of the 26 new TTS candidates, 11 sources have IRAS measurements within 60″ radius. Harris et al. (1988) suggested the IRAS colours of the TTSs as

$$0.03 < \log(F25/F12) < 0.58 \quad \text{and} \quad -0.26 < \log(F60/F25) < 0.41,$$

using the flux densities at 12, 25, and 60 μm bands.

Of the 11 IRAS detected sources, only 3 sources agree the IRAS TTS selection, and the other 8 sources lies near the boundary. However, there is only 1 source that has qualities of 3 in all the three bands. Although this source does not agree the criteria, their input sources, to determine these criteria, were a little different with ours. Their input sources were based on NH_3 cores, i.e., biased to embedded objects, while we used TTSs without surrounding envelopes, in addition. Hence, we cannot be asserted that that our new TTS candidates would not TTSs.

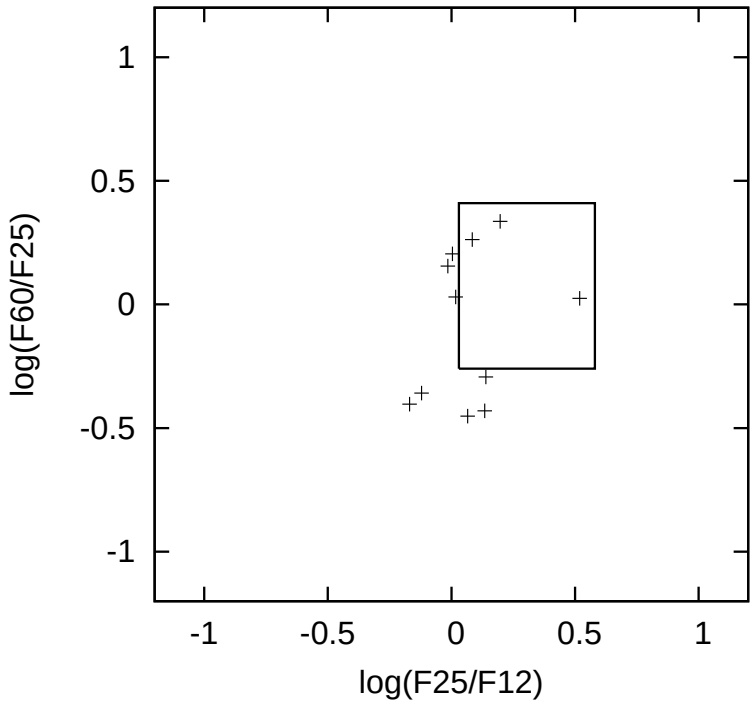

Figure 3.10: Plot of log(F25/F12) vs. log(F60/F25) colours for the new TTS candidates. The box indicates the colour limits of TTSs.

ROSAT measurements of the new TTS candidates

Since the ROSAT survey is one of the most useful tools to find new TTS candidates, we searched 26 new TTS candidates with the ROSAT All-Sky Bright Source Catalogue, but none of them is found. We, furthermore, surveyed using

Table 3.6: IRAS measurements for our new TTS candidates.

	Flux density [Jy]				Quality flag			
AKARI IRC	12	25	60	100	12	25	60	100
0322025+305129	0.2476	0.25	0.4	14.76	1	3	1	1
0325067+310652	0.25	0.8245	0.8735	9.396	1	3	3	1
0414187+115812	0.2921	0.2824	0.4041	6.256	1	3	1	1
0425412+353718	0.2708	0.4262	0.9244	1.791	1	2	3	1
0450190+092328	1.207	0.9134	0.4	1.239	3	3	1	1
0502405+192237	0.7903	1.078	0.4	1.713	3	3	1	1
0517259+070022	0.5693	0.785	0.4	10.65	3	3	1	1
0522456+225444	1.379	1.604	0.5675	1.851	3	3	3	1
0527433+031309	0.25	0.3035	0.555	2.533	1	3	1	1
0527493+064638	2.221	1.504	0.5942	11.86	3	3	1	1
0537531+372456	0.3602	0.375	0.4022	2.558	3	1	1	1

the ROSAT All-Sky Survey Faint Source Catalogue, and found 5 sources within $1'$ searching radius. The X-ray parameters are tabulated in Table 3.7.

Neuhäuser et al. (1995a) developed the criteria to extract TTS candidates by using the Hardness Ratios (HRs) of the ROSAT data. The HR was defined as

$$HR1 = \frac{Z_{h1} + Z_{h2} - Z_S}{Z_{h1} + Z_{h2} + Z_S} \quad \text{and} \quad HR2 = \frac{Z_{h2} - Z_{h1}}{Z_{h2} + Z_{h1}},$$

where Z are the count rates for the ROSAT energy channels of soft (0.1–0.4 keV), hard 1 (0.5–0.9 keV), and hard 2 (0.9–2.1 keV). We can extract TTS candidates by using the following criteria

$$-0.15 < HR1 < 1 \quad \text{and} \quad -0.3 < HR2 < 0.5.$$

Of the 5 ROSAT faint sources, 2 sources satisfy these criteria. Furthermore, considering the large uncertainties of the HRs, these 5 sources agree the TTS criteria. Here, the detection of the X-ray raise the TTS probability for these 5 sources. On the other hand, since the X-ray detection rate of the previously known TTSs are ∼10% and ∼60% for the CTTSs and WTTSs, respectively, we cannot rule out the possibility that the sources which does not have ROSAT measurement are TTSs.

3.3.4 Follow-up Observations of the New TTS Candidates

We obtained follow-up spectroscopic observations for our 26 new TTS candidates. The objectives of the observations were to find Hα emission/absorption

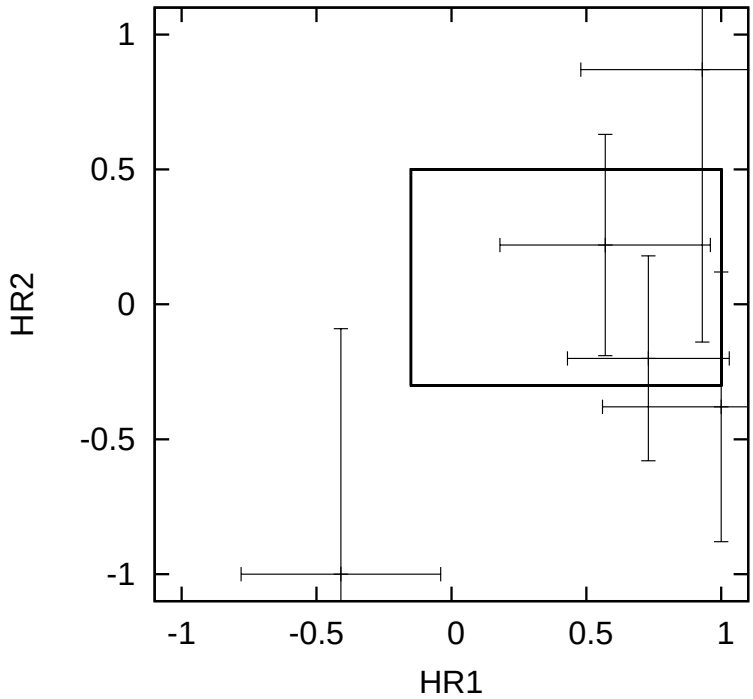

Figure 3.11: HR2 vs. HR1 plot of the ROSAT detected sources. The box shows the selection criteria.

line (6563 Å) and LiI absorption line (6707 Å). Since Li is easily destructed when the stars begin nuclear fusion, the existence of the Li is the most important feature for the stars being young. Usually, the equivalent width of Li (W(Li)) of the Pleiades members are used as Zero-Age-Main-Sequence (ZAMS) stars, and the typical value is ∼0.1 Å.

Data were obtained by the observation run in 2010 Nov 14–18th at the Kitt-Peak National Observatory. We performed intermediate resolution (R ∼3000) spectroscopy at the optical wavelengths of 6000–7000 Å using the Gold Camera on the 2.1 meter telescope. The instrumental settings were a 600 lines mm^{-1} grating blazed at 11000 Å and used at grating angle at 7°.55. The slit width was set to 2″ and the position angle was 90°. For the wavelength calibration, we took spectra of an He-Ne-Ar lamp before every target stars. We used BD+28 4211, Feige 25, and BD+08 2015 as standard stars. The obtained data were reduced using the Image Reduction and Analysis Facility (IRAF)[1]. Since AKARI-IRC-V1 J0337114+330303 are seems to be a binary (the South component locate ∼ 10″ away), we observed both of them, i.e., we observed 27 sources in total. The observed parameters are tabulated at Table 3.8 and the obtained spectra are

[1]IRAF is distributed by the National Optical Astronomy Observatories, which are operated by the Association of Universities for Research in Astronomy, Inc., under cooperative agreement with the National Science Foundation.

Table 3.7: X-ray data for our new TTS candidates from the ROSAT All-Sky Faint Source Catalogue.

AKARI IRC	1RXS	Count [ct/s]	HR1	HR2
0322025+305129	J032201.1+305129	0.0212±0.00902	0.57±0.39	0.22±0.41
0325125+305922	J032511.3+305939	0.0202±0.00793	0.93±0.45	0.87±1.01
0517259+070022	J051726.0+070024	0.0225±0.00868	0.73±0.30	-0.20±0.38
0527433+031309	J052744.2+031329	0.0270±0.00937	1.00±0.44	-0.38±0.50
0527493+064638	J052748.7+064544	0.0248±0.00884	-0.41±0.37	-1.00±0.91

shown in Figure 3.12. We also show the spectra of a previously knwon CTTS, HL Tau, for comparison.

Among the 27 target stars, we have detected significant Li absorption lines in 25 stars. The typical value of W(Li) is 0.3 Å and ranges from 0.04 to 0.57 Å. Although there are 4 Li weak (W(Li) < 0.1) sources, 2 sources are near boundaries of W(Li) ∼0.08 and 0.09, and we consider them as PMS stars. The other 2 sources may be post TTSs. We, then, have 23 PMS stars. This result indicates the usefulness of our TTS criteria by AKARI IRC PSC.

Of the 23 PMS stars, 5 sources have absorption line and 18 sources have emission line (including 7 P Cygni profiles and 1 inverse P Cygni profile) for the Hα. Since the P Cygni profiles are thought to be caused by the cold material that is moving toward us, they would have molecular outflow and are thought to be CTTSs. Furthermore, of the 7 P Cygni profile sources, 2 sources show significant forbidden [OI] emission lines (6300 Å) and 4 sources have probable [OI] emission lines, which come from the shocked region. We note that the [OI] line can be seen in about 20 % of TTSs, and the typical equivalent width is as weak as 1 Å. On the other hand, the inverse P Cygni profile indicates the presence of infalling matterials.

It is now known that W(Hα) varies with time (accretion rate), and it would be underestimated by effects of veiling. White & Basri (2003) proposed the new CTTS/WTTS classification by full width at 10% of the Hα emission profile peak. The full width at 10% of >270 km s^{-1} indicates the presence of accretion disk (i.e., CTTS). Here, we use this criterion to classify our new TTSs. We fitted a Gaussian to the emission line and measured 10% width (see Figure 3.13). For the 8 sources with P Cygni profiles, we used the lower slopes. We note that our intermediate resolution of R ∼3000 represents to velocity resolution of ∼100 km s^{-1}. Considering this relatively large velocity resolution, we consider 3 Hα emitting sources, AKARI-IRC-V1 J0337114+330303 S, 0512342+255847, and 0527433+031309, as WTTSs. Finally, we got 15 CTTSs and 8 WTTSs.

We also tabulated the FIS data for the three new TTSs in Table 3.9.

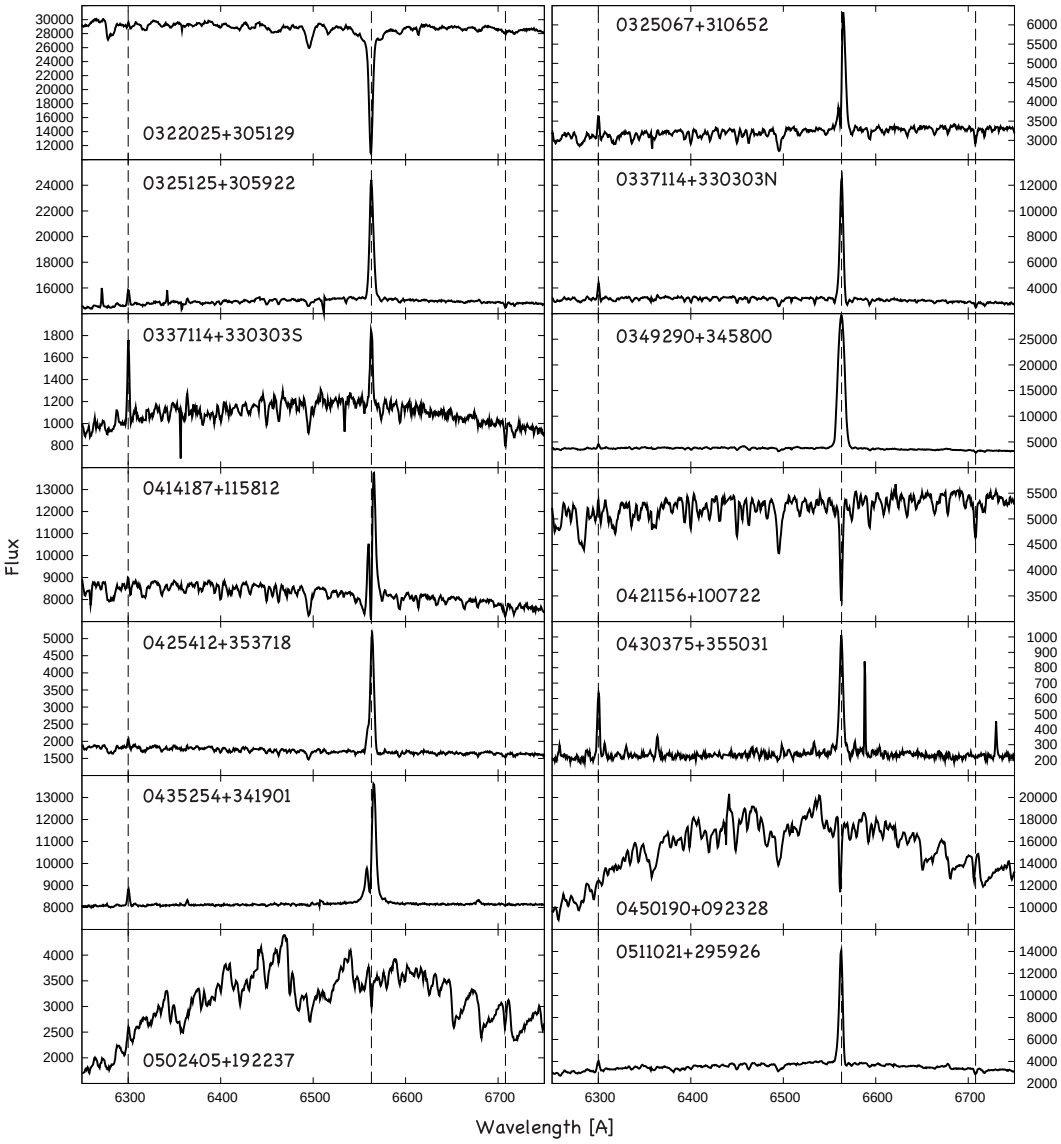

Figure 3.12: Optical spectra for our new TTS candidates.

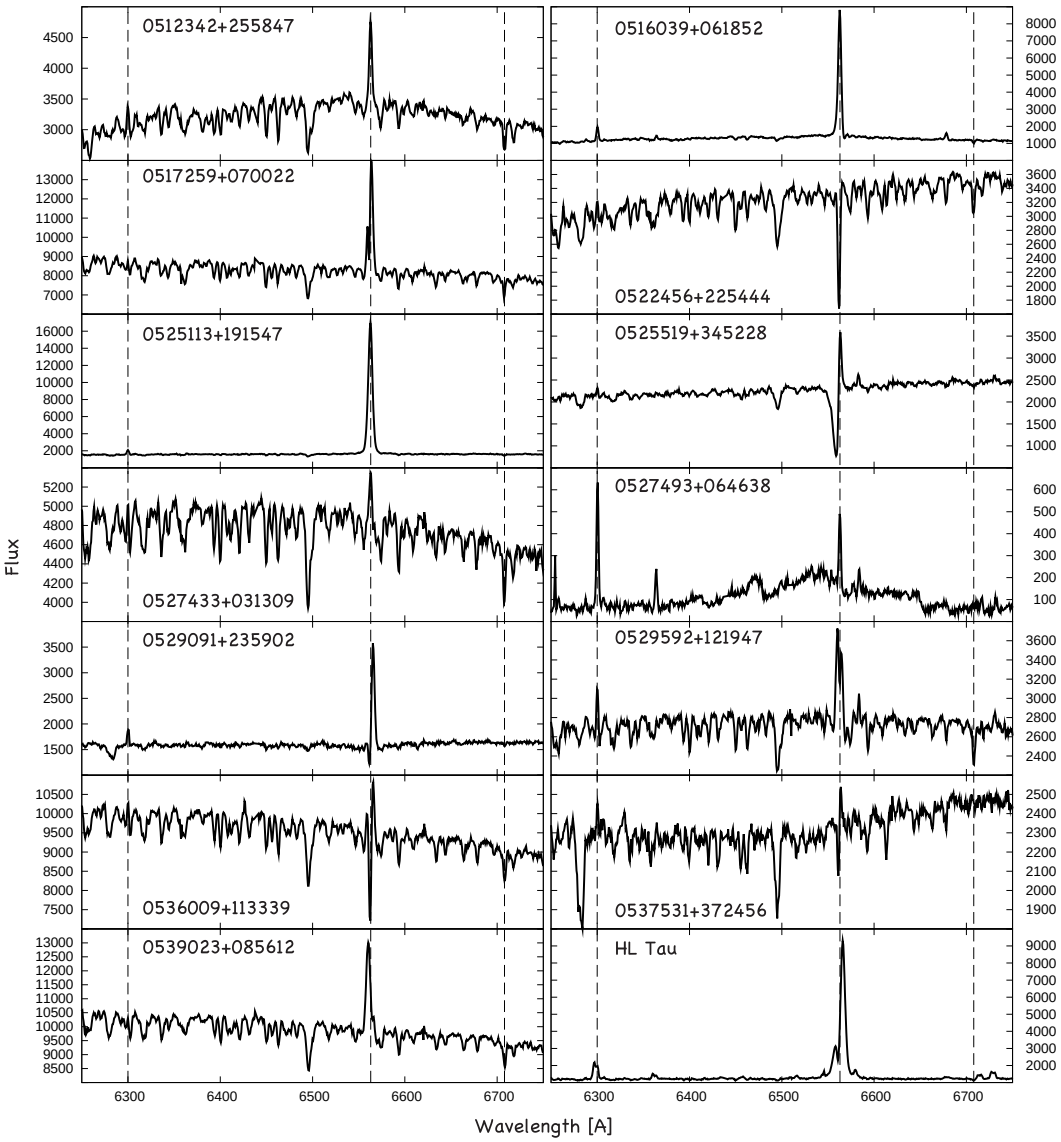

Figure 3.12: *Continued.*

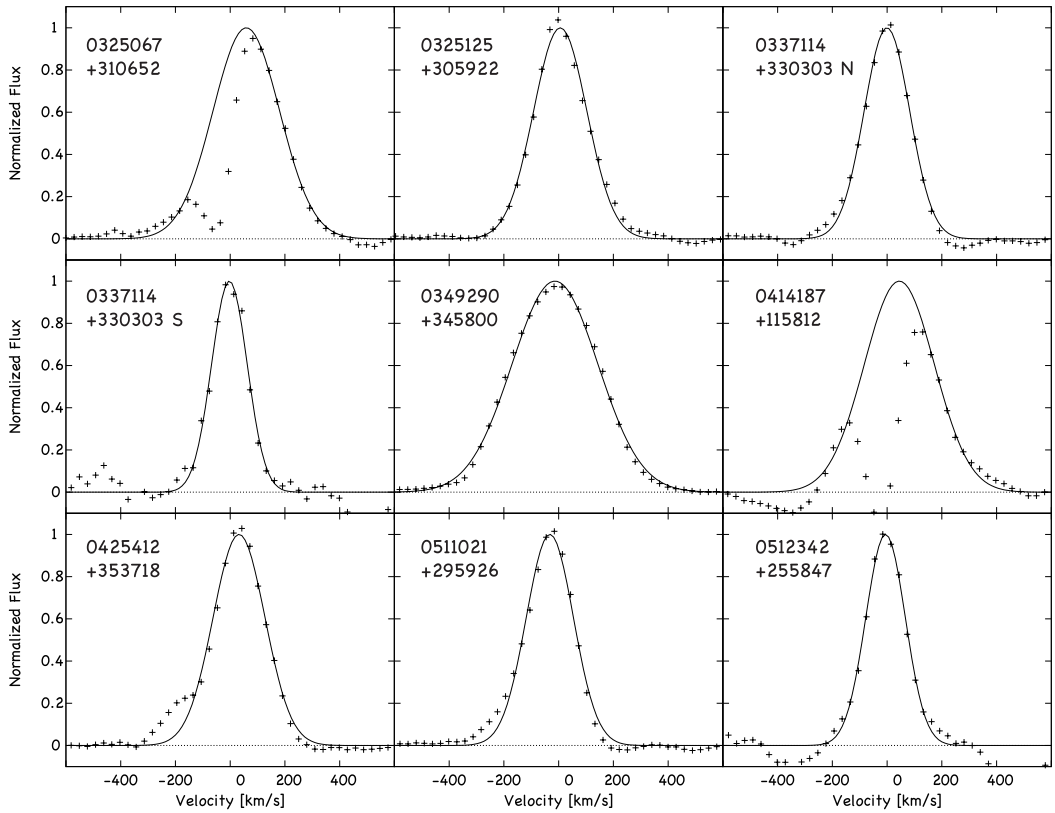

Figure 3.13: Hα velocity profiles for the new TTSs which have emission. The profiles have been continuum-subtracted and normalized to range from 0.0 (continuum level) to 1.0 (emission peak level). The solid curves indicates the fitted Gaussians.

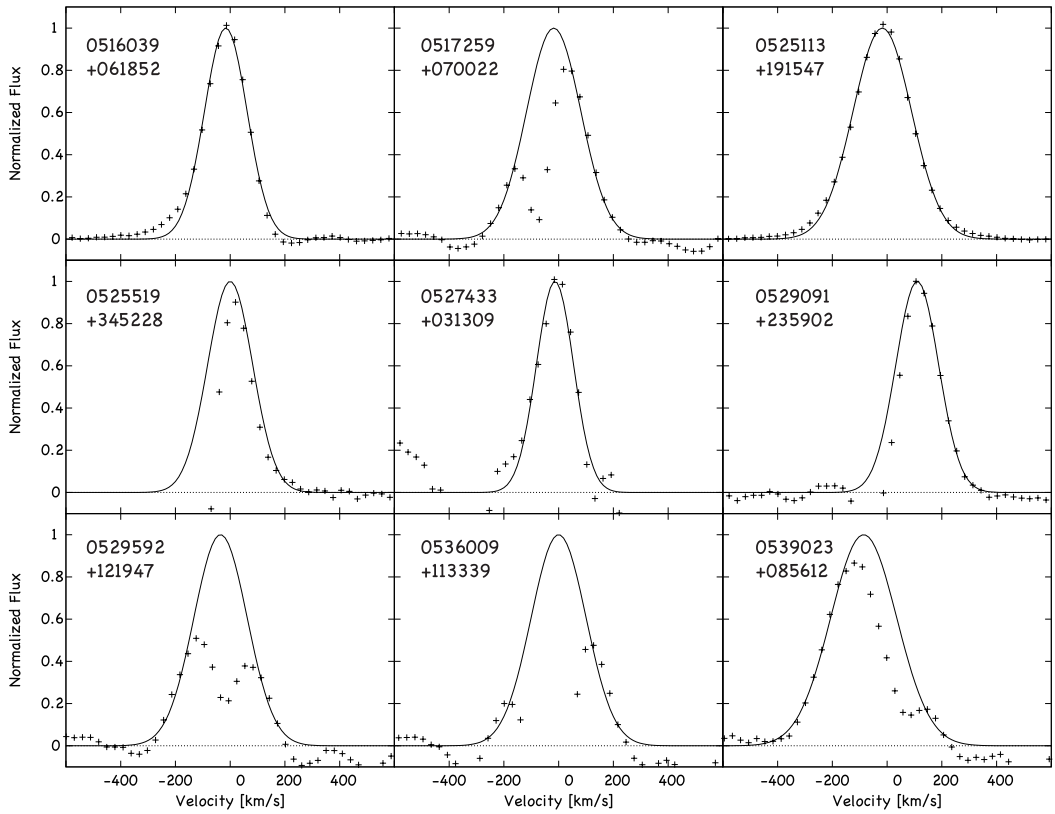

Figure 3.13: *Continued.*

Table 3.8: Observed parameters of the new TTS candidates.

AKARI IRC	Exposure	W(Hα)	10% width	W(Li I)	Sp	comment
	[s]	[Å]	[km s^{-1}]	[Å]		
0322025+305129	1200	4.5	—	0.08	G–K	
0325067+310652	1200	-5.9[a]	522	0.31	G–K	[O I]
0325125+305922	1200	-3.2	417	0.09	G–K	
0337114+330303 N	1800	-17.	357	0.36	G–K	
0337114+330303 S	1800	-3.7	279	0.57	G–K	
0349290+345800	1200	-62.	673	0.37	G–K	
0414187+115812	1200	-4.8[a]	548	0.21	G–K	[O I]?
0421156+100722	1200	1.4	—	0.42	G–K	
0425412+353718	1200	-11.	407	0.18	G–K	
0430375+355031	1800	-19.	—	—	G–K	not TTS
0435254+341901	1800	-5.0[a]	—	0.05	G–K	post TTS?
0450190+092328	1200	1.3	—	0.46	M	
0502405+192237	1200	0.58	—	0.46	M	
0511021+295926	1200	-13.	370	0.48	G–K	
0512342+255847	1200	-2.9	310	0.56	G–K	
0516039+061852	1800	-23.	334	0.50	G–K	
0517259+070022	1200	-4.0[a]	425	0.32	G–K	
0522456+225444	1200	1.6	—	0.43	G–K	
0525113+191547	1800	-57.	458	0.31	G–K	
0525519+345228	1800	2.2[a]	353[c]	0.10	G–K	[O I]?
0527433+031309	1200	-1.4	290	0.37	G–K	
0527493+064638	1800	-6.5	—	—	—	Symbiotic
0529091+235902	1800	-5.2[a]	335	0.11	G–K	[O I]
0529592+121947	1200	-2.8[a]	418	0.45	G–K	[O I]?
0536009+113339	1200	-0.55[a]	431[c]	0.31	G–K	[O I]?
0537531+372456	1800	-0.08[a]	—	0.04	G–K	post TTS?
0539023+085612	1200	-2.0[b]	518	0.31	G–K	

[a] These sources have P Cygni profiles.
[b] This source has an inverse P Cygni profile.
[c] The fitting was done by eye, because of deep absorption.

Table 3.9: AKARI (FIS) photometric data for the new TTSs.

FIS name[a]	IRC name[b]	FLUX65 [Jy]	FLUX90 [Jy]	FLUX140 [Jy]	FLUX160 [Jy]
0325072+310658	0325067+310652		0.58 ± 0.08		
0425410+353723	0425412+353718		0.83 ± 0.07		
0525509+345227	0525519+345228	10.24 ± 1.53	19.45 ± 1.18	36.04 ± 6.58	68.15 ± 12.06

[a] The source must be referred to in the literatures by its full name: AKARI-FIS-V1 J0123456+765432, where V1 refers to the version code.

[b] The source must be referred to in the literatures by its full name: AKARI-IRC-V1 J0123456+765432, where V1 refers to the version code.

Chapter 4

DISCUSSION

4.1 The Origin of the Isolated CTTSs

We have discovered 23 new TTSs, 15 of them locate more than 1 degree (or ∼2.4 pc at distance of 140 pc) away from the clouds ($A_V > 2$). Furthermore, other 171 previously known TTSs are also isolated from the clouds. Three ideas for the origin of the isolated TTSs were suggested (Feigelson 1996);

1. TTSs have moved with their proper motions of Δv ∼1 km s^{-1}, taking over the thermal velocity dispersions of the natal cloud gas (we call 'slow-drifting' TTSs),

2. TTSs were born in cloudlets, and the cloudlets have already dissipated (we call in-situ star formation),

3. TTSs were dynamically ejected with high-velocity by gravitational interactions with other stars.

Since the third mechanism seems to contribute to few isolated TTSs (Feigelson 1996), we consider the former 2 mechanisms.

Feigelson (1996) suggested, for the Chamaeleon region, that if stars have an isotropic Gaussian velocity dispersion with $\Delta v \sim 1\,\mathrm{km\,s^{-1}}$, it is sufficient to explain the spacial distributions of the widely dispersed WTTSs. The proper motions for ∼75 spectroscopic Taurus members (YSOs) were measured by Jones & Herbig (1979). Of their 75 sources, 63 sources were identified as kinematic Taurus members, because they have similar proper motions. The velocity dispersion for these 63 TTSs was ∼2 km s^{-1}, and it is slightly larger. Considering that the TTSs which locate farther from clouds than 1° (∼2.4 pc at distance of 140 pc) are isolated ones, they need higher velocities than 2.4 km s^{-1} to move from their born place within 1 Myr. The probability that the sources have v >2.4 km s^{-1} is ∼12%, with the 2 km s^{-1} velocity dispersion. Of the 516 previously known TTSs, there are 130 CTTSs, and 8 sources locate more than 1 degree away from

the clouds. On the other hand, the predictable number of isolated CTTSs is 15 (130×0.12). This difference might come from the non-isotropic distribution of proper motions, or incomplete sample of isolated CTTSs.

For the second mechanism, we examine 2 cases, that cloudlets are some parts of the Taurus molecular complex or are not related to the complex. If the cloudlets associate with the complex, the velocity dispersion of cloudlets should originate from that of complex. There are a relationship for velocity dispersion and size of molecular cloud, $\Delta v \sim 1.0(R\,\mathrm{pc}^{-1})^{0.5}\,\mathrm{km\,s}^{-1}$ (Larson's low). Since the size of the Taurus complex is ~10 pc, the dispersion is estimated to be ~3 km s^{-1}. If we consider the lifetime of star forming cloudlets as 0.1 Myr (typical lifetime of protostars), it is impossible that cloudlets locate 1 degree away from the complex. Considering this short lifetime of cloudlets, the spatial distribution and proper motion of TTSs are thought to be similar to the first mechanism. However, we note that cloudlets can survive more than 0.1 Myr. On the other hand, if cloudlets are not related to the Taurus complex, the larger velocity dispersion and the scattered proper motion can be acceptable.

Proper motions of the new TTSs

To search for the origin of our 23 TTSs, we obtained the proper motions for our sources with UCAC3. Of the 23 sources, 17 sources have been measured proper motions (see Figure 4.1). Since the new TTSs have significant IR excess emission and TTSs with IR excess emission is relatively young (e.g., Cieza et al. 2007), we used the lifetimes of 1 Myr, which is the typical age of CTTSs. A source, located north of the Taurus molecular cloud has proper motions headed to the north, is thought to be a 'slow-drifting' TTS from the Taurus cloud. There are 5 sources near the IC 348; 3 sources are moving toward north-west, and the other 2 sources toward north-east. Considering the location of the TTSs and IC 348, 3 west headed sources could be originated from IC 348. The dispersions of their proper motions are ~1–2 km s^{-1} or ~3 km s^{-1} assuming the distance of 140 pc or 300 pc (distance to IC 348), respectively. It is consistent to the typical dispersions, although there are only three sources. The other 2 sources seems to be formed in other clouds, considering the directions of their proper motions. Near the λOri region, there are 8 probable 'slow-drifting' TTSs. The dispersions of their proper motions are ~20 km s^{-1} or ~60 km s^{-1} assuming the distance of 140 pc or 450 pc (distance to λOri), respectively. This large dispersion suggests that not all the 8 sources are formed as λOri members, and some of them are quite close to the Earth. The remaining 3 sources would not be related to the famous star forming regions. Therefore, at least 5 sources are thought to be formed in cloudlets.

Origin of the isolated TTSs

How many TTSs are 'slow-drifting'? We checked the proper motions for the 516 previously known TTSs using UCAC3, and 249 sources were measured. Including the new TTSs, 266 TTSs have been measured proper motions. Figure 4.2 shows the proper motions with respect to the Taurus molecular cloud[1] for the previously known 249 sources (not include the new ones). We note that the vectors in Figure 4.2 indicate the movements of the sources for the last 1 Myr (typical time-scale of a CTTS), without care about their ages. We can see that their proper motions are very scattered, except for sources near the Pleiades. Furthermore, we can find 3 other groups (contains more than 5 sources) near L1551, L1495, and L1536. Figure 4.3 shows the histogram of the proper motions. Here, we limit sources with uncertainties of proper motions less than 3 mas yr^{-1} as good sources, and got $\sim$120 out of 266 sources in total. We note that the positional error in 1 Myr time-scale is less than 5$'$ and typically 2$'$.5 for the good sources. The dispersions of the proper motions are calculated as $\sim$1 and $\sim$5 km s^{-1} for Pleiades and L1551 members, respectively. The dispersion of the Pleiades agrees the typical one of $\sim$1 km s^{-1}, but the dispersion of the L1551 is larger, even than the Taurus one. However, the L1551 member may contain some non-member, because we classified by eye. We did not calculate the dispersions for L1495 and L1536 members, because there remained only a few sources. The dispersion, for sources not classified as group members, is estimated to be $\sim$15 km s^{-1}, and it far exceeds the typical value of $\sim$1 km s^{-1}. From these facts, it seems that 'slow-drifted' TTSs are few.

We propose that the large dispersion of proper motion was caused by the inter-cloud velocity distribution. Dutra & Bica (2002) has compiled dark clouds for whole sky, and we found that there are 263 clouds laid inside the region we surveyed. Figure 4.4 shows the spatial distributions of the clouds. Of the 263 clouds, 77 clouds were measured their radial velocities by CO emission line. Figure 4.5 shows the histogram of the radial velocity. The velocity dispersion is estimated to be $\sim$5 km s^{-1}. This dispersion is not comparable to the typical dispersion of the proper motion ($\sim$1 km s^{-1}).

The difference of dispersion is thought to be caused by the availability of the molecular cloud survey. Clouds are originally found as dark clouds, which conceal background stars, and these clouds are located in the Galactic plane. The survey of CO gas was also performed in the Galactic plane region, and thus, clouds are crowded in the Galactic plane. After the IRAS all-sky survey, dust clouds are known to exist at high Galactic latitude (high latitude clouds; HLC). However, since the spatial resolution of IRAS is as large as a few arcmin (at 100 μm wavelength), only HLCs as large as $\sim$ 10$'$ were discovered by IRAS. This circumstance can be seen in Figure 4.4, that small ($<$ 10$'$) clouds locate at low

[1]The proper motions of the Taurus molecular cloud were 6 and -22 mas yr^{-1} for R.A. and Dec. directions, respectively (Jones & Herbig 1979).

latitude ($|b| < 20°$), while large ($> 10'$) clouds are extended to high latitude ($|b| > 20°$).

If we limit the clouds in $|b| < 20°$, there are 193 clouds and 38 of them have the measured CO radial velocity. The velocity dispersion of these clouds is as small as $\sim$2 km s^{-1}, similar to the typical dispersion of proper motion. Furthermore, since their typical velocity is $\sim$7 km s^{-1} and range from 0 to 10 km s^{-1}, they seem to be associated to the Taurus molecular cloud, whose radial velocity is $\sim$7 km s^{-1}. On the other hand, in the high latitude region ($|b| > 20°$), there are 70 clouds and 39 of them have measured radial velocity. The dispersion becomes $\sim$7 km s^{-1}, and velocity ranges from -10 to +12 km s^{-1}. Thus, these HLCs seem to contribute the widely distributed TTSs. Although there still remains a difference of velocity dispersions between the HLCs and TTSs, this could be explained by the limited sample of the cloud. We can roughly calculate the cloud mass as

$$M_{\rm cloud} = \pi \times A \times B \times N_{\rm H} \times m_{\rm H} \quad [{\rm g}], \tag{4.1}$$

where A and B is the cloud size in Major and Minor axes, respectively, and E_{B-V} is extinction toward the cloud. Since E_{B-V} is defined as

$$N_{\rm H} = \frac{E_{B-V}}{1.7 \times 10^{-22}} \quad [{\rm cm}^{-2}], \tag{4.2}$$

and assuming the distance to the cloud as 140 pc, the cloud mass can be derived as

$$M_{\rm cloud} \approx 0.23 \times a \times b \times E_{B-V} \quad [{\rm M}_\odot], \tag{4.3}$$

where a and b are the cloud size in the unit of arcmin. The mass of the large clouds is larger than $\sim$100 M$_\odot$, and typically $\sim$400 M$_\odot$. Thus, the cloud survey is not complete to the mass of a few M$_\odot$, which is the typical mass of the cloud core that forms a Sun-like star. From above facts, most of the widely distributed TTSs around the Taurus region were thought to be born in the small clouds, which were also distributed toward the Taurus molecular complex.

So are small clouds have large velocity dispersion? Since molecular clouds are formed from the HI clouds, we inspected the velocity dispersion of HI gas. We used HI 21 cm line data obtained by Hartmann & Burton (1997). We made the mean line profile of the HI averaged over the $2^{\rm h}40^{\rm m} <$ R.A. $< 5^{\rm h}40^{\rm m}$ and $0° <$ Dec $< 40°$ region. Figure 4.6 shows the resultant profile. The velocity dispersion is estimated to be $\sim$11.7 km s^{-1} by fitting a Gaussian function. This dispersion is consistent to that of the proper motions of the TTSs ($\sim$15 km s^{-1}). We executed chi-square test whether radial velocity distributions of previously known molecular clouds and HI clouds are same. We first estimated the expectation value of clouds in each velocity bins (1 km s^{-1} bin from -80 to $+80$ km s^{-1}) from the HI mean profile. Next, we calculated the chi-square value as

$$\chi^2 = \sum_i \frac{(N_i - n_i)^2}{n_i}, \tag{4.4}$$

where N_i is the number of clouds, n_i is expectation value in each velocity bin. Here, we used all clouds which have radial velocities, i.e., the sum of N_i or n_i over all the velocity bins is 77. We then calculated the probability as

$$P(\chi^2|\nu) = P(\frac{\nu}{2}, \frac{\chi^2}{2}), \tag{4.5}$$

where ν is the degree of freedom (in this time, 160) and P is the incomplete gamma function

$$P(a, x) = \frac{\int_0^x e^{-t}\, t^{a-1}\, dt}{\int_0^\infty e^{-t}\, t^{a-1}\, dt}, \tag{4.6}$$

and this probability becomes almost unity. Thus, the velocity distribution of known molecular clouds are different from that of HI clouds, and there would substantial amount of hidden clouds which contribute the large velocity dispersion.

4.2 Disks of Isolated TTSs

CTTS/WTTS ratios

Is there any differences of the disk properties between the TTSs associated to the clouds and isolated. First, we compare the CTTS/WTTS ratio. Since the ratio strongly depends on the sensitivity of the observations, we use TTSs detected by AKARI. There are 132 previously known TTSs (80 CTTSs and 37 CTTSs from their W(Hα)), and 23 new TTSs (14 CTTSs and 9 WTTSs). Assuming that the region of $A_V > 2$ as clouds and sources within 1° are associated to the clouds, there are 81 CTTSs and 31 WTTSs. On the other hand, for the isolated sources, we got 12 CTTSs and 16 WTTSs. Thus, the CTTS/WTTS ratios are 81/31 in the clouds and 12/16 outside the clouds. We summarized these numbers in Table 4.1.

Far-Infrared emissions from circumstellar disks

To investigate the disk properties, we use Far-Infrared data from the FIS onboard AKARI, because the dust around TTSs becomes optically thin at long wavelengths, and then, is sensitive to dust mass. As noted in §3.1, 79 previously known TTSs (53 CTTSs and 16 WTTSs) were detected by the FIS. Of the 23 new TTSs, only 3 CTTSs were detected. We got 52 CTTSs and 14 WTTSs, which were associated to clouds, and 4 CTTSs and 2 WTTSs, which were isolated (see Table 4.1). The FIS detection rates for sources inside clouds are 41% and 12% for CTTSs and WTTSs, respectively, and for isolated sources are 25% and 1% for CTTSs and WTTSs, respectively. The detection rate for isolated WTTSs is one tenth of the cloud associated WTTSs. The similar results are shown

Table 4.1: TTS

		initial	IRC detection			FIS detection		
		known	known	new	total	known	new	total
CTTS	cloud	122	76	6	82	50	2	52
	isolate	8	4	9	13	3	1	4
WTTS	cloud	112	28	2	30	14	0	14
	isolate	157	9	6	15	2	0	2
other	cloud	111	15	—	15	10	—	10
	isolate	6	0	—	0	0	—	0
total		516	132	23	155	79	3	82

by Cieza et al. (2007) that disks frequencies of WTTSs, which are associated molecular clouds, are 3–6 times larger than that for a relatively isolated WTTSs. Although the initial number of isolated CTTSs is small (8 previously known and 8 newly found), the detection rate for isolated CTTSs is also smaller than those associated to clouds. The decrease of detection rate indicate that isolated TTSs would relatively older than those associated to clouds, due to disk dissipation.

We can estimate the mass of the circumstellar disk from the 90 μm flux density by following equation

$$M_{\rm disk} = F_\nu \times \left(\frac{d^2}{B_\nu(T_{\rm dust})\kappa_\nu} \right), \tag{4.7}$$

where F_ν is flux density, d is distance to the target TTS, $B_\nu(T)$ is the Planck function at the temperature of T, and κ_ν is the absorption coefficient. Assuming a dust temperature of $T_{\rm dust} = 50$ K (typical temperature for primordial disks), absorption coefficient of $\kappa_{90\mu{\rm m}} = 0.67$ (astronomical silicate, e.g., Weingartner & Draine 2001), and the distance of $d = 140$ pc, the disk mass can be estimated as

$$M_{\rm disk} = 20 \times \frac{F_\nu}{1[{\rm Jy}]} \quad [{\rm M}_\oplus]. \tag{4.8}$$

We note that since the κ_ν comes from the astronomical silicate, the derived mass is total (gas + dust) one. The detection limit of 0.5 Jy at 90 μm, which is the most sensitive FIS band, corresponds to the disk gas mass of $\sim$10 M$_\oplus$. Figure 4.7 shows the histogram of the flux densities at 90 μm band. Typical disk masses of TTSs associated to clouds and isolated ones are both $\sim$20 M$_\oplus$ (disk mass). Although number of isolated TTSs is small, it is not unreasonable to say that the distribution of disk mass is similar to that of TTSs inside clouds. Assuming that the isolated TTSs are relatively old, the disk mass becomes smaller because of disk dissipation with time.

Spectral energy distributions

The spectral energy distribution (SED) well represents the shape of TTS disk. We, classified TTSs detected by the IRC (known + new) with their slopes ($\alpha = \mathrm{d}\log\lambda F_\lambda/\mathrm{d}\log\lambda$) of the SED at wavelengths of 1–24 μm. The classification was done with following criteria.

1. 'embedded' ($\alpha_{J-K_S} > 0$ and $\alpha_{K_S-9} > -0.4$): these sources have very red colours owing to extinction, i.e., they are thought to be obscured by surrounding envelope.

2. 'nir-excess' (remaining sources of the other criteria): they have moderate excess emission at $\gtrsim 2\mu$m wavelengths. This SED seems to indicate a primordial, optically thick disk.

3. 'mir-excess' ($\alpha_{K_S-9} < -0.8$ and $\alpha_{K_S-9} < \alpha_{9-24<0}$): they have weak or no excess emission at $\lesssim 5-8\mu$m, but have optically thin excess emission at longer wavelengths. This SED is thought to indicate 'homologously depleted disk' which is the other type of transitional disk, newly suggested by Currie et al. (2009).

4. 'mir-turnover' ($\alpha_{K_S-9} < -0.8$ and $\alpha_{9-24} > 0$): they have blackbody-like SED at $\lesssim 9\mu$m, but strong, optically thick excess emission at longer wavelengths. This SED corresponds to the 'classical' transitional disk (i.e., a disk with inner hole).

5. 'photosphere' ($\alpha_{2.2-24} < -2$): they seem to have no excess emission. However, we cannot rule out whether they have teneous debris disks.

For the 127 TTSs associated to clouds, there are 33 'embedded', 40 'nir-excess', 36 'mir-excess', 9 'mir-turnover', and 9 'photosphere' sources. Furthermore, for the 27 isolated TTSs, there are 2 'embedded', 10 'nir-excess', 6 'mir-excess', 1 'mir-turnover', and 8 'photosphere' sources (see Table 4.2). The SEDs are shown in Figures 4.9–4.18.

We hardly find clear correlations between the SED types and their spatial distributions (see Figure 4.8). There are 2 'embedded' sources of isolated TTSs; one is a previously known CTTS, L1489 IRS, and the other is a new CTTS. The new CTTS, AKARI-IRC-V1 J0525519+345228, has Hα emission with P-Cygni profile. It locates $\sim 30'$ north west of an HII region, IC 417. Thus, these 2 CTTSs are thought to be locally embedded.

Although the fractions of each disk-bearing objects ('nir-excess', 'mir-excess', and 'mir-turnover' classes) are almost the same between TTSs associated to the clouds and isolated TTSs, the fractions of foregoing 'embedded' and following 'photosphere' objects are different. About a quarter of TTSs associate to the clouds have envelopes and a few % of them are naked. On the other hand, a

Table 4.2: Numbers of SED types

cloud	SED types	isolate
33 (26%)	'embedded'	2 (7%)
40 (31%)	'nir-excess'	10 (37%)
36 (28%)	'mir-excess'	6 (22%)
9 (7%)	'mir-turnover'	1 (4%)
9 (7%)	'photosphere'	8 (30%)

few % of isolated TTSs have envelopes and one third of them are naked. This indicates that sources outside the clouds are relatively older. We note that this classification is erratic for sources which do not have photometric data at ∼3–8 μm wavelengths (i.e., about a half of the cloud TTSs and almost all isolated TTSs).

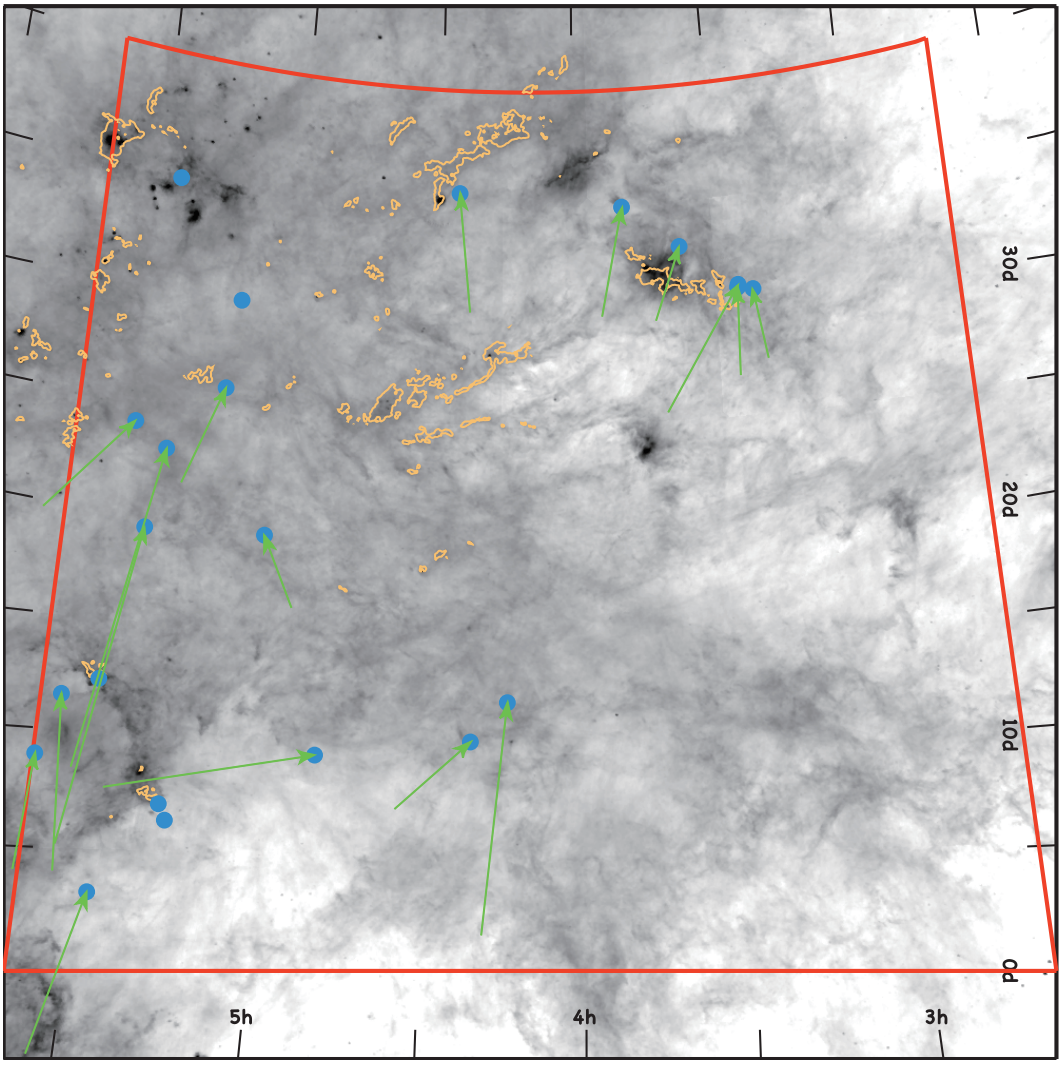

Figure 4.1: Distribution (circles) and proper motions (vectors) of the new TTSs. The mean proper motions of the Taurus molecular clouds of (6, -22) mas yr^{-1} (Jones & Herbig 1979) were subtracted. The vectors represents the movements of the sources for the ideal last 1 Myr. The grey scale and yellow contour are the same as Figure 2.5.

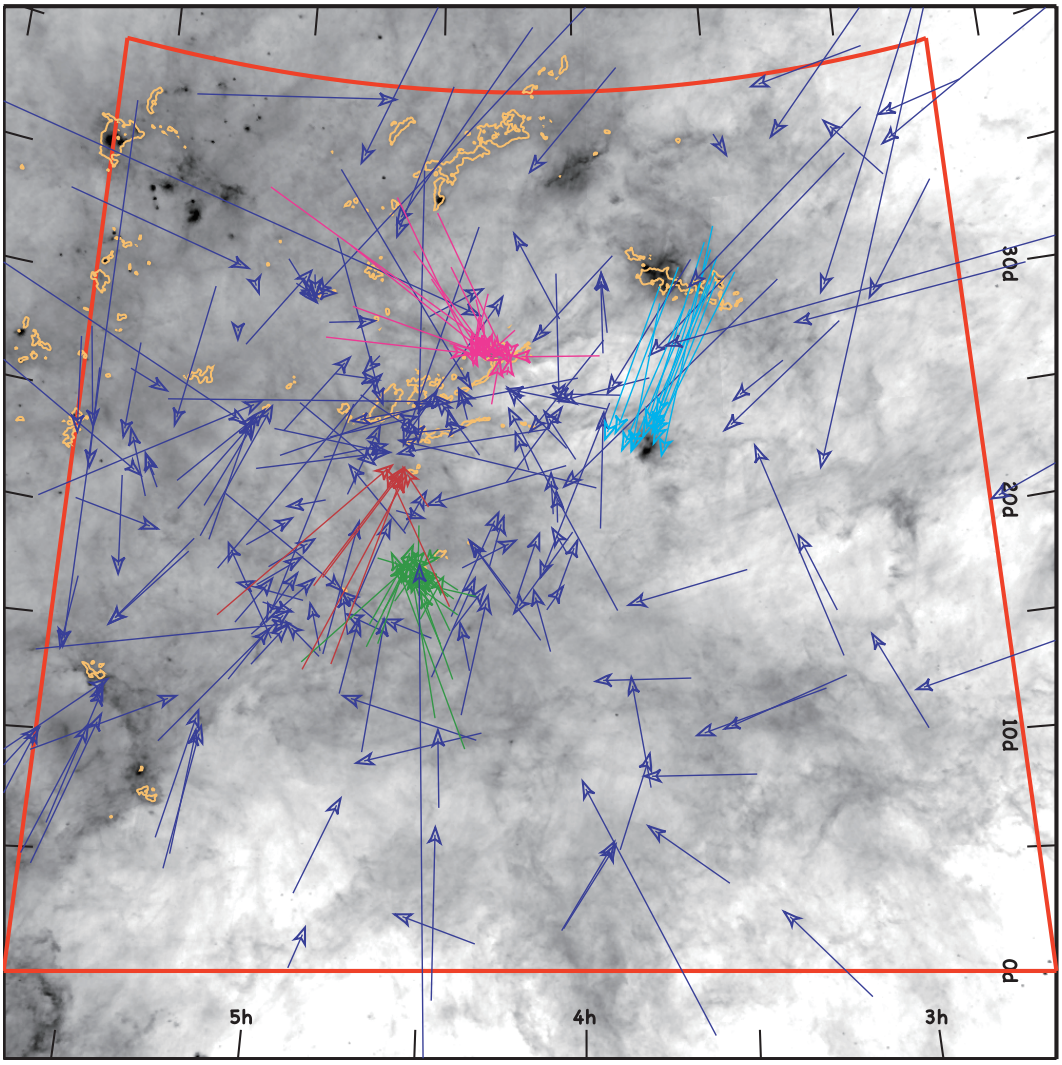

Figure 4.2: The proper motions of the previously known TTSs. The mean proper motions of the Taurus molecular clouds of (6, -22) mas yr^{-1} (Jones & Herbig 1979) were subtracted. The cyan, green magenta, and red vectors indicate the probable members of the Pleiades, L1551, L1495, and L1536, respectively. The vectors represents the movements of the sources for the ideal last 1 Myr. The grey scale and yellow contour are the same as Figure 2.5.

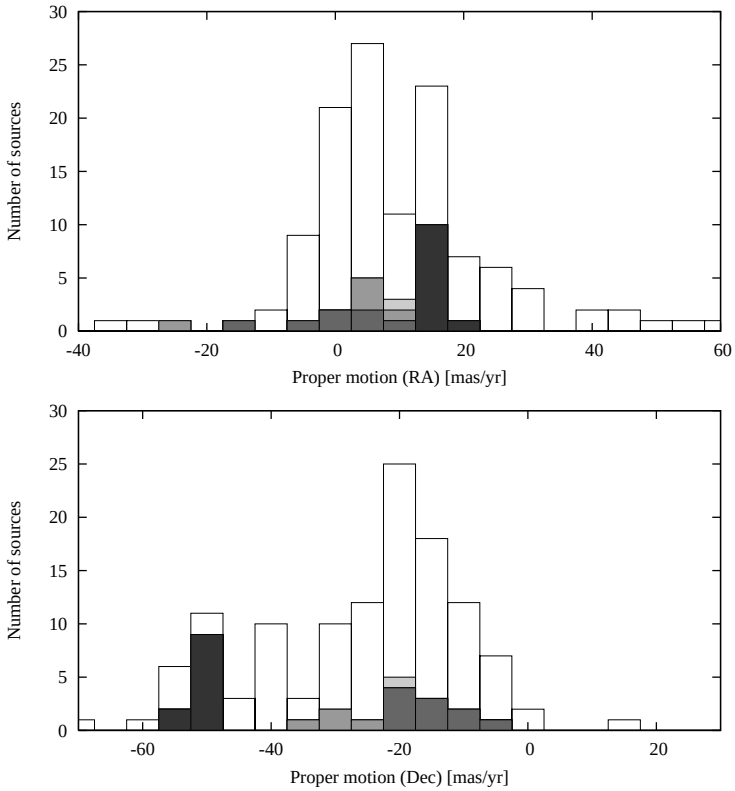

Figure 4.3: The histograms of the proper motions in R.A. (*top*) and Dec. (*bottom*) direction. The black, dark grey, grey, and light grey bins are for the Pleinades, L1551, L1495, and L1536 members, respectively. The white bins are for the other Taurus members. The bin sizes are 10 mas yr^{-1}.

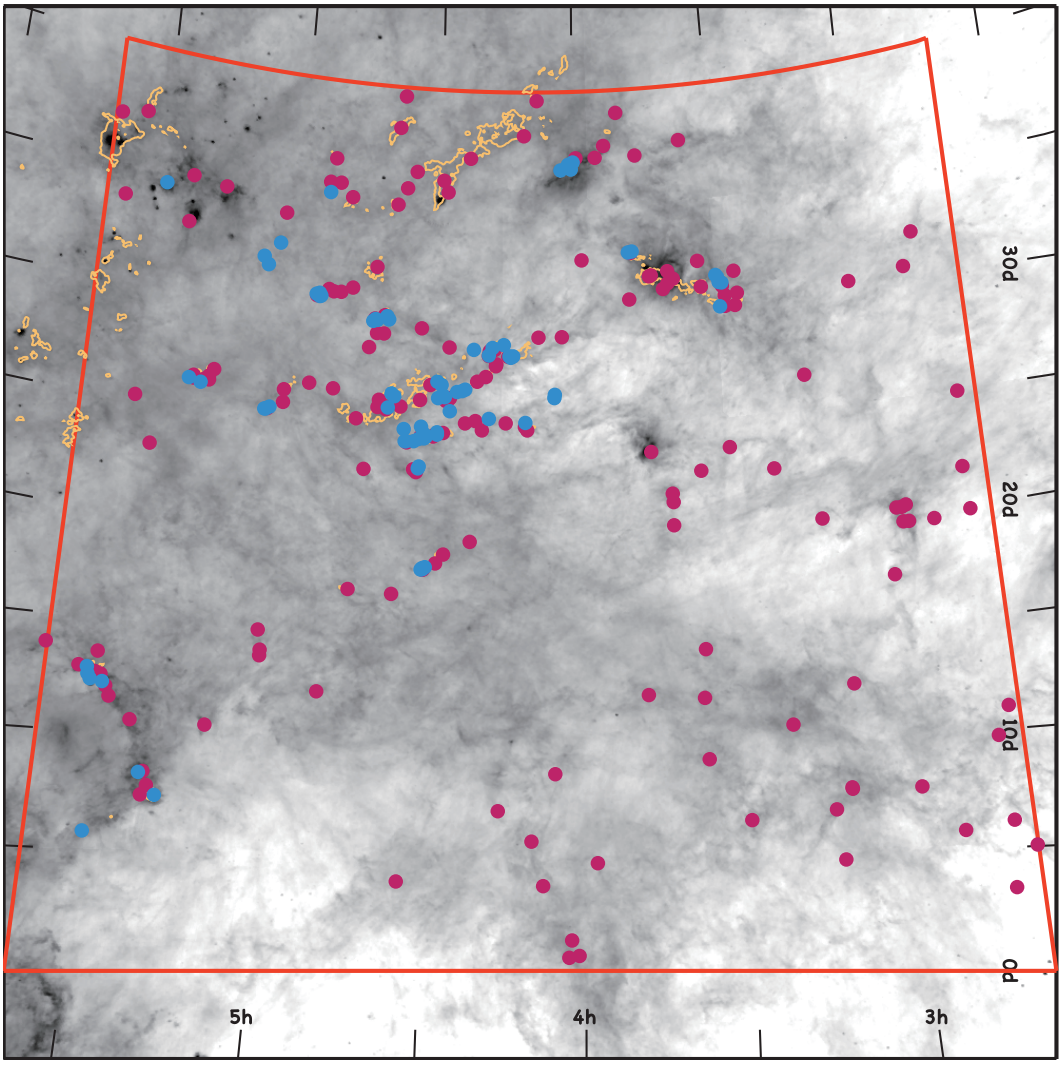

Figure 4.4: The spatial distributions of clouds, catalogued by Dutra & Bica (2002). The magenta circles are clouds with size of $> 10'$ and the cyan ones are $< 10'$ clouds. The grey scale and the yellow contour are same as Figure 2.5.

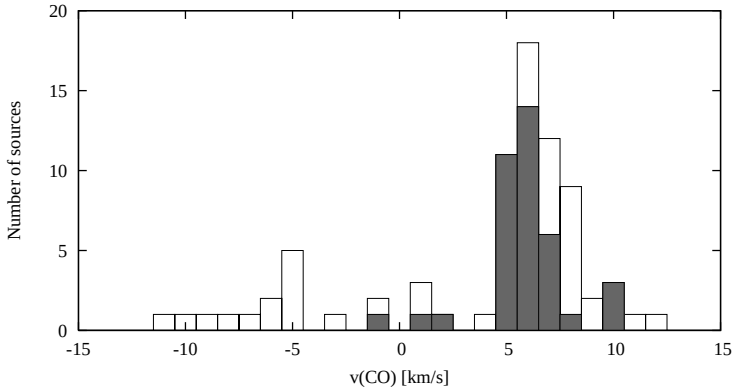

Figure 4.5: The histogram of the radial velocities of previously known clouds measured by CO line emission. The black bins are for the clouds in the low latitude region ($|b| < 20°$). The bin size is 1 km s^{-1}.

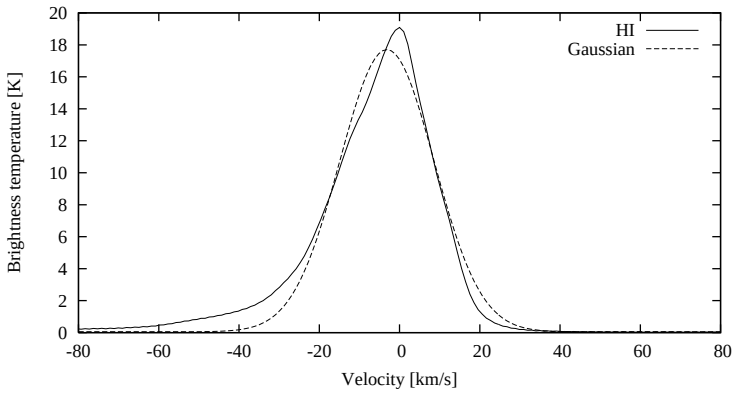

Figure 4.6: The mean profile of the HI 21 cm line toward the Tau-Aur region. The broken curve shows the fitted Gaussian ($\sigma \sim 11.7$ km s^{-1}).

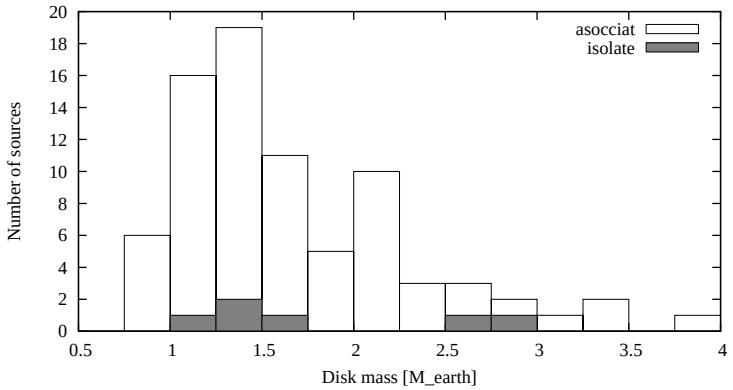

Figure 4.7: The histogram of disk mass, derived from the AKARI 90 μm band. The open and filled boxes are the TTSs associated to the clouds and isolates, respectively. The bin size is 0.25 $M_{\oplus}$.

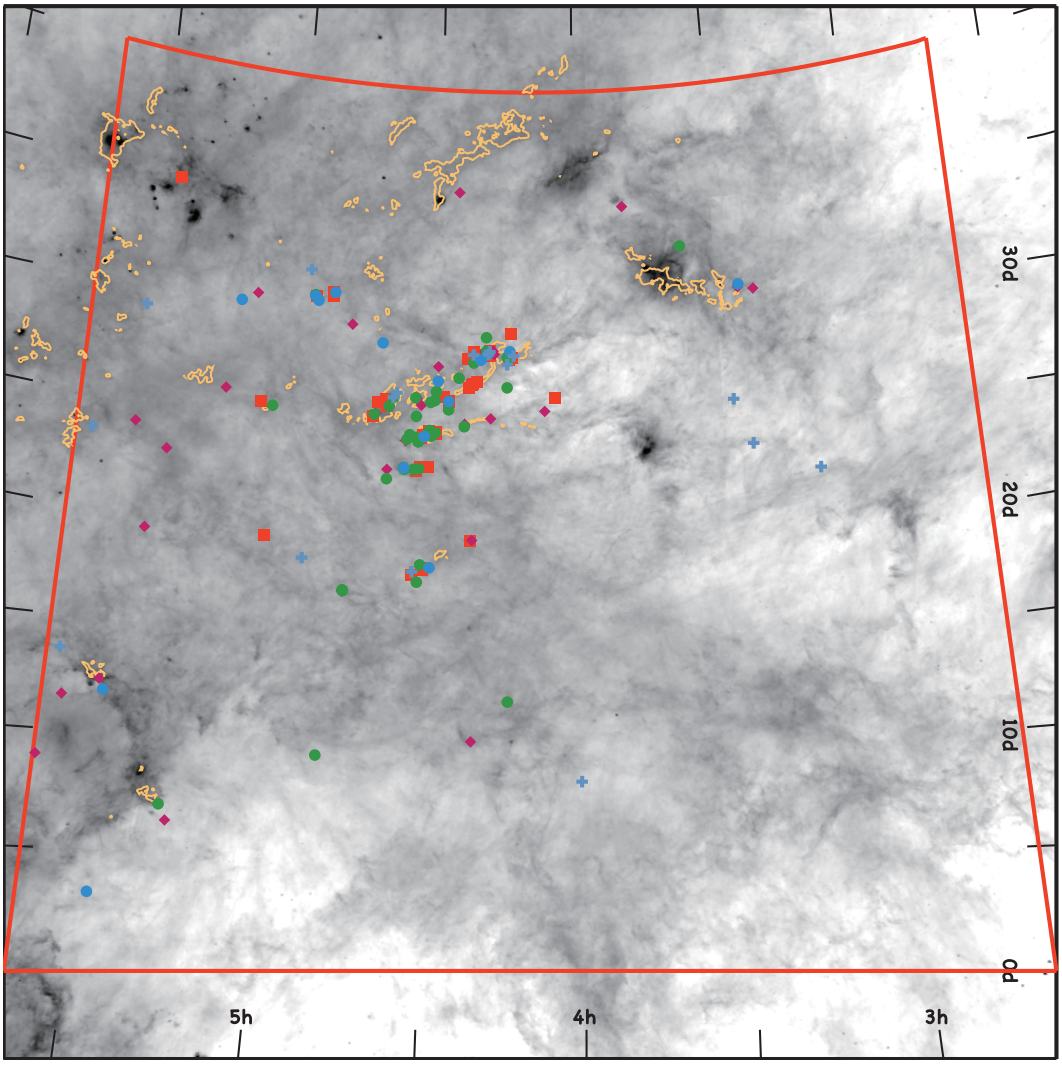

Figure 4.8: The spatial distributions of the AKARI detected previously known TTSs. The red squares are 'embedded', magenta diamonds are 'nir-excess', green diamonds are 'mir-excess', green circles are 'mir-turnover', and cyan pluses are 'photosphere'. The grey scale and the yellow contour are same as Figure 2.5.

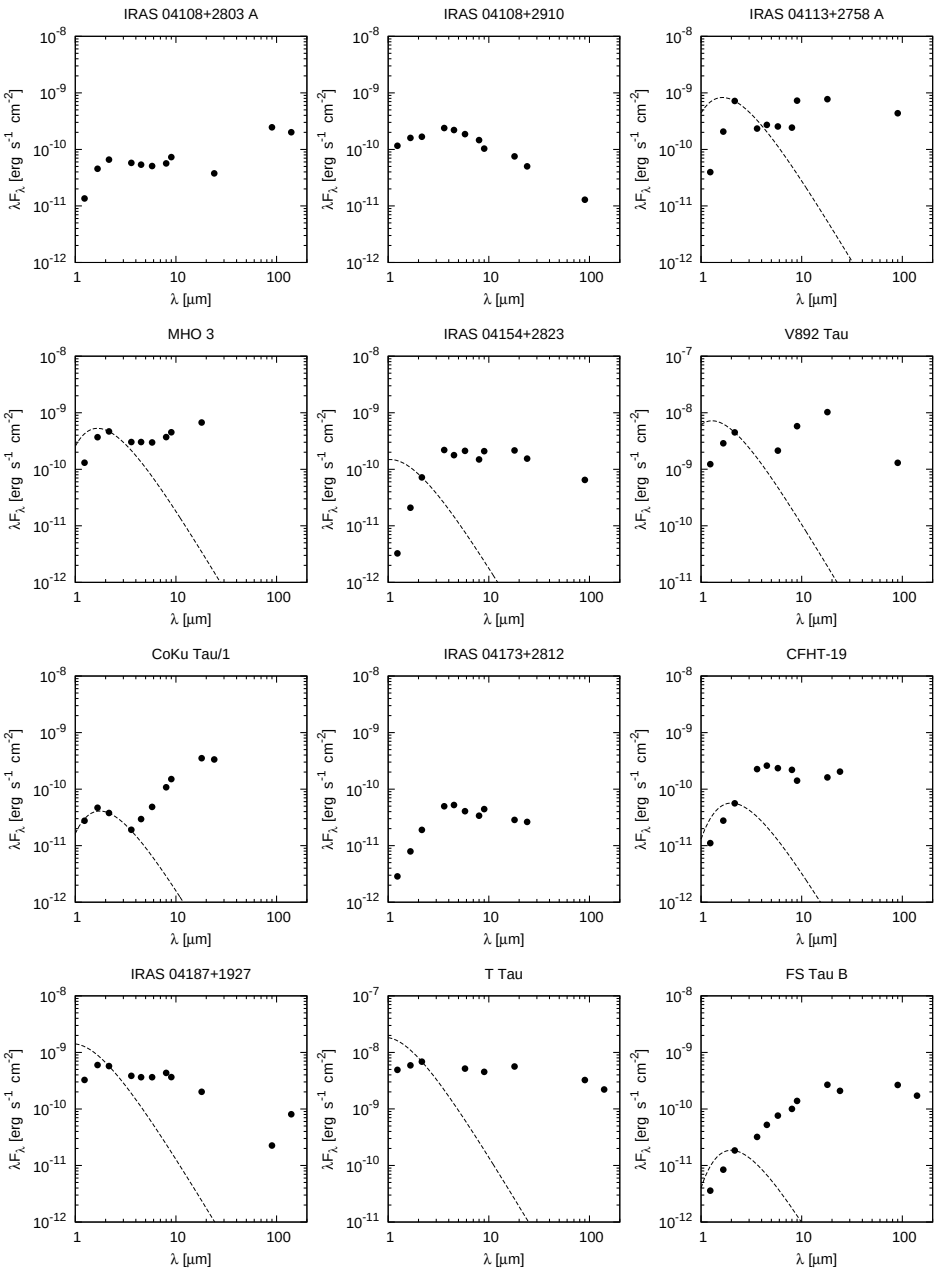

Figure 4.9: SEDs of the TTSs, associated to clouds and classified as 'embedded'. The broken curve represents the Planck function normalized to the K_S band flux, if the sources have been measured effective temperature in previous studies.

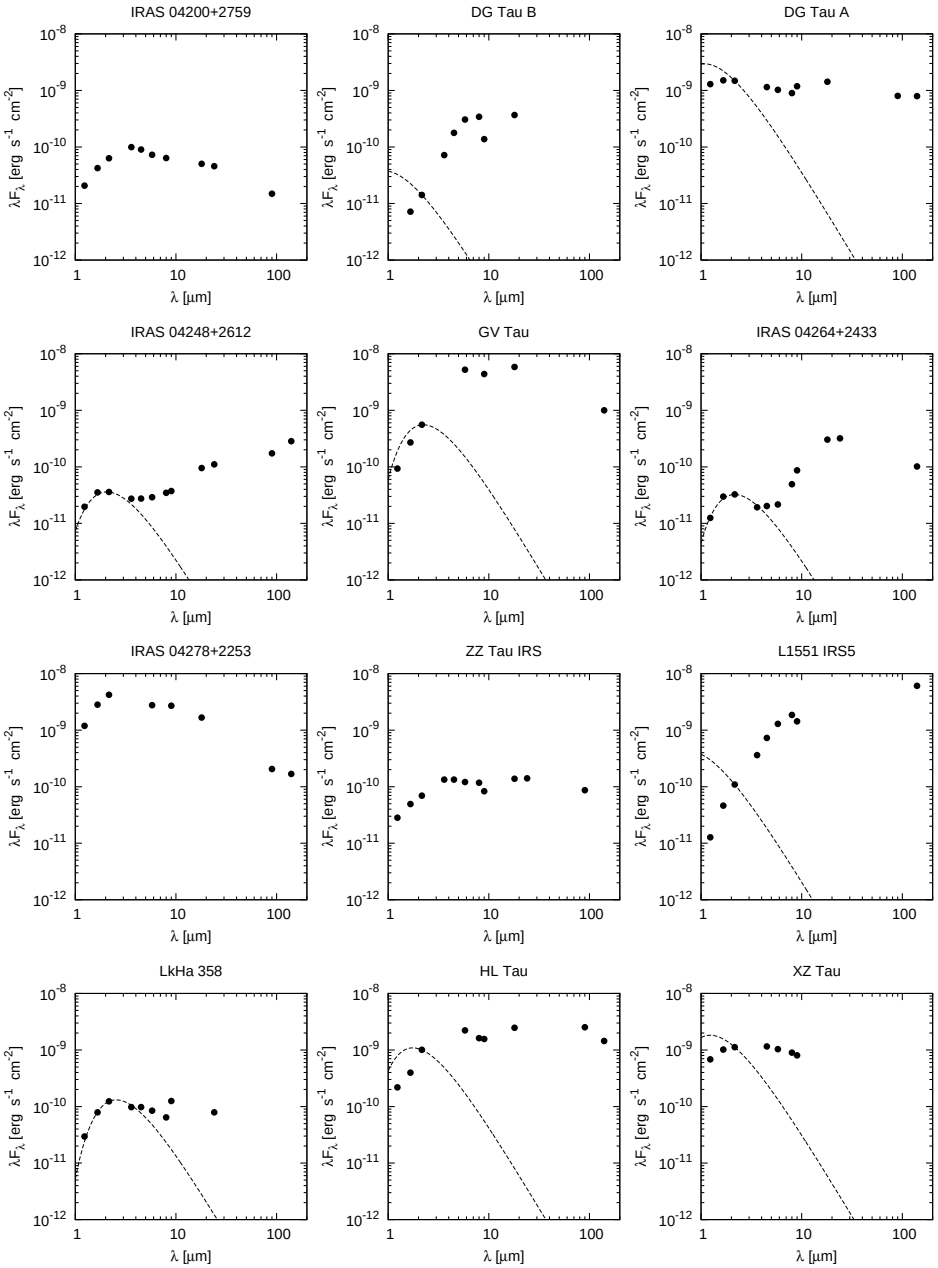

Figure 4.9: *Continued.*

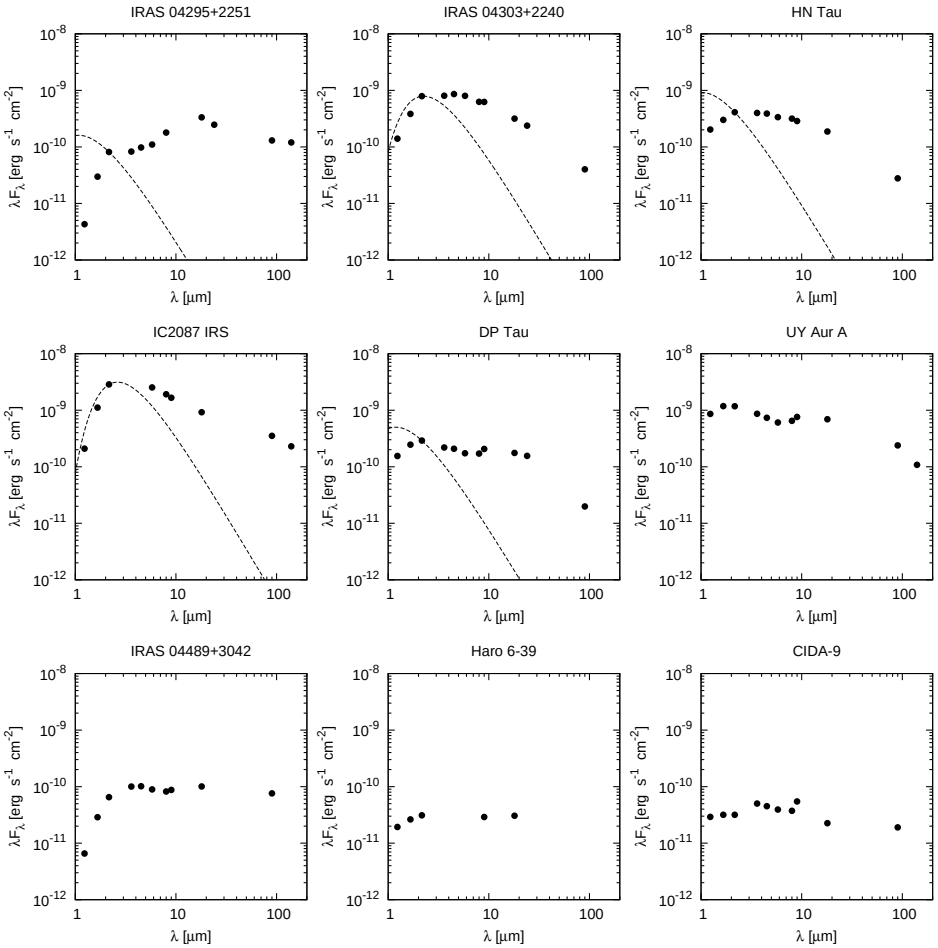

Figure 4.9: *Continued.*

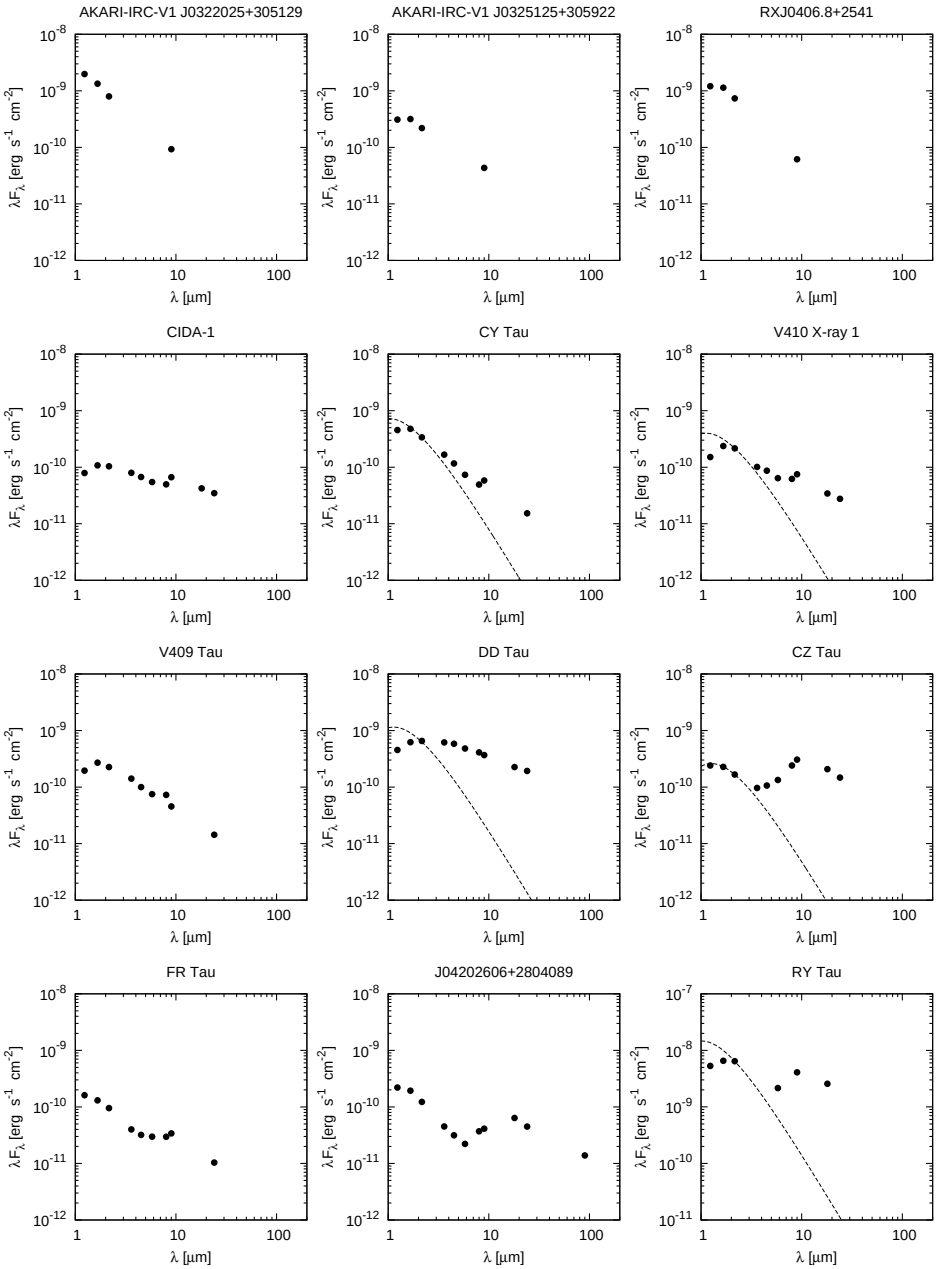

Figure 4.10: SEDs of the TTSs, associated to clouds and classified as 'nir-excess'. The broken curves are the same as Figure 4.9.

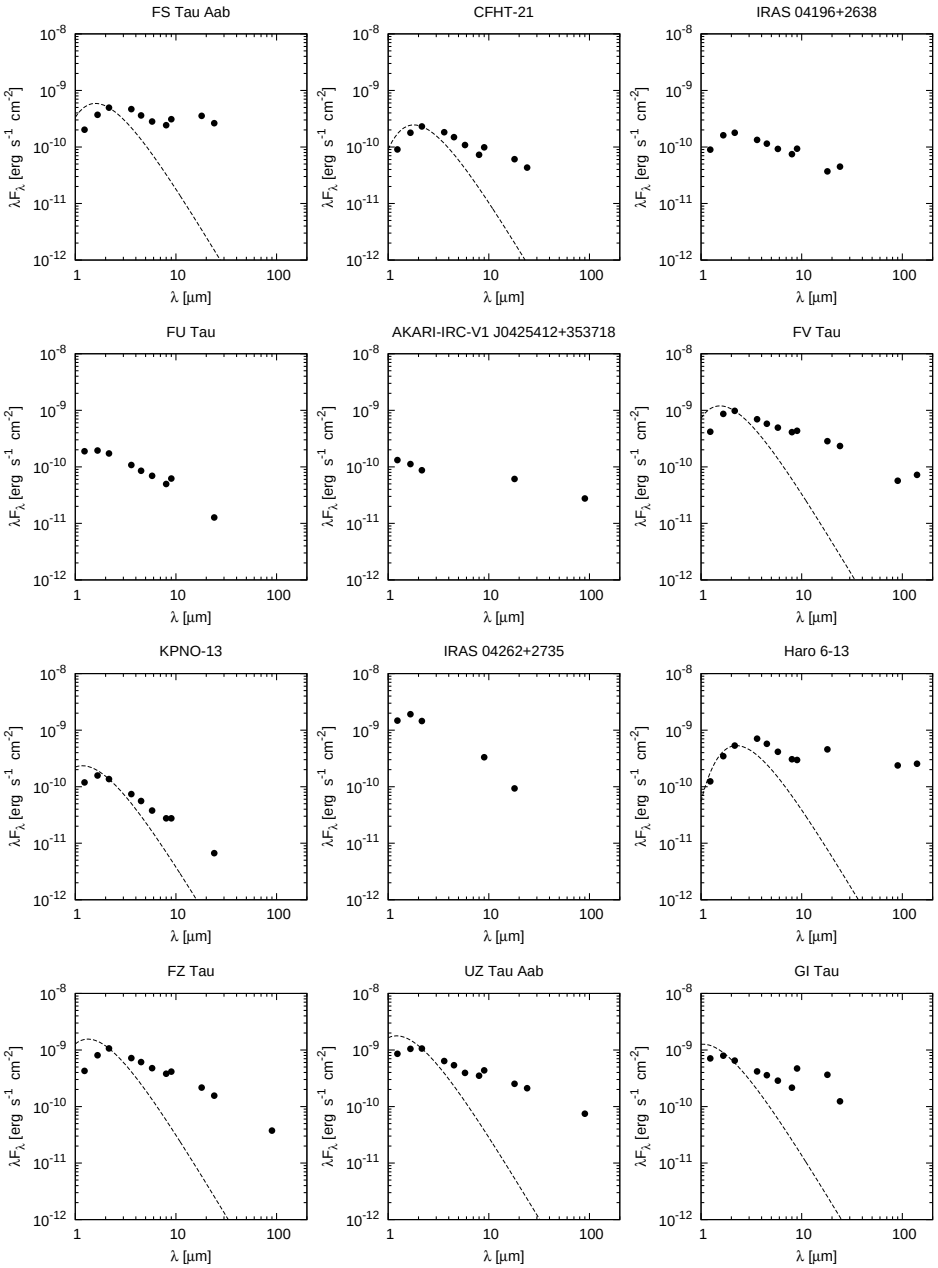

Figure 4.10: *Continued.*

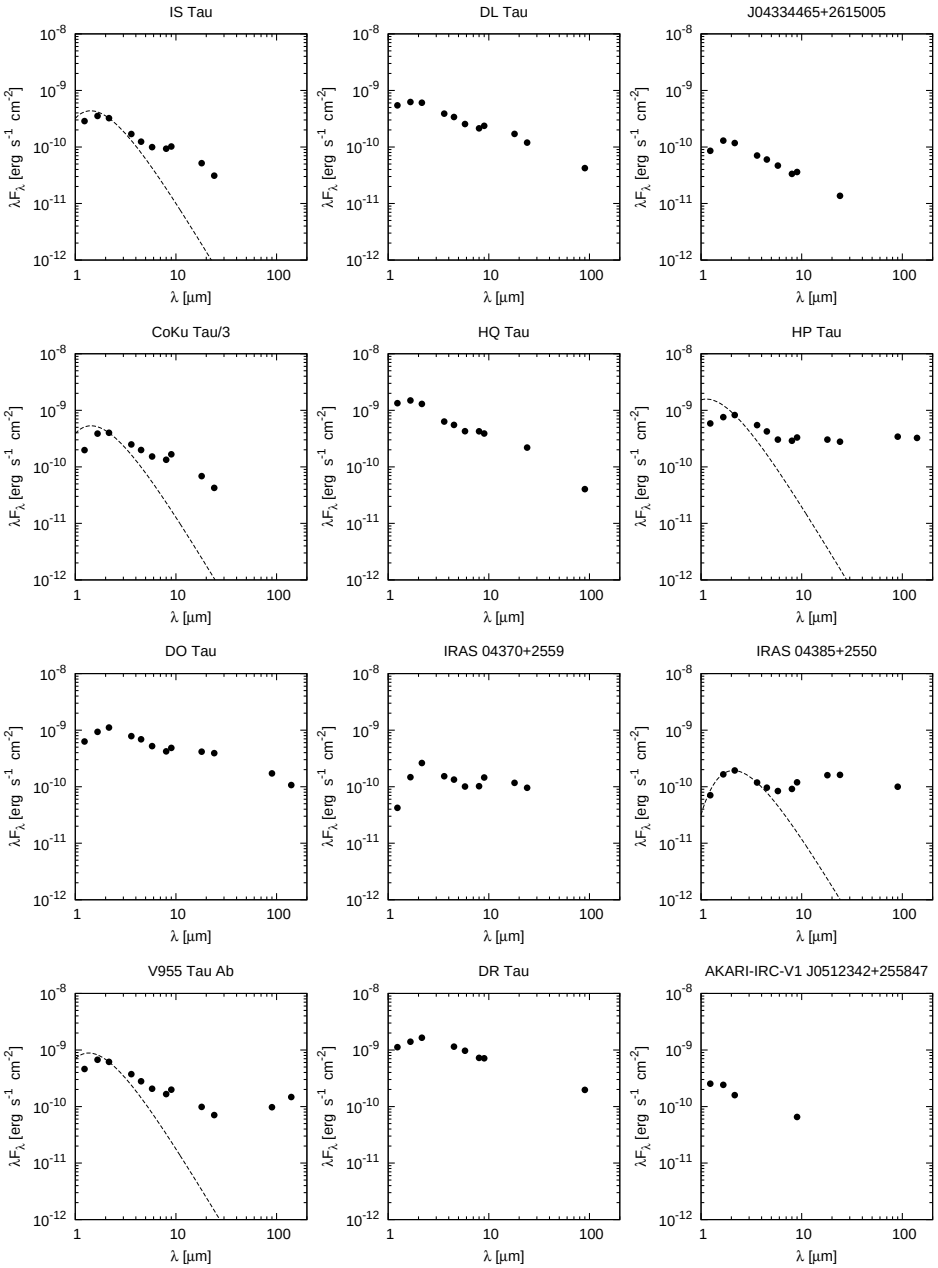

Figure 4.10: *Continued.*

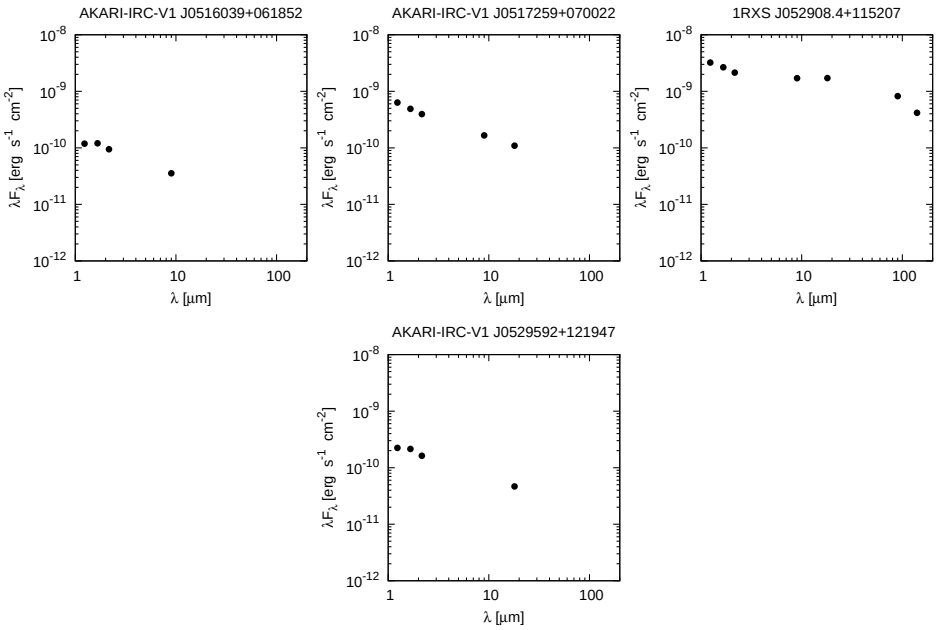

Figure 4.10: *Continued.*

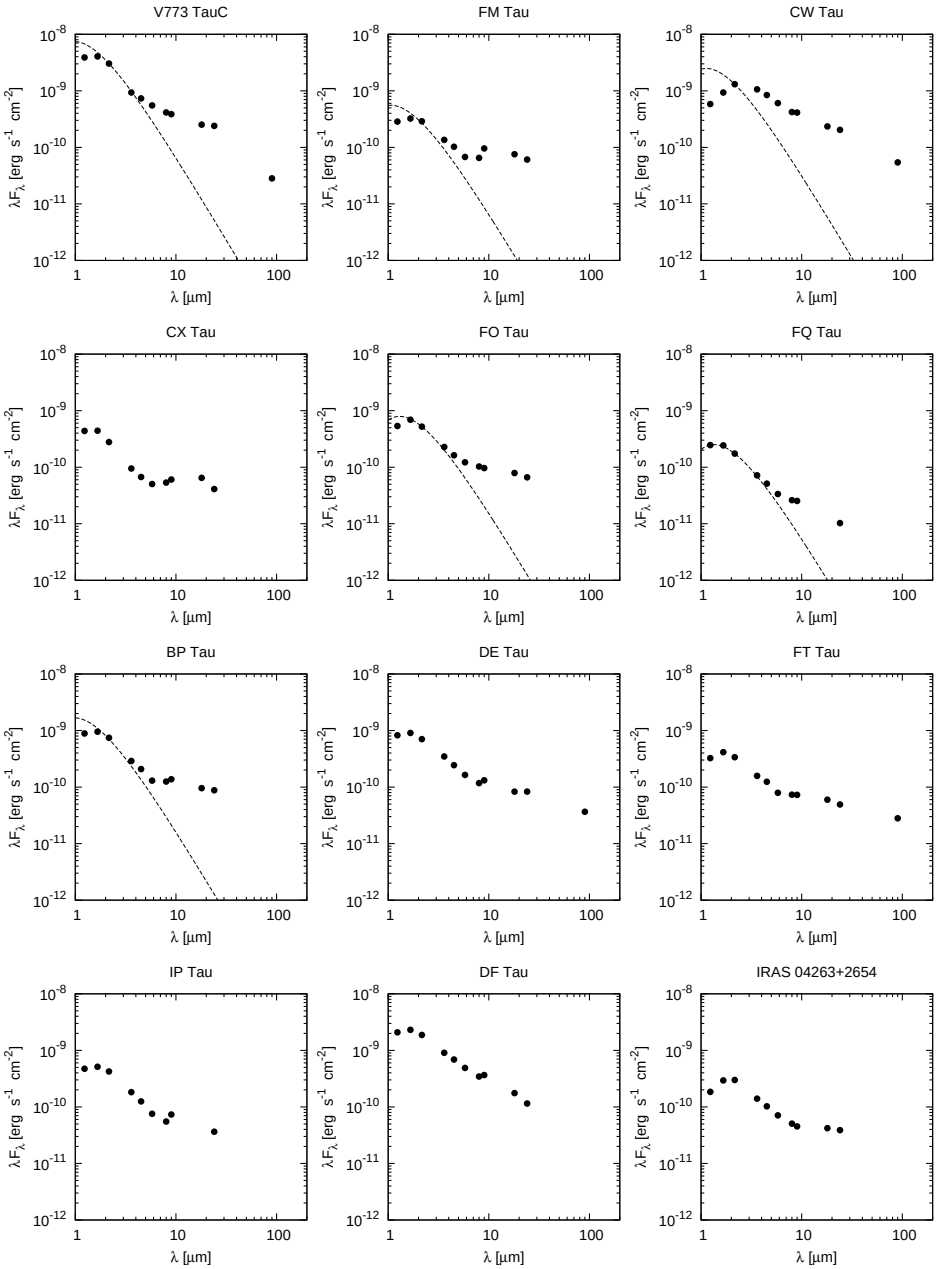

Figure 4.11: SEDs of the TTSs, associated to clouds and classified as 'mir-excess'. The broken curves are the same as Figure 4.9.

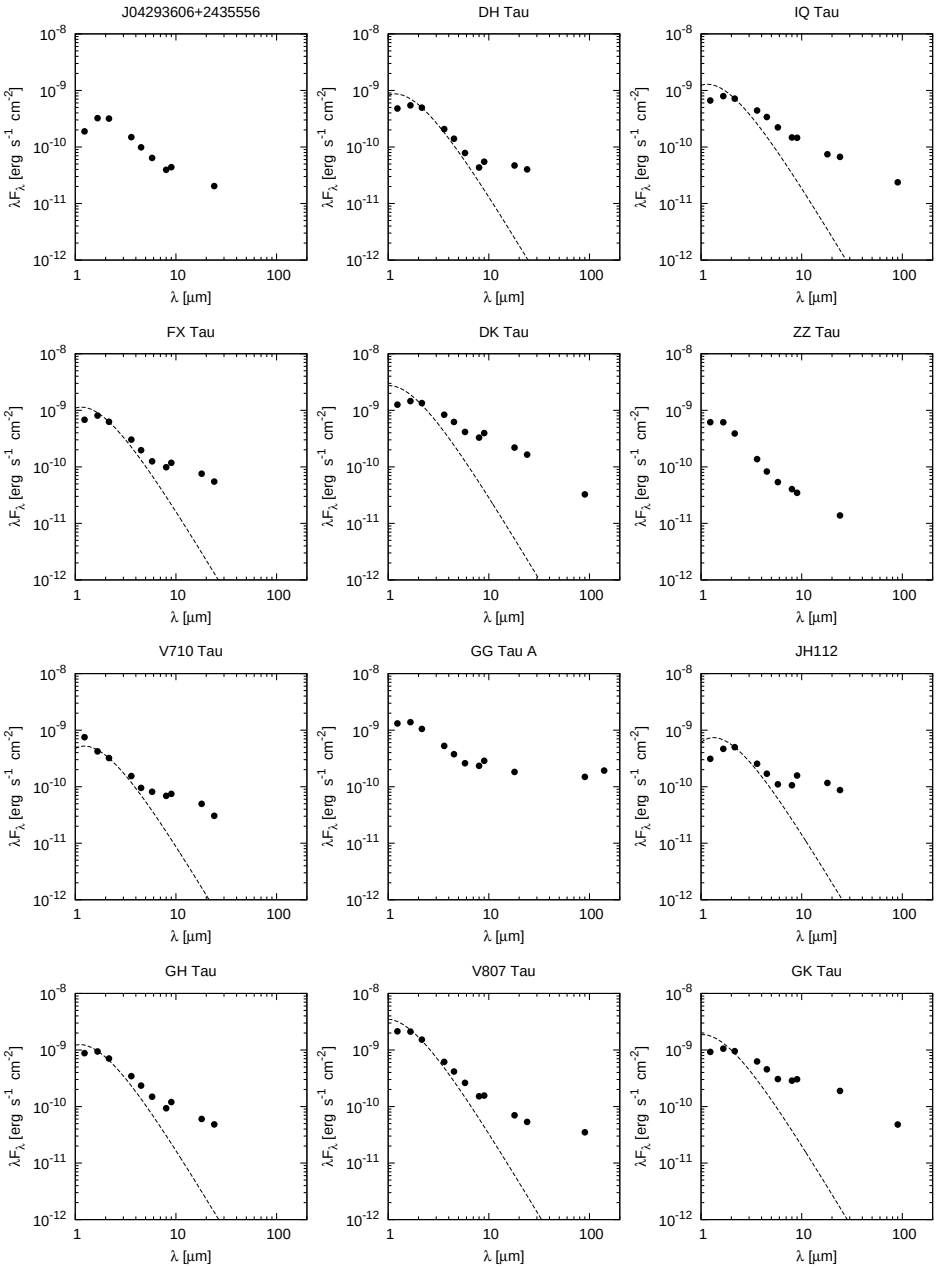

Figure 4.11: *Continued.*

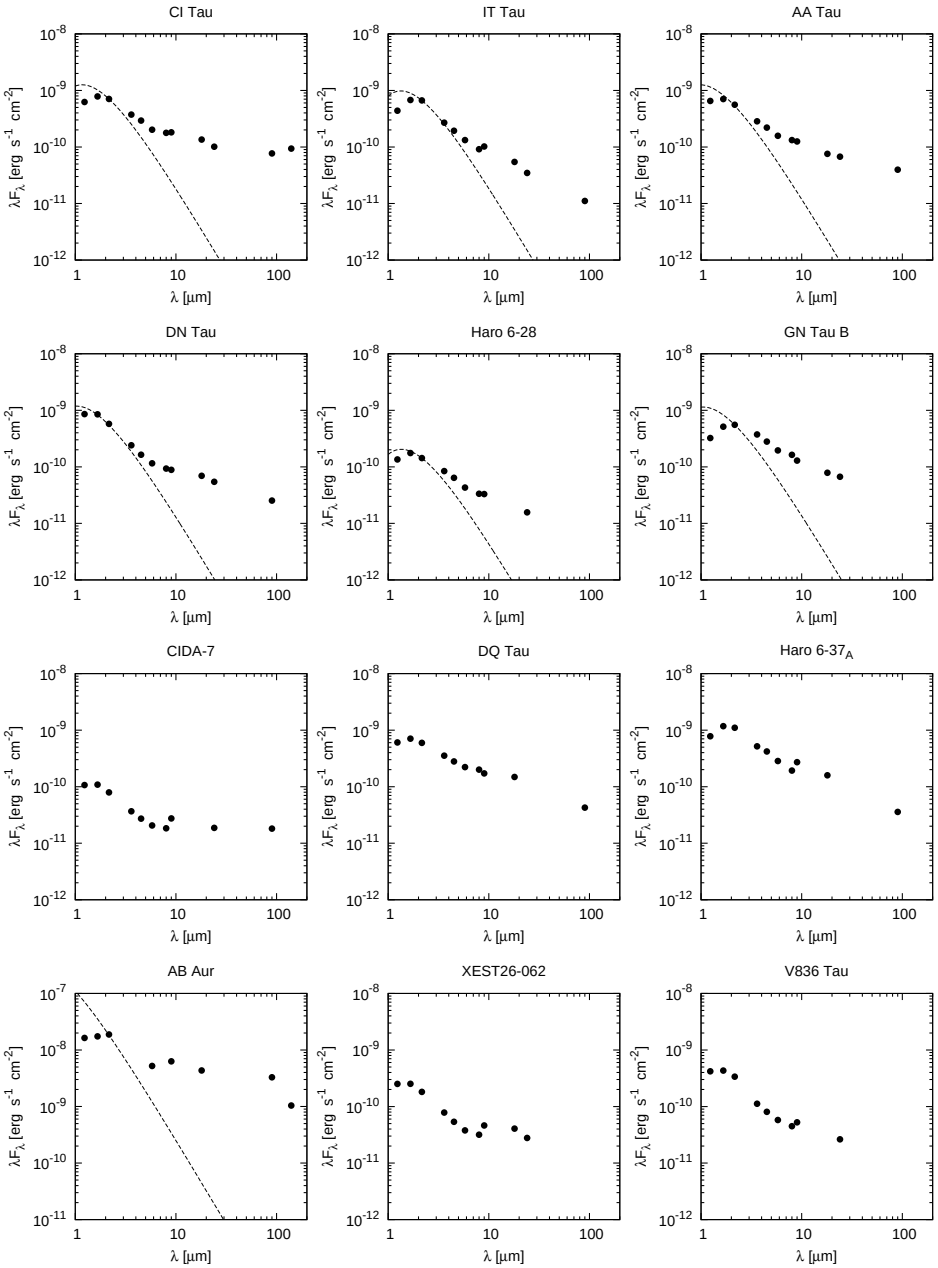

Figure 4.11: *Continued.*

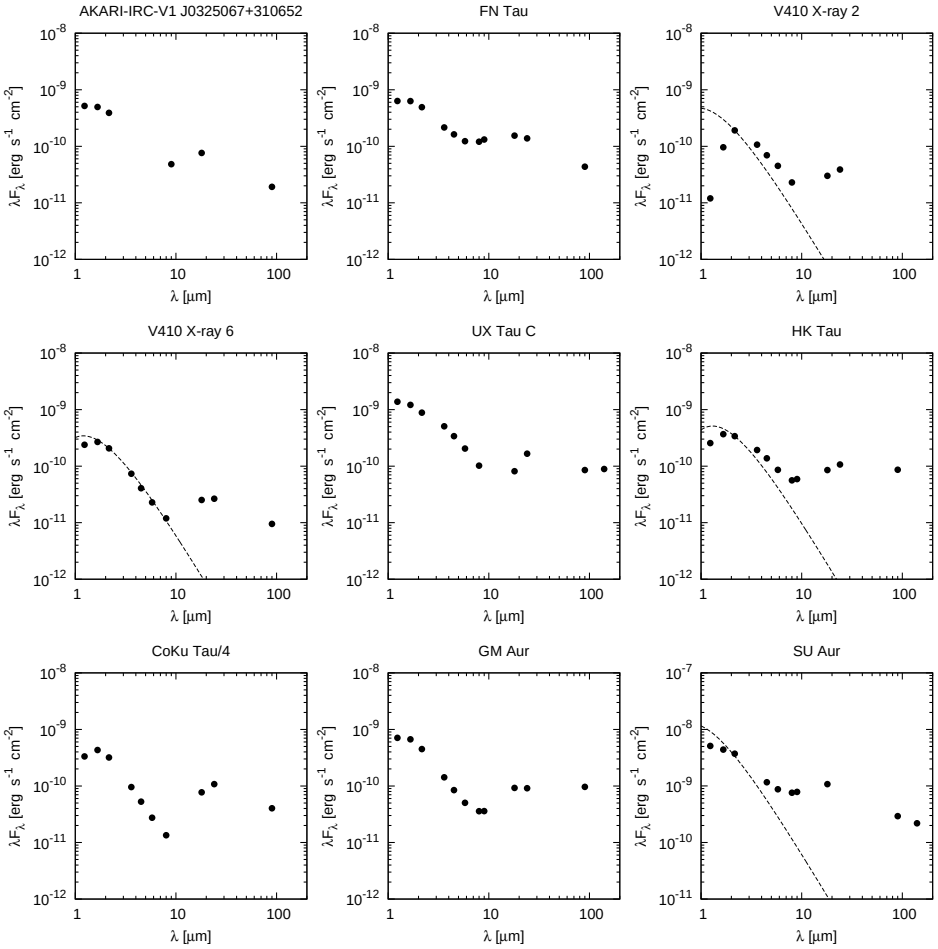

Figure 4.12: SEDs of the TTSs, associated to clouds and classified as 'mir-turnover'. The broken curves are the same as Figure 4.9.

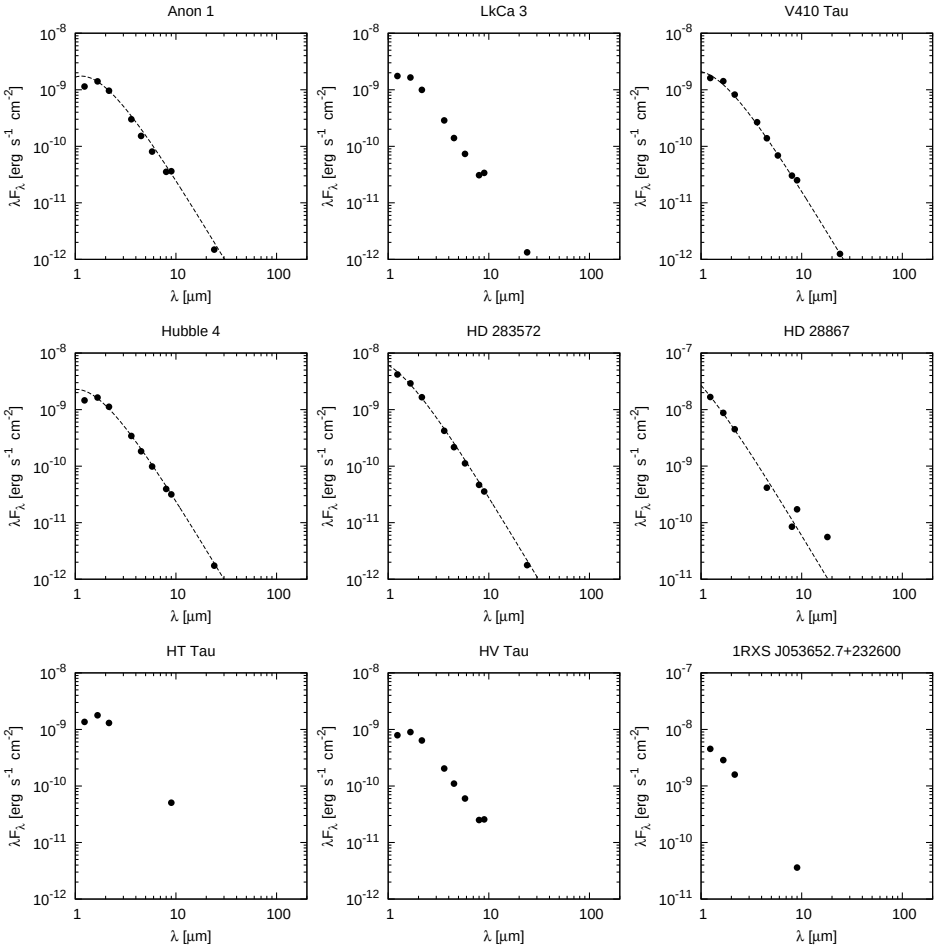

Figure 4.13: SEDs of the TTSs, associated to clouds and classified as 'photosphere'. The broken curves are the same as Figure 4.9.

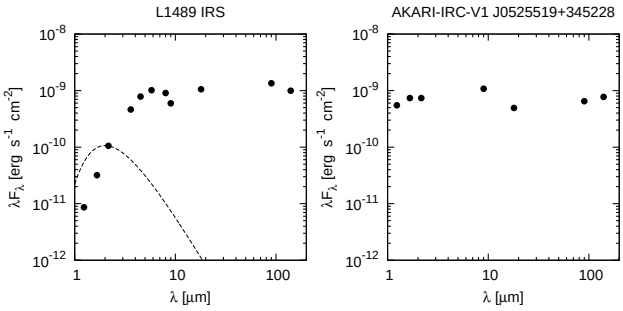

Figure 4.14: SEDs of the isolated TTSs, classified as 'embedded'. The broken curves are the same as Figure 4.9.

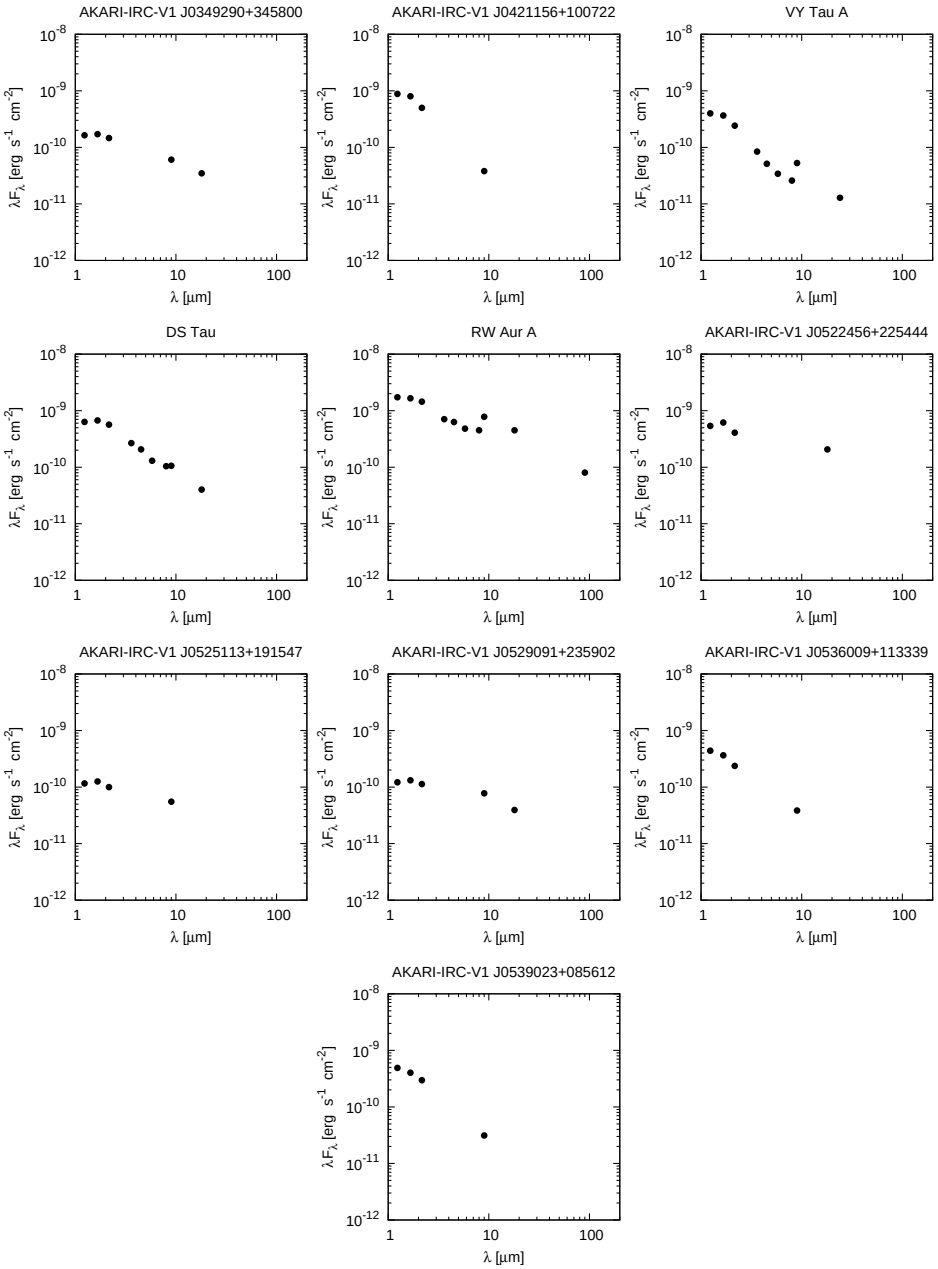

Figure 4.15: SEDs of the isolated TTSs, classified as 'nir-excess'. The broken curves are the same as Figure 4.9.

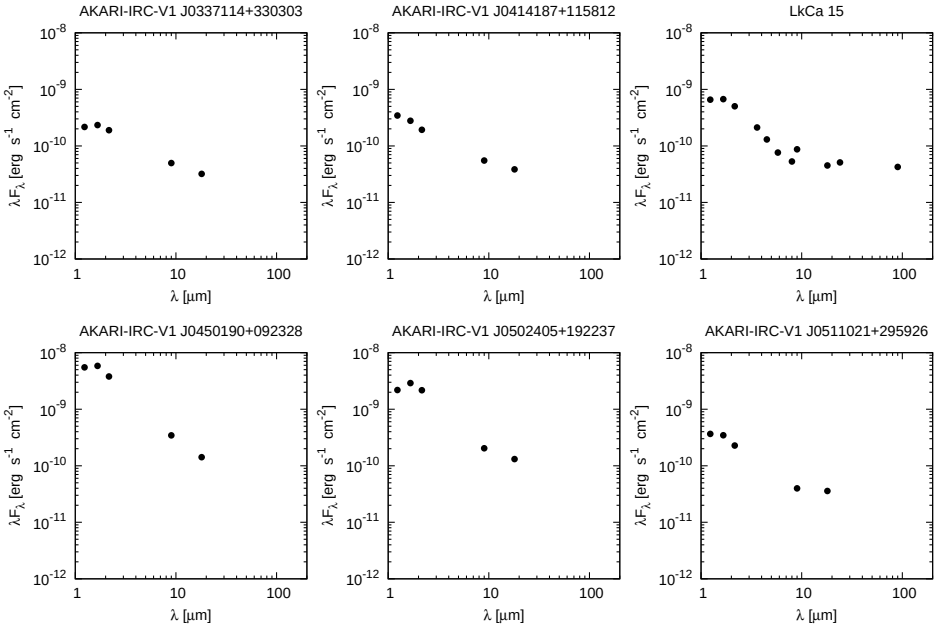

Figure 4.16: SEDs of the isolated TTSs, classified as 'mir-excess'. The broken curves are the same as Figure 4.9.

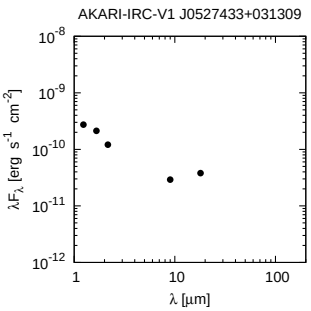

Figure 4.17: SEDs of the isolated TTSs, classified as 'mir-turnover'. The broken curves are the same as Figure 4.9.

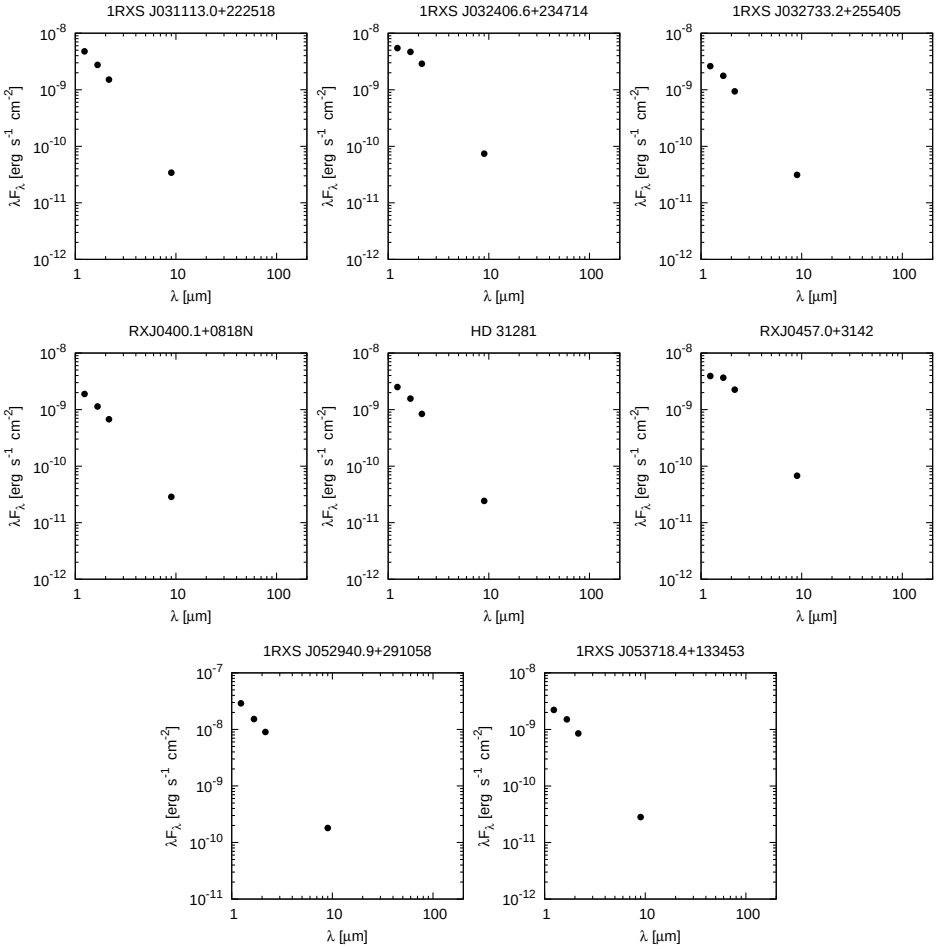

Figure 4.18: SEDs of the isolated TTSs, classified as 'photosphere'. The broken curves are the same as Figure 4.9.

Chapter 5

SUMMARY

In this thesis, we proposed new criterion to extract TTSs by using AKARI (MIR) as well as UCAC (optical) and 2MASS (NIR) surveys. Our new criterion is valid for the whole sky, i.e., not biased to the molecular clouds. We further investigated the origin and disk properties of TTSs isolated from molecular clouds.

We performed a survey of TTSs toward a 1800-square-degree region of Taurus-Auriga star forming region, based on the AKARI IRC All-Sky Survey. To determine the TTS selection method, we used 132 out of 516 previously known TTSs, that were detected by the AKARI IRC. Since TTSs show IR excess emission from dust in the protoplanetary disks, we used colour-colour and colour-magnitude diagrams to extract TTSs. In this process, we also consider other types of objects with surrounding dust, which also show IR excess emission, to avoid contamination. Using the $(J - K_S)$ vs. $(S9W - L18W)$, $(UCAC)$ vs. $(UCAC - J)$, $(J - K_S)$ vs. $(K_S - S9W)$ and $(J - K_S)$ vs. $(K_S - L18W)$ diagrams, we can extract TTS candidates with $\sim$ 80% probability. Although a number of high sensitivity surveys of TTSs have been done by Spitzer, our method has a strong advantage in the survey area, i.e., the whole sky.

From this method, we got 26 new TTS candidates. We performed follow-up spectroscopic observations at optical wavelengths, and found that 23 sources are TTSs. This result indicates the usefulness of our method.

Of the 23 new TTSs, 15 sources locate outside the clouds. Furthermore, there are 171 previously known TTSs, isolated from the clouds. There are three ideas for the origin of isolated TTSs;

1. TTSs have moved with their proper motions of $\Delta v \sim$1 km s^{-1}, taking over the thermal velocity dispersions of the natal cloud gas,

2. TTSs were born in cloudlets, and the cloudlets have already dissipated,

3. TTSs were dynamically ejected with high-velocity by gravitational interactions with other stars,

but the third idea contributes to few TTSs.

To determine the origin of isolated TTSs, we checked proper motions of the previously known TTSs using UCAC. We confirmed some spatial-kinematical groups, and the dispersions of proper motion are $\sim$1 and $\sim$4–5 km s^{-1} for the Pleiades and L1551 groups, respectively. The dispersions of proper motion of the remaining sources are as large as $\sim$15 km s^{-1}, far exceeds the typical value of $\sim$1–2 km s^{-1}. This fact indicates that not all the previously known TTSs were born in the molecular cloud cores which were gravitationally bounded by the Taurus molecular cloud and have moved with their proper motions. And the star formation in small clouds is generally occurred.

We propose that the large dispersion of proper motion comes from the inter-cloud velocity dispersion. There are 77 previously known clouds with measurement of CO radial velocity inside the studied region. Although the dispersion in radial velocity for the 77 known clouds is $\sim$5 km s^{-1}, the difference is thought to be caused by the availability of the cloud survey; small clouds (a few $\times$ M$_\odot$) locate only at low Galactic latitude ($|b| < 20°$), while clouds distributed to high latitude ($|b| > 20°$) are massive ($\gtrsim 100\,\mathrm{M}_\odot$). On the other hand, we found that the HI clouds, the genesis of molecular clouds, have large dispersion of $\sim$12 km s^{-1} in radial velocity. Here, there are substantial amount of hidden clouds which contribute the large velocity dispersion.

We also studied the differences of disk properties between TTSs associated to the clouds and isolated. The CTTS/WTTS ratios of AKARI detected TTSs are 81/31 and 12/16 for inside and outside the clouds, respectively. Considering the typical age of a CTTS and WTTS, TTSs associated to the clouds are relatively young. However, these numbers strongly depend on the sensitivity. We determined disk masses of 82 sources using the AKARI FIS data, but no remarkable difference was seen.

We further classified AKARI detected TTSs with their slopes (α) of the SED. From this classification, about a quarter of TTSs associated to clouds have envelopes and a few % of them are naked. On the other hand, a few % of isolated TTSs have envelopes and about one third of them are naked. This also supports the idea that TTSs associated to the clouds are relatively younger.

We could not distinguish any remarkable differences of disk properties between cloud TTSs and isolated TTSs. These results indicates that disk evolution processes seem to be the same.

Appendix A

The data reduction tools for the AKARI IRC slow-scan observations

A.1 IRC slow-scan mode

The Infrared Camera (IRC) on-board AKARI was originally designed to perform imaging and spectroscopic observations in the stirring pointing attitude. Later, the additional function for survey-type observations (scan mode) was developed (Ishihara et al. 2006). The scan mode was used for the All-Sky Survey and also in the pointed observation mode. The latter is called as slow-scan mode.

For the All-Sky Survey, we only observed in the *S9W* and *L18W* photometric bands. The data of two rows in the 256×256 detector arrays were selectively acquired by continuous and non destructive readout. The data were sampled at every 0.044 sec, and the pixels were reset at every 13.5 sec (or every 306 sampling) to discharge the photo-current. Since the scan speed was about $215''$ sec^{-1}, the pixel size in the in-scan direction is about $10''$. Because the pixel size of the detectors is $\sim 2\farcs5$, the output signals of every four adjacent pixels along each row were binned on board, so that the effective pixel size in the cross-scan direction is also about $10''$. Confirmation of a possible celestial signal detected by the first row is done by the data from the second row, successively observed the same sky independently. This procedure worked well in removing fake sources caused by spurious signals and charged particle hits, because the fake events are thought to occur only in one row. The spatial resolution can be improved to be $\sim 5''$ in the data reduction process, because the two independent rows are combined in the interlaced manner shown in Figure A.1.

The slow-scan observation mode has the same operation manner as in the All-Sky Survey mode. The major differences between the slow-scan and the All-Sky Survey are as follows.

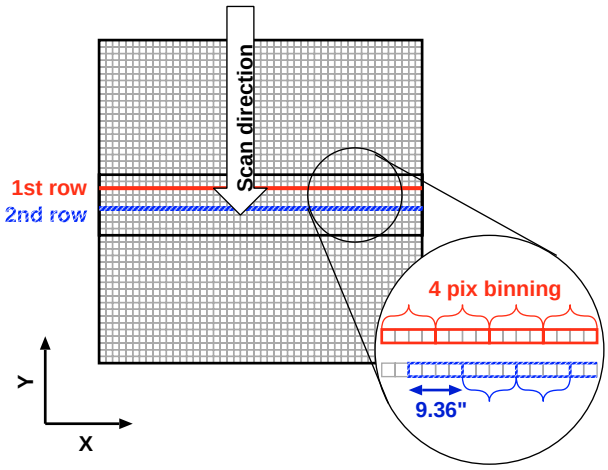

Figure A.1: Illustration of the array operation of the All-Sky Survey (from Ishihara et al. 2010). The data of two rows are selectively acquired, and every four adjacent pixels were binned. The binning of the second row shifts two pixels.

1. the telescope scans the sky with much slower speed (8, 15 or 30″ sec^{-1}) than that of the All-Sky Survey (215″ sec^{-1}).

2. the telescope scans along one or two round trip paths around the target object to take a redundant dataset.

Two ways of data sampling for the IRC slow-scan mode are defined by a set of Astronomical Observation Templates (AOT); one is called IRC11 which is compatible with the All-Sky Survey, and the other is called IRC51 which provides full pixel data without binning to realize the spatial resolution of $\sim$ 2.″5 in the cross-scan direction. The reset interval is also different, that the IRC51 mode reset every 51 sampling instead of 306 sampling in IRC11. Since the data is sampled every 0.044 sec, the spatial resolution in the in-scan direction is 0.″352, 0.″66, and 1.″32 for scan speeds of 8, 15, and 30″ sec^{-1}, respectively, in both the AOTs. The slow-scan operation is schematically shown in Figure A.2.

A.2 Data packages of the IRC slow-scan

The data packages are prepared in dedicated format called Time-Series Data (TSD), which is originally developed for the FIS (see Verdugo et al. 2007). The TSD is a binary FITS table and consists of header parts and arrays of data record (Figure A.3). A record (corresponds to a detector sampling) consists of the instrument data and necessary information from other house keeping (HK) instruments, as well as positional information given by the ground attitude determination processing. Since the sampling rate of these data are different to

each other, they are re-gridded by interpolation to synchronize with the clock of the detector so that all data are related to each other. All information from the main instrument is included in the TSD dataset, while only the subset of any information that is needed for the data reduction is provided from other instruments. Two data sets are created from one pointed observation for the MIR-S and MIR-L channels of the IRC.

A.3 AKARI data Reduction tools for the IRC Slow-scan (ARIS)

ARIS is developed on Interactive Data Language (IDL). Basic calibrations such as corrections of the non-linearity of the detector response, dark subtraction, flat fielding are applied onto the TSD format data. To create the images, we use Gridding Convolution Function (GCF) to re-grid onto a regular grid, since the data acquisition were not on a regular spatial grid. The flowchart of the reduction processes is sketched in Figure A.4. The conversion factors from the instrumental signal in an arbitrary data unit (ADU) to the physical flux density in Jy for point sources are derived from the observations of 4 and 3 standard stars for the *S9W* and *L18W* observations, respectively. The conversion factors for diffuse radiation are under investigation. For the IRC11 observations, we use the same correction procedures and parameters of the All-Sky Survey, except for the dark subtraction.

In the following sub-sections, we describe details of each correction procedure.

A.3.1 Reset anomaly correction

There is an anomalous behaviour of the detector output that persists a few seconds after the reset (reset anomaly). Figure A.5 explains this phenomenon. Since the offset level of the detector output is sensitive to the temperature (Ishihara et al. 2003), this anomaly is explained by the temperature drift caused by the reset current to discharge the stacked photo-electrons. The reset anomaly is corrected as

$$S_i^{(1)}(t) = S_i^{(0)}(t) - R(t), \tag{A.1}$$

where $S^{(0)}$, $S^{(1)}$, and R are the raw data, corrected data, and the correction offset, respectively. The suffix i indicates the pixel number and the t is the time (sampling) from the last reset. The correction offset is given by

$$R(t) = a_0 \times \exp(a_1 \times t) + a_2 \times \exp(a_3 \times t^2). \tag{A.2}$$

The parameters are tabulated in Table A.1.

Table A.1: Parameters of the reset anomaly correction.

	MIR-S	MIR-L
a_0	3.098	2.721
a_1	-0.1045	-0.08774
a_2	72.31	4.973
a_3	-0.4321	-0.1087

A.3.2 Linearity correction

The IRC detectors have non-linearity due to the decrease of the bias voltage during integration. This non-linearity is measured in the laboratory prior the launch. Figure A.6 shows the raw signal output versus the expected signal. The expected signal is derived by fitting the raw data of ADU < 15000 with a linear function. We then obtain the correction factors in a polynomial form as

$$S_i^{(2)} = \sum_{x=1}^{n} L_x \times (S_i^{(1)})^x, \tag{A.3}$$

where L_x are the coefficients. We apply $n = 7$ for both the MIR-S and -L detectors, and the parameters are listed in Table A.2.

The output signal is corrected by the polynomial. Figure A.7 shows the deviations of the corrected signals. After the correction, the error from the ideal linear line is better than 5% at 30000 and 35000 ADU for the MIR-S and MIR-L, respectively. From Figure A.6, the physical detector saturation occurs around 40000 ADU for both the detectors.

Table A.2: Parameters of the linearity correction.

	MIR-S	MIR-L
L_1	0.9977	0.9996
L_2	2.559×10^{-6}	-2.906×10^{-7}
L_3	-4.029×10^{-10}	5.278×10^{-10}
L_4	-7.599×10^{-15}	-1.132×10^{-13}
L_5	3.481×10^{-18}	8.722×10^{-18}
L_6	-1.387×10^{-22}	-2.659×10^{-22}
L_7	1.722×10^{-27}	2.913×10^{-27}

A.3.3 Differentiation

Since the raw signal from the detector of the scan observations are integrated data, we differentiate it with respect to time as

$$S_i^{(3)}(t) = S_i^{(2)}(t) - S_i^{(2)}(t - \Delta t), \tag{A.4}$$

where Δt is the data sampling interval and fixed as 0.044 sec.

A.3.4 Dark subtraction

The slow-scan observation mode takes dark frames during the manoeuvre at before and after of the each observation. We calculate the dark signal per pixel by taking the median value from all dark frame data, then subtract it from the data, assuming that the dark level is almost constant in an observation

$$S_i^{(4)} = S_i^{(3)} - D_i, \tag{A.5}$$

where D is the dark signals.

A.3.5 Flat fielding

We construct the flat-field data from ∼200 observations of the south ecliptic pole (SEP) region by taking the median value for each pixel. The correction is applied as

$$S_i^{(5)} = S_i^{(4)}/F_i, \tag{A.6}$$

where F is the normalized flat correction factor (see Figure A.8).

A.3.6 Masking bad pixels

We mask invalid data such as

1. pixels which are masked out for the slit spectroscopy,
2. all pixels just after the resets because they have heavy reset anomaly,
3. all the saturated samplings.

A.3.7 Image reconstruction

Finally, the image map is created from the calibrated scan data. In this process, we use GCF to re-grid the sampling data onto a regular grid. The successful/default parameters are the Gaussian kernel with full width at half maximum (FWHM) of 1 pixel, where the pixel size is $\sim 2\farcs5$ pixel^{-1} and $\sim 5''$ pixel^{-1} for the IRC51 and IRC11 observations, respectively. To abandon charged particle hitting data, we perform 5-σ clipping within 1 pixel radius. We have three choices of the position information,

1. the one which were determined by the on board attitude and orbit control system (AOCS),
2. the one which were re-processed on the ground, called G-ADS (ground-based attitude determination system),
3. the 'self-pointing reconstruction' method which modifies the above data (see section A.4).

A.4 Self-pointing reconstruction

The AOCU or G-ADS information have positional accuracy of typically $\sim 10''$ (see Figure A.9 *left*). Although this satisfies the required absolute error of $\sim 30''$, it is not accurate enough compared to the spatial resolution of the IRC observations of $\sim 2''.5$ or $\sim 5''$ at the IRC51 or IRC11 observations, respectively. Therefore, we developed a software to make a time dependent correction of scanned position based on the observed data by comparing with the positions of detected point sources with those in the reference catalogue. This process is called self-pointing reconstruction (self-PR).

The self-PR procedure are described as follows.

1. First, we make an initial image of each forward/backward scan using either AOCS or G-ADS position data.
2. Second, we extract point sources and save their observed time and positions.
3. Third, we do cross-identification between the detected sources with a position reference catalogue (usually 2MASS PSC), and the position differences are evaluated. Here, the position differences are measured in in-scan and cross-scan direction.
4. Next, we take mean values of the differences with given (30 sec by default) time width, and then, interpolate these values (see Figure A.9 *middle*).
5. Finally, we apply the correction to the position information and make the final image from all forward/backward scans.

The final position is as accurate as about $1''$ (Figure A.9 *right*).

A.5 Flux calibration

A.5.1 Observed standard stars and data processing

For the absolute flux calibration, we observed 4 and 3 infrared standard stars (Cohen et al. 1999) for *S9W* and *L18W* bands, respectively (Table A.3). These observations were carried out by IRC51.

The raw data were processed by the ARIS, and the final images are created using the self-PR method. We applied aperture photometry to the final image. We used DAOPHOT-Type Photometry Procedures of GCNTRD and APER in the IDL Astronomy User's Library (Landsman 1993) (version 2007 May). The radius of the aperture is 7.5 pixels and the sky value is estimated by the annulus of 7.5–12.5 pixel radii.

A.5.2 Estimation of the in-band flux density

The in-band flux density of each band at the effective wavelength, $f_\lambda^{\rm quoted}(\lambda)$ is calculated by the following equation

$$f_\lambda^{\rm quoted}(\lambda_i) = \frac{\int_{\lambda_{is}}^{\lambda_{ie}} R_i(\lambda)\lambda f_\lambda(\lambda) d\lambda}{\int_{\lambda_{is}}^{\lambda_{ie}} (\lambda_i/\lambda) R_i(\lambda)\lambda d\lambda}, \tag{A.7}$$

where $f_\lambda(\lambda)$ is the flux density of a standard star SED (provided by M. Cohen) and $R_i(\lambda)$ is the spectral response function (including the transmission of the optics and the response of the detector) of the band i. Here $f_\lambda \propto \lambda^{-1}$ is assumed. This is the convention adopted by IRAS, COBE, ISO, Spitzer/IRAC, and other AKARI observations (Tanabé et al. 2008, Ishihara et al. 2010)

A.5.3 Conversion factor

The relations between the pipeline output ADUs and the calculated in-band flux densities of the standard stars are shown in Figure A.10. A straight line was fitted to these data and the slope of the fitted lines provides the conversion factors f_0(ADUtoJy). The factors are tabulated in Table A.4.

A.5.4 Comparison with the AKARI IRC PSC

We compared the flux densities of the sources around the Chamaeleon I molecular cloud with the AKARI IRC PSC to verify the flux calibration of the IRC slow-scan mode. About 900 and 150 sources are detected in the observed region with the IRC slow-scan observations at the *S9W* and *L18W* bands, respectively. We searched these sources in the IRC PSC, and found 203 and 69 matches in the *S9W* and *L18W* bands, respectively. Figure A.11 shows the flux density ratios of the slow-scan to PSC as a function of the slow-scan flux. It seems that the ratios of the faint (<0.1 Jy) *S9W* sources drops systematically to ∼0.6–0.7. This result is thought to be caused by a 'flux-boost' effect[1] in the IRC PSC. Actually, the completeness of the IRC PSC is only ∼50% at $f(9\mu{\rm m}) = 0.1$ [Jy] (see Figure

[1]If a source is as faint as the noise level, we can detect it only when the signal is unevenly bright.

20 and Table 3 of Ishihara et al. 2010), and thus, many fain sources are absent from the IRC PSC. The mean values and standard deviations of the ratios are tabulated in Table A.5.

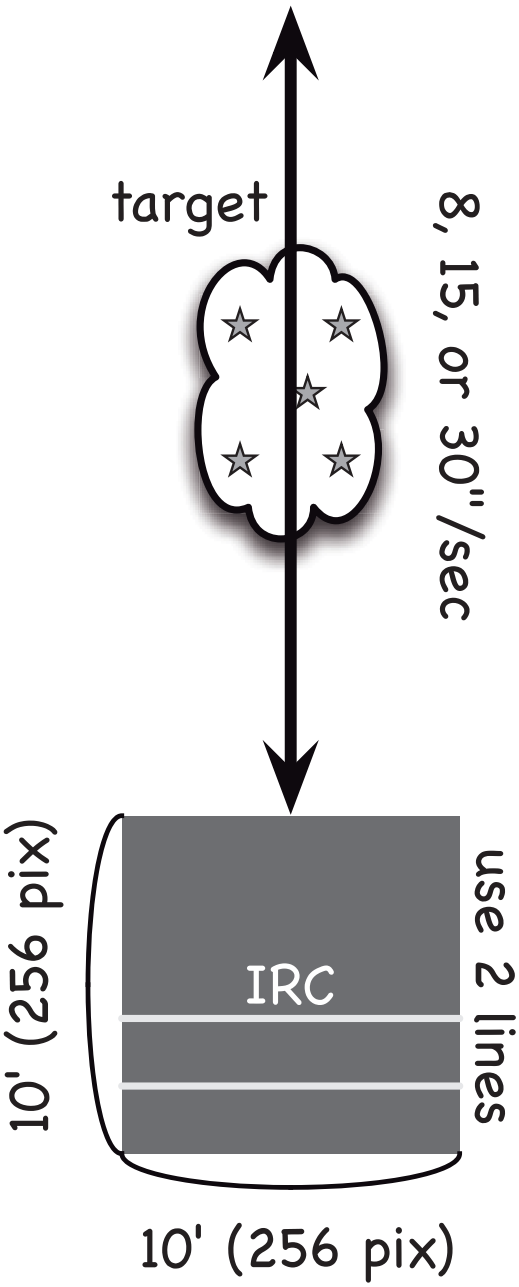

Figure A.2: Schematic illustration of the slow-scan observations. The telescope (and thus, the detector) scans along one or two round trip paths around the target object, with speeds of 8, 15, or 30″ sec^{-1}.

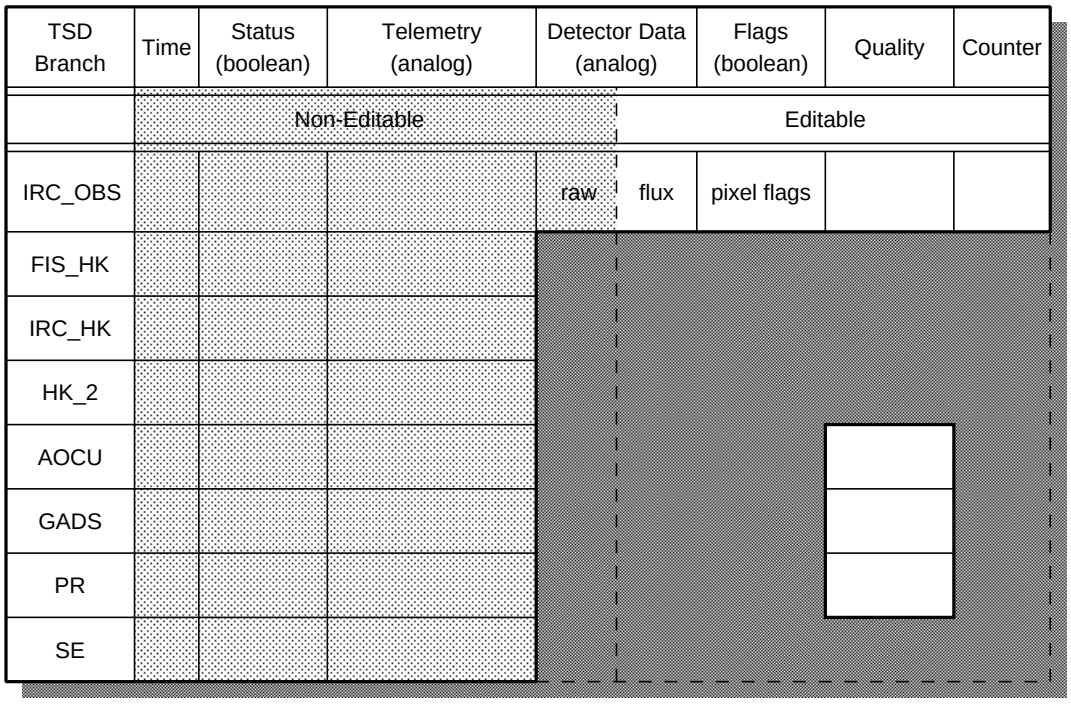

Figure A.3: An overview of Time Series Data (TSD) structure (modified Figure 6.1.1 of Verdugo et al. 2007).

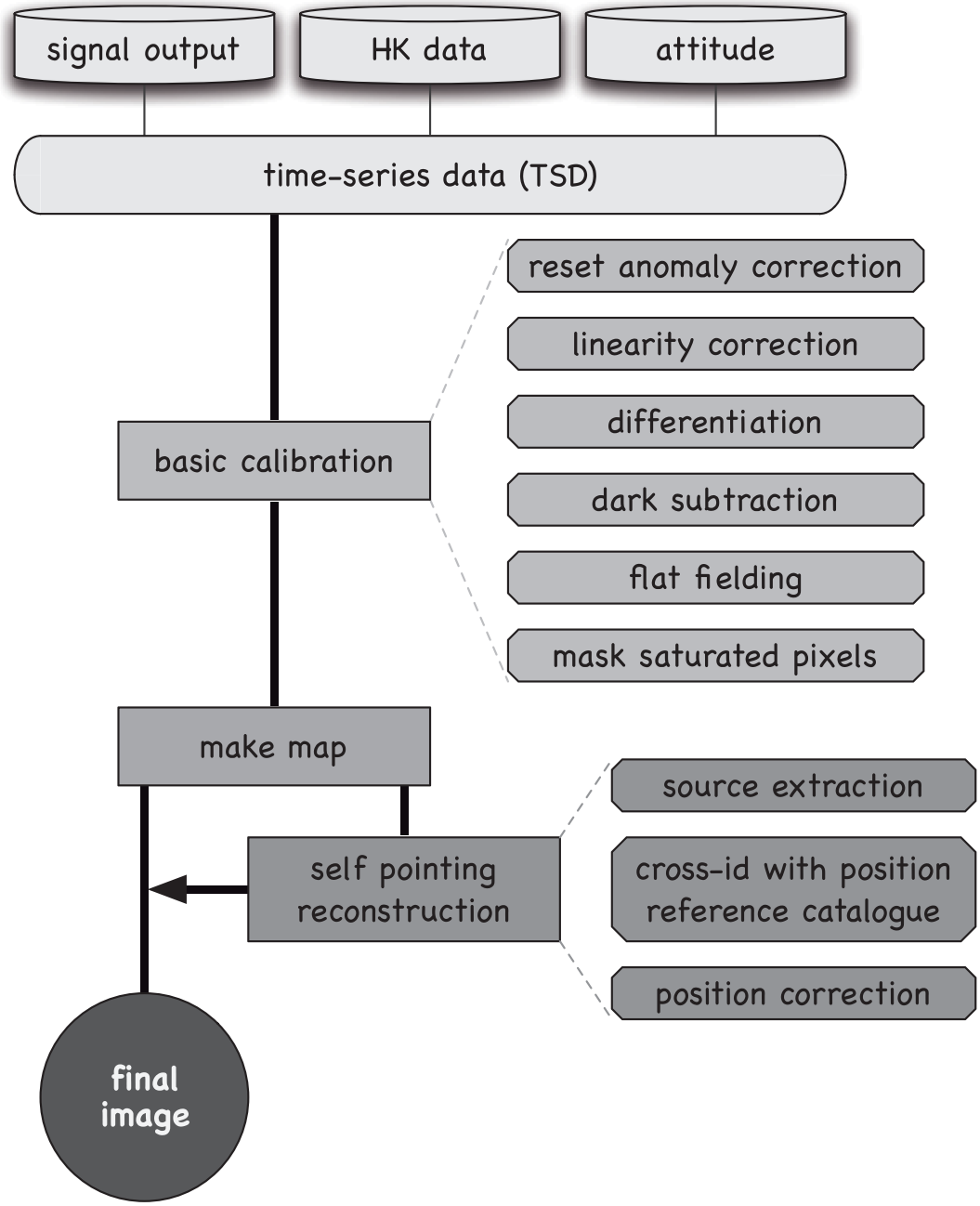

Figure A.4: Flowchart of the data reduction for the IRC slow-scan.

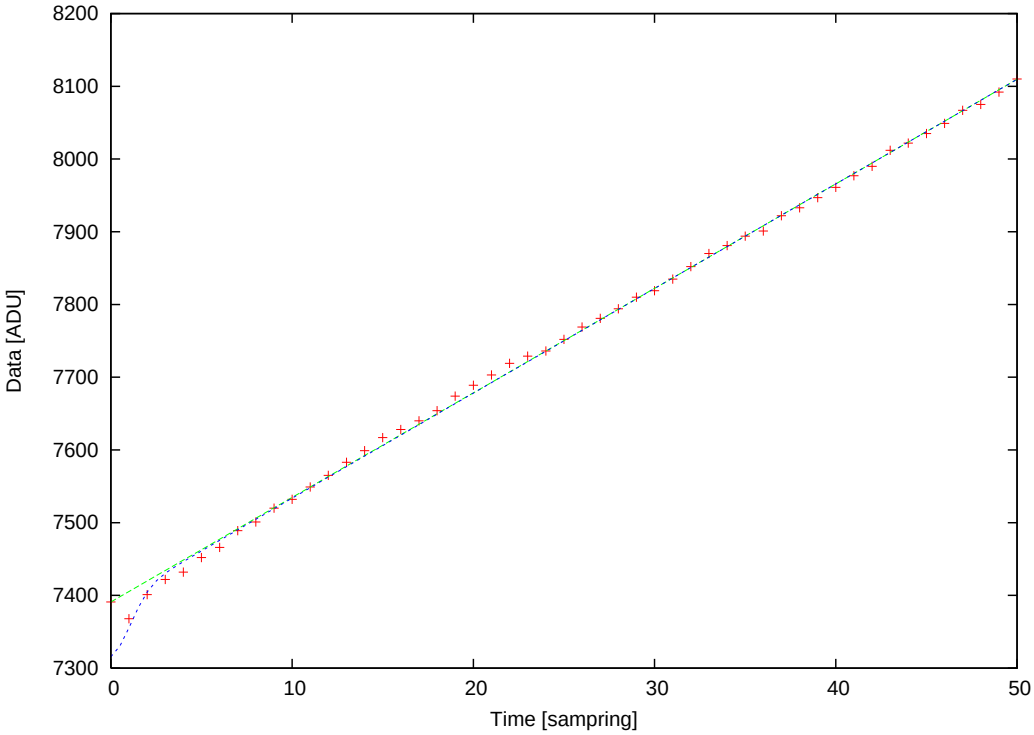

Figure A.5: An example of the reset anomaly correction. The red crosses are the output signal of a pixel from observed sky. The green broken line is a linear function of $a + b \times t$, where t is the sampling from the last reset, fitted from $5 < t < 51$. The blue curve indicates the correction function.

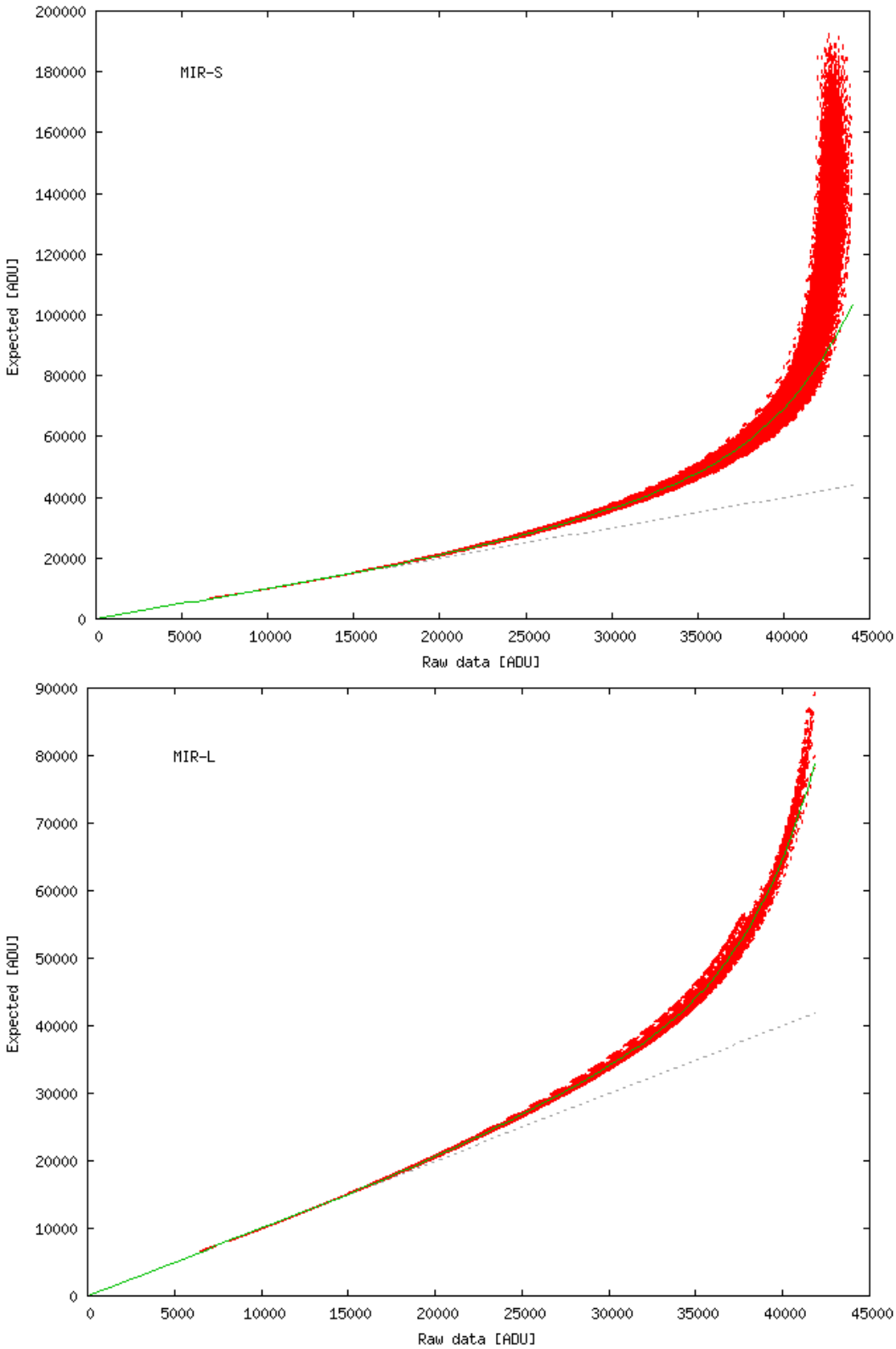

Figure A.6: The raw signal versus expected signal plot for the MIR-S (*top*) and MIR-L (*bottom*) detectors. The green curve is fitted function with equation (A.3).

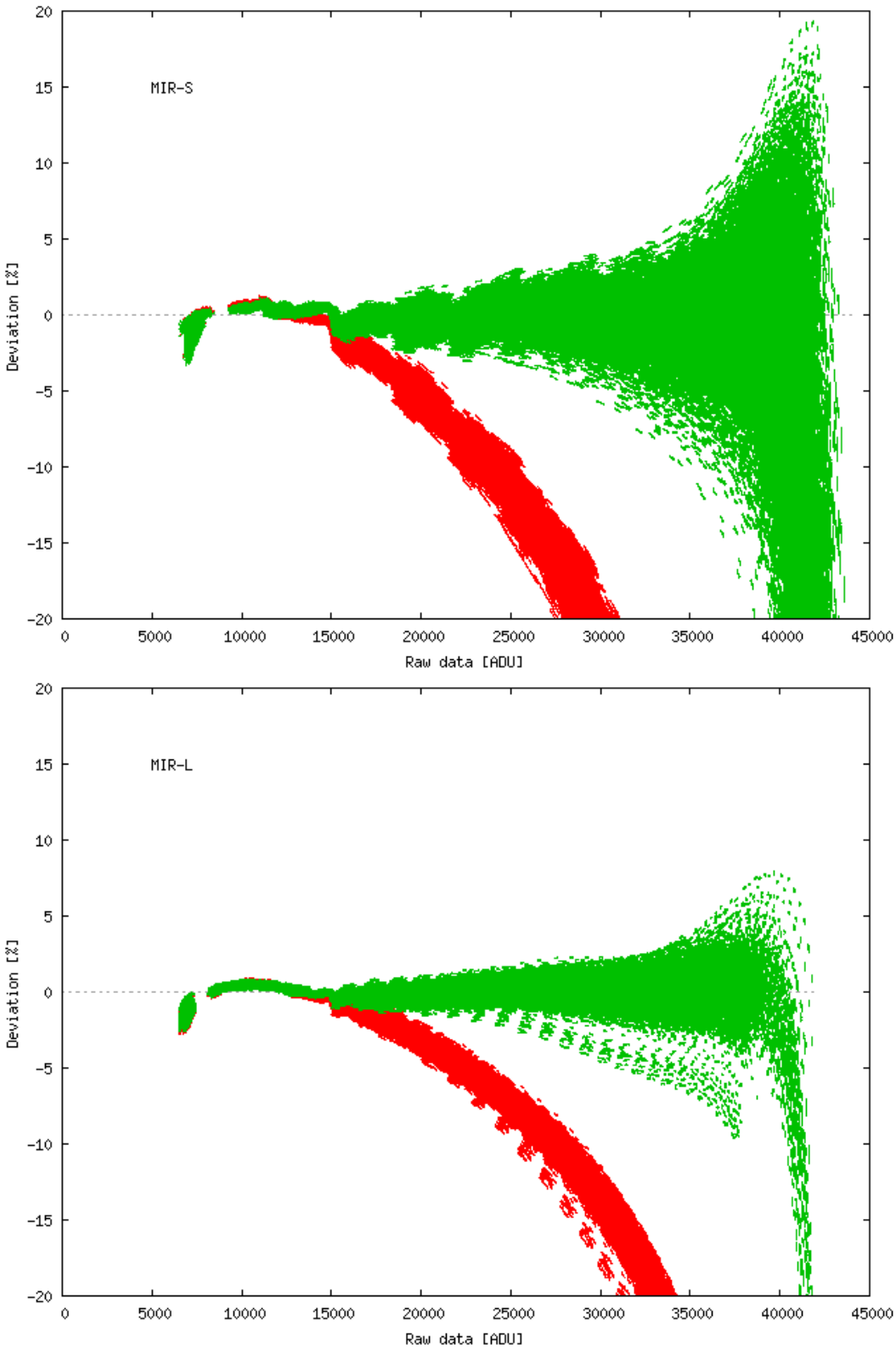

Figure A.7: The deviations of the corrected signals for the MIR-S (*top*) and MIR-L (*bottom*) detectors. The red dots are the deviations of the raw data from the equation (A.3), and the green dots are those of the corrected data.

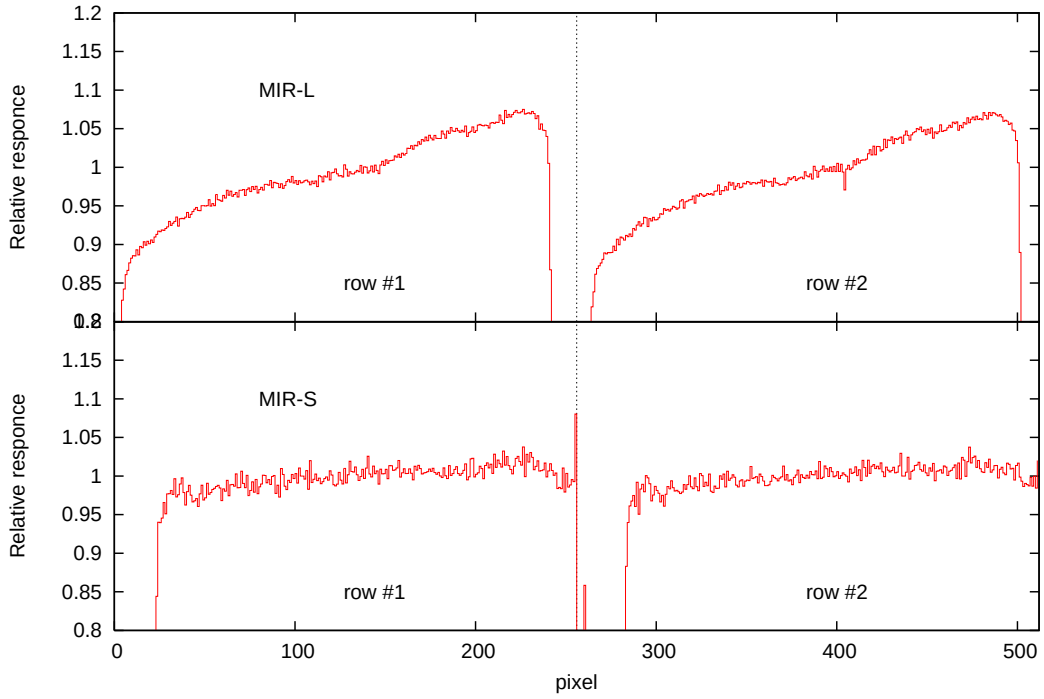

Figure A.8: Flat data for the *S9W* band (bottom) and *L18W* band (top), normalized to the mean value of pixels 25–256 and 281–512 for *S9W* and 2–236 and 258–492 for *L18W*.

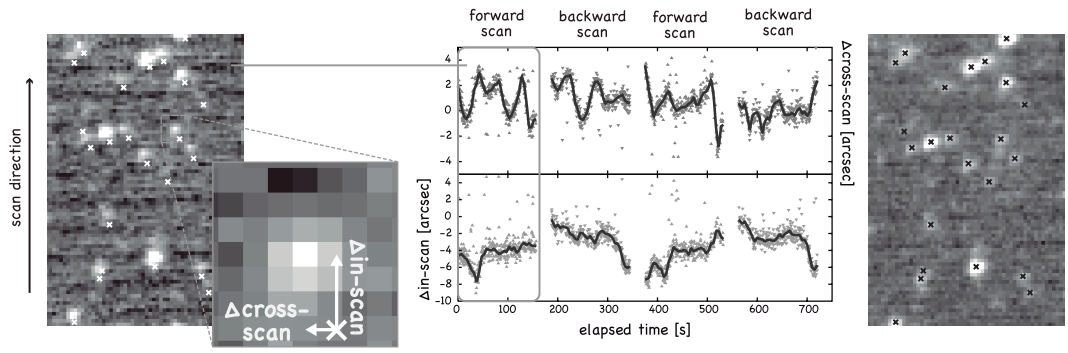

Figure A.9: An example of the self-pointing reconstruction. (*left*) The 9 μm image from the first forward-scan using the satellite telemetry and its magnified image of a point source. The crosses are the positions of 2MASS point sources. (*middle*): Time vs. Δcross-scan (top) and Δin-scan (bottom) deviation. The thick curves indicate trend of the differences. (*right*): The final image based on the corrected position data by the self-pointing reconstruction.

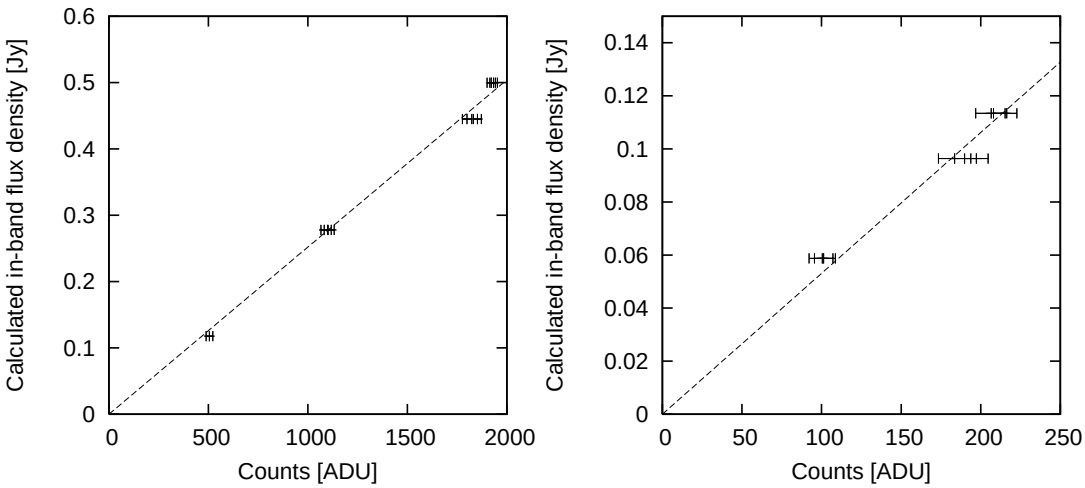

Figure A.10: Estimated flux density versus observed ADU of the standard stars for the *S9W* (*left*) and *L18W* (*right*) bands. A broken line in each plot is the least-squares fit to the data.

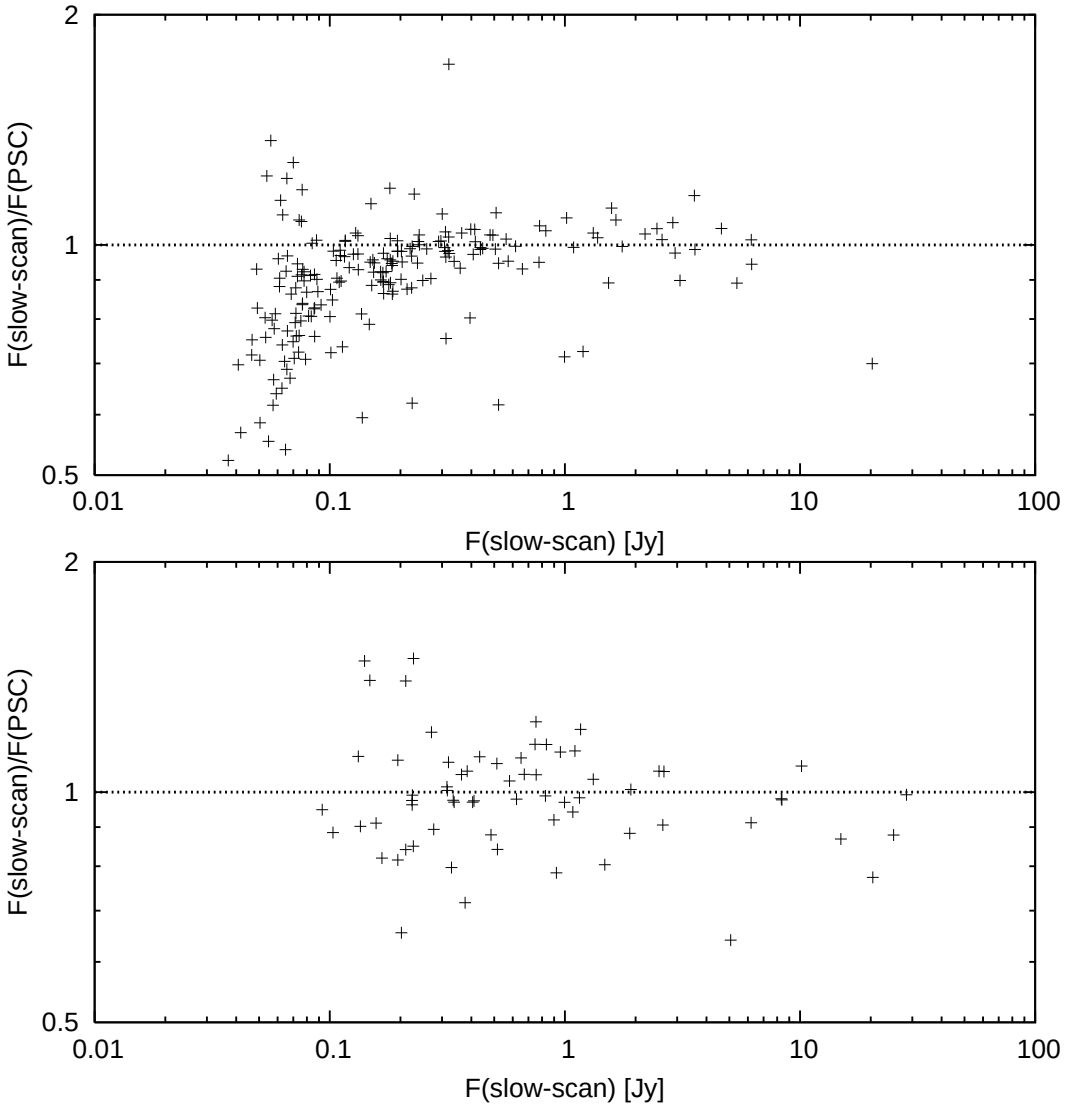

Figure A.11: The flux density ratios of the slow-scan to the IRC PSC as a function of the slow-scan flux densities for the *S9W* (*top*) and *L18W* (*bottom*) band.

Table A.3: Observed standard stars.

Star	2MASS ID	Spectrum	Expected flux†		Observation		
			S9W [Jy]	*L18W* [Jy]	date (UT)	ID	parameter‡
BD+62 1588	17564731+6220553	K5 III	4.9966×10^{-1}	1.1341×10^{-1}	2007-03-13 23:59:21	5124045 1	i;N;15
					2007-03-14 01:38:43	5124046 1	i;N;30
					2007-03-16 00:00:36	5124047 1	i;L;15
					2007-03-16 01:39:57	5124048 1	i;L;30
HD 42525	06060937−6602227	A0 V	2.7792×10^{-1}	5.8763×10^{-2}	2007-05-02 09:00:33	5124066 1	i;N;30
					2007-05-03 01:34:32	5124065 1	i;N;15
					2007-05-04 23:57:43	5124067 1	i;L;15
					2007-05-05 01:37:07	5124068 1	i;L;30
HD 46819	06302274−6601230	K0 III	4.4501×10^{-1}	9.6344×10^{-2}	2007-06-06 00:46:43	5124108 1	a;N;15
					2007-06-06 02:26:08	5124109 1	a;N;30
					2007-06-17 01:56:29	5124110 1	i;L;15
					2007-06-20 02:51:59	5124111 1	i;L;30
BD+66 1060	17560018+6655430	K2 III	1.1766×10^{-1}	2.6382×10^{-2}	2007-08-02 04:29:25	5124130 1	a;N;30

† Flux density for each band estimated from equation (A.7).
‡ The first character 'a' and 'i' indicates one and two round trips, respectively. The second parameter expresses that the target source is observed with MIR-S ('N') or MIR-L ('L') channel. The last numeral is the scan speed in arcsec sec^{-1}.

Table A.4: Conversion factor f_0 [Jy ADU^{-1}]

Band	f_0	Error
S9W	2.518×10^{-4}	3.228×10^{-6}
L18W	5.291×10^{-4}	1.365×10^{-6}

Table A.5: Mean values and standard deviations of the flux ratio between Slow-scan and the All-Sky Survey

Band	MEAN	STDDEV	n_{star}
S9W	0.915	0.198	203
(> 0.1[Jy])	0.957	0.195	131
L18W	0.986	0.197	69

Appendix B

AKARI FIS slow-scan observations of Weak-line T Tauri stars around the Chamaeleon region

B.1 Observations and Data Reduction

To determine the protoplanetary disk mass of weak-line T Tauri stars (WTTSs), we performed FIS observations of 31 previously known WTTSs toward the Chamaeleon star forming region. These WTTSs were found by ROSAT, and are isolated from the clouds (see Figure B.1). The FIS was operated in a photometry mode, and observed in four bands: *N60* (65 μm), *WIDE-S* (90 μm), *WIDE-L* (140 μm), and *N160* (160 μm). We used astronomical observation template (AOT) FIS01, which performs two round-trips with a 70″ cross-scan step. A summary of the observations is given in Table B.1.

The FIS slow-scan data were processed with the AKARI standard data reduction tool kit. We used local flat option, and the sigma clipping threshold of 1.5. The resulting maps were created as $12' \times 12'$ postage stamps centred at the positions of the target objects. The pixel scale is 15″ pix^{-1} for the *N60* and *WIDE-S* bands, and 30″ pix^{-1} for the *WIDE-L* and *N160* bands. The typical 1σ noise levels are 0.766, 0.317, 0.622, and 0.977 MJy sr^{-1} at 65, 90, 140, and 160 μm, respectively.

Since there were no possible emission from the disks at all, we stacked the images to improve the sensitivity. We subtracted background from each image, because the background levels were varied. We then, created images for 4 bands, taking mean values in each pixel. The stacked maps have 1σ sensitivities of 0.208, 0.0706, 0.118, and 0.195 MJy sr^{-1} at 65, 90, 140, and 160 μm, respectively.

B.2 Results and Discussion

Figure B.2 shows the resultant images. There exists no significant peak at the centre of the stacked images despite of our expectation of possible disk presence. The 1σ noise levels for point sources are evaluated to be 10.4, 3.53, 8.88, and 14.7 mJy at 65, 90, 140, and 160 μm, respectively. If we assume that the disk is optically thin, the disk mass is estimated by the following equation

$$M_{\rm disk} = F_\nu \times \left[\frac{d^2}{B_\nu(T_{\rm dust})\kappa_\nu} \right], \tag{B.1}$$

where $B_\nu(T)$ is the Planck function, $T_{\rm dust}$ the dust temperature, κ_ν the dust mass absorption coefficient, and d the distance to the target. Adopting the absorption coefficient for the astronomical silicate (Weingartner & Draine 2001), distance of 160 pc, and the dust temperature of 50 K (typical value for primordial disks), the disk masses corresponding to the 5σ flux densities are 1.08, 0.461, 2.53, and 5.70 $M_\oplus$ at 65, 90, 140, and 160 μm, respectively. These masses are smaller than typical disk mass of primordial disks around Classical T Tauri stars (CTTSs) ($\sim$100 $M_\oplus$), and comparable to that of debris disks around main-sequence stars ($\lesssim$1 $M_\oplus$). Considering that the disks around WTTSs are intermediate between those around CTTSs and main-sequence stars, we could detect disk emission.

Since the estimated mass in above paragraph consider only one photometric band, we also calculate the SED with simple optically thin disk model. The observed flux from disk thermal emission is given by integrating the intensity over the solid angle,

$$\begin{aligned} F_{\rm disk} &= \int I_\nu \, \mu \, d\Omega, & \text{(B.2)} \\ &= \frac{2\pi}{d^2} \int_{r_\circ}^{r_D} [1 - \exp(-\tau_\nu(r))] \, B_\nu(T_r) \, \cos\theta \, r \, dr, & \text{(B.3)} \\ &= \frac{4\,\pi\,h\,\nu^3}{d^2\,c^2} \int_{r_\circ}^{r_D} [1 - \exp(-\tau_\nu(r))] \, \frac{\cos\theta \, r \, dr}{\exp(\frac{h\,\nu}{kT_r}) - 1}, & \text{(B.4)} \end{aligned}$$

where r_D and $r_\circ$ are the outer and inner disk radius, τ is the disk opacity, and θ is the inclination angle of the disk with respect to the line of sight. Assuming that the disk is optically thin, this equation can be simplified as

$$F_{\rm disk} = \frac{4\,\pi\,h\,\nu^3}{d^2\,c^2} \int_{r_\circ}^{r_D} \tau_\nu(r) \, \frac{\cos\theta \, r \, dr}{\exp(\frac{h\,\nu}{kT_r}) - 1}. \tag{B.5}$$

The opacity is given by absorption coefficient κ_ν and surface density Σ

$$\tau_\nu = \frac{\kappa_\nu \Sigma}{\cos\theta}. \tag{B.6}$$

We use an usual simplifying assumption that the disk surface density can be represented by power law:

$$\Sigma = \Sigma_\circ (r/r_\circ)^p. \tag{B.7}$$

Here, the expected flux density can be written as

$$F_{\rm disk} = \frac{4\,\pi\,h\,\nu^3\,\Sigma_\circ}{d^2\,c^2} \int_{r_\circ}^{r_D} \frac{\kappa_\nu\,(\frac{r}{r_\circ})^p\,r\,dr}{\exp(\frac{h\,\nu}{kT_r}) - 1} \tag{B.8}$$

To calculate this equation, we assume $p = -1.5$ (typical value) and that the dust temperature obeys following equation

$$T_r = \left(\frac{L_\star}{16\,\pi\,r^2\,\sigma}\right)^{1/4}, \tag{B.9}$$

where $L_\star$ is stellar luminosity and σ is the Stefan-Boltzmann constant. We examine three models; $M_{\rm disk} = 0.1\,{\rm M}_\oplus$ and $r_\circ = 1$ [AU], $M_{\rm disk} = 0.1\,{\rm M}_\oplus$ and $r_\circ = 5$ [AU], and $M_{\rm disk} = 1\,{\rm M}_\oplus$ and $r_\circ = 30$ [AU] (see Figure B.3). We conclude that the upper limit of the disk mass around WTTS in the Chamaeleon regions seems to be 1 $\rm M_\oplus$.

Table B.1: Observation log

Object†	RA	Dec	Date	OBS ID	Parameter‡
0842.4−8345	130.594563	−83.756527	2006-09-11 17:58:47	1600340	1.0;15;70
1039.5−7538	159.880821	−75.633859	2007-02-11 16:13:08	1600337	1.0;15;70
1219.7−7403	184.931250	−74.065806	2007-02-14 03:47:02	3130033	1.0;15;70
1220.4−7407	185.101667	−74.123667	2007-02-14 23:38:56	3130034	1.0;15;70
0901.0−7715	135.247917	−77.254556	2007-02-15 01:21:40	3130003	1.0;15;70
0919.4−7738	139.849583	−77.645806	2007-02-16 02:11:17	3130005	1.0;15;70
1159.7−7601	179.921250	−76.023667	2007-02-16 03:48:06	3130024	1.0;15;70
1224.8−7503	186.199167	−75.051833	2007-02-16 23:39:32	3130037	1.0;15;70
1207.9−7555	181.978750	−75.922694	2007-02-17 01:19:14	3130030	1.0;15;70
1220.6−7539	185.148333	−75.657389	2007-02-17 02:58:21	3130035	1.0;15;70
0849.2−7735	132.292941	−77.595060	2007-02-17 11:18:17	1600362	1.0;15;70
1239.4−7502	189.845000	−75.044167	2007-02-18 00:29:15	3130041	1.0;15;70
1233.5−7523	188.375417	−75.390250	2007-02-18 02:08:44	3130040	1.0;15;70
1243.1−7458	190.766667	−74.974056	2007-02-18 03:47:51	3130042	1.0;15;70
1150.4−7704	177.606250	−77.078722	2007-02-18 23:40:52	3130019	1.0;15;70
1202.8−7718	180.711667	−77.309833	2007-02-19 01:20:03	3130027	1.0;15;70
1320.0−7406	199.987917	−74.102667	2007-02-20 00:29:07	3130045	1.0;15;70
1204.6−7731	181.145958	−77.527833	2007-02-20 02:10:01	3130028	1.0;15;70
1158.5−7754a	179.620417	−77.909583	2007-02-20 03:49:29	3130021	1.0;15;70
0946.9−8011	146.717920	−80.197559	2007-02-24 15:27:57	1600339	1.0;15;70
1117.0−8028	169.254167	−80.470278	2007-02-25 01:22:54	3130016	1.0;15;70
1207.7−7953	181.930417	−79.886389	2007-02-25 03:01:38	3130029	1.0;15;70
0848.0−7854	131.996667	−78.916167	2007-02-25 04:43:26	3130002	1.0;15;70
1217.4−8035	184.359583	−80.586028	2007-02-26 02:12:19	3130032	1.0;15;70
1009.6−8105	152.407083	−81.096528	2007-02-26 03:53:03	3130014	1.0;15;70
1325.7−7955	201.427500	−79.923500	2007-03-01 01:23:05	3130046	1.0;15;70
1415.0−7822	213.757500	−78.370111	2007-03-02 02:12:26	3130049	1.0;15;70
1125.8−8456	171.458704	−84.945312	2007-03-07 04:46:05	1600336	1.0;15;70
1007.7−8504	151.922030	−85.077777	2007-03-09 04:47:34	1600973	1.0;15;70
1014.2−7636	153.545414	−76.607359	2007-08-19 00:24:03	1602622	2.0;8;70
1129.2−7546	172.302909	−75.773333	2007-08-20 01:17:59	1602619	2.0;8;70

†: The source full name is as RXJ 0123.4−5432.
‡: The first value is integration time (sec). The second one is scan speed (arcsec sec^{-1}). The last one is step width in the cross-scan direction (arcsec) between the two sets of round trips.

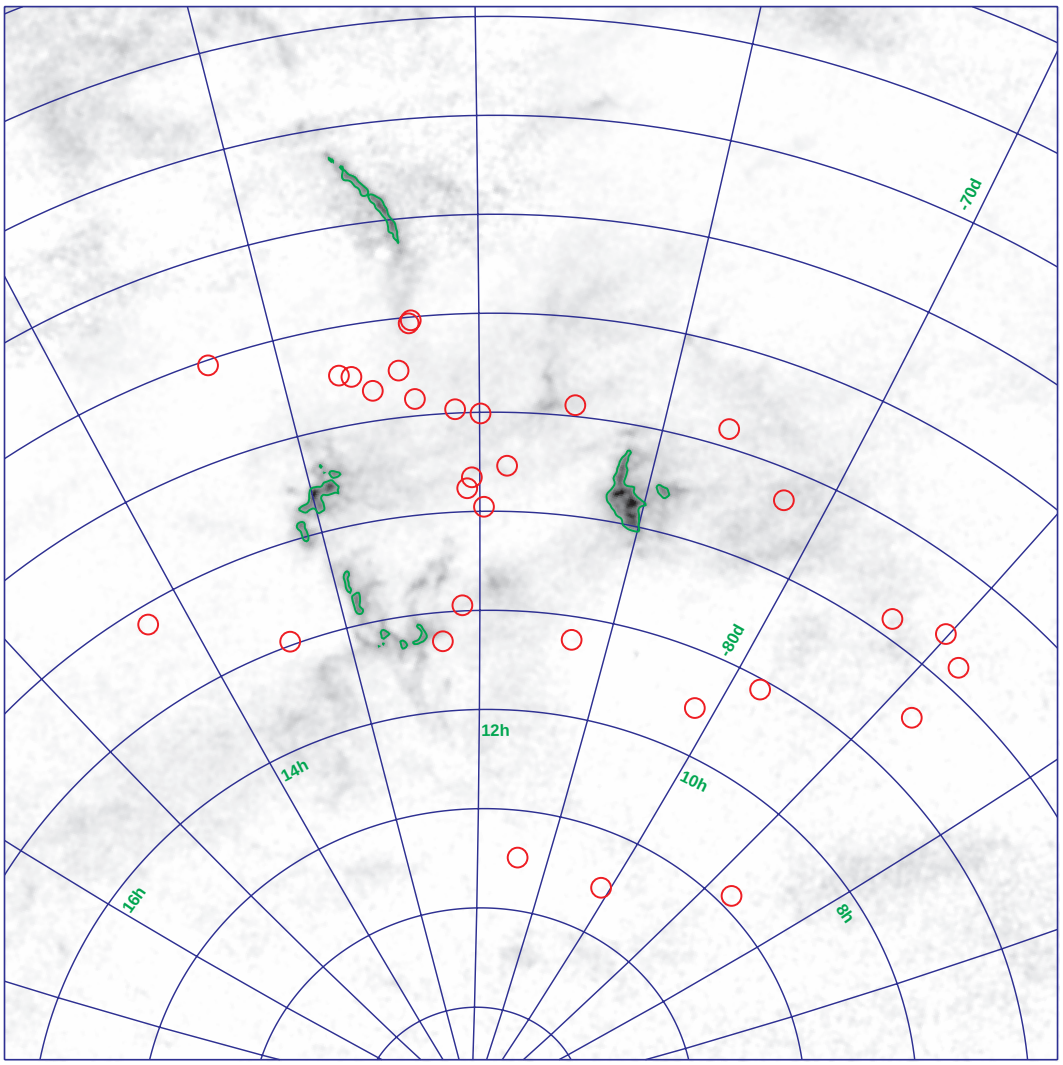

Figure B.1: Distribution of the observed WTTSs. The grey scale is the extinction map (from Dobashi et al. 2005) and the green contours indicate the extinction of $A_V = 2$.

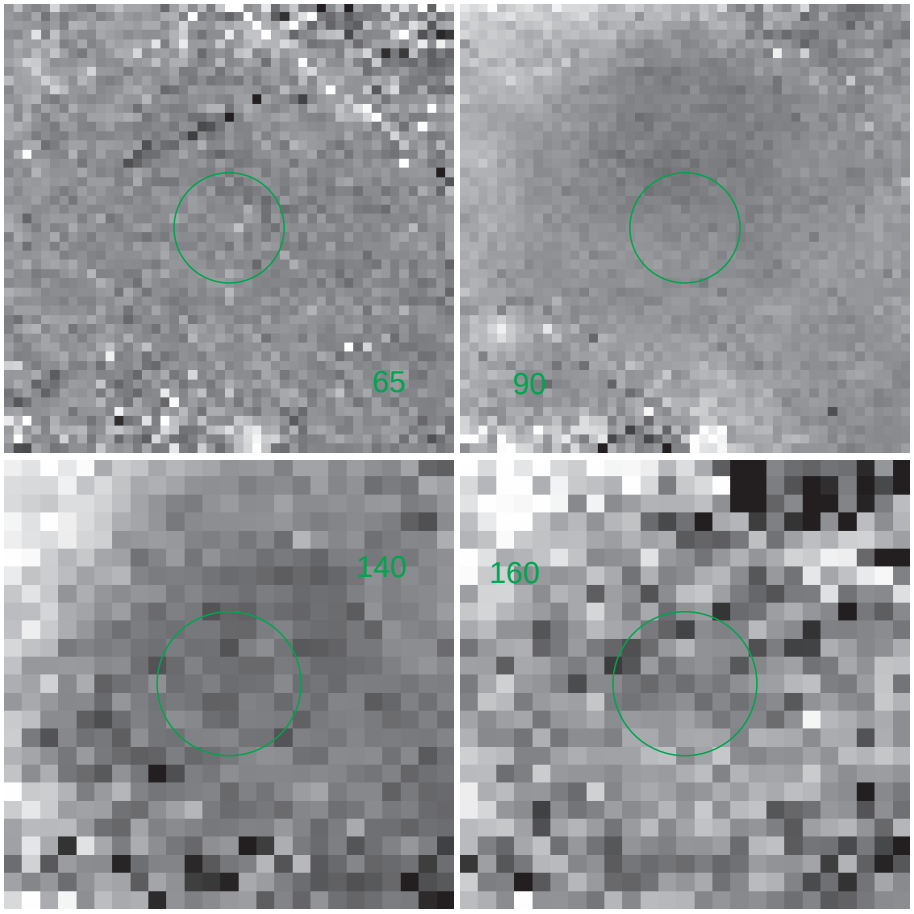

Figure B.2: The stacked image of WTTSs at the *N60* (*top-left*), *Wide-S* (*top-right*), *Wide-L* (*bottom-left*), and *N160* (*bottom-right*). Green circles indicate the position of the source.

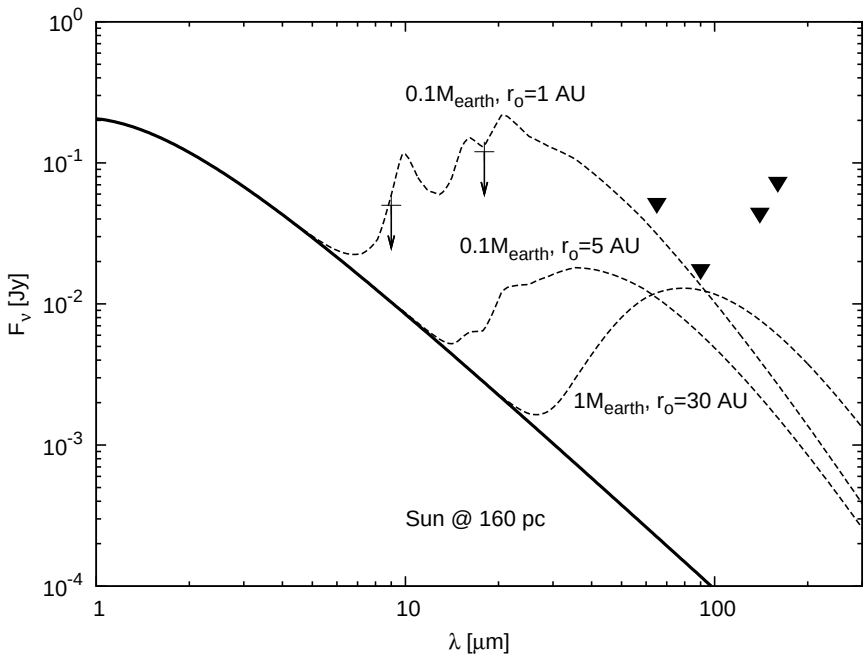

Figure B.3: SED of optically thin disk model. The solid curve indicates the Sun at a distance of 160 pc. The broken curves are the expected disk thermal emission for 0.1 $M_\oplus$ and $r_\circ = 1$ AU, 0.1 $M_\oplus$ and $r_\circ = 5$ AU, and 1 $M_\oplus$ and $r_\circ = 30$ AU. The triangles are the 5σ noise levels of the FIS band. Two arrows show the 5σ detection limit of the AKARI IRC All-Sky Survey (50 and 120 mJy at 9 and 18 μm bands, respectively).

References

Acker, A., Ochsenbein, F., Stenholm, B., et al., 1994, VizieR Online Data Catalog, 5084, 0

Adams, F. C., Lada, C. J., & Shu, F. H., 1988, ApJ, 326, 865

Alcala, J. M., Krautter, J., Schmitt, J. H. M. M., et al., 1995, A&AS, 114, 109

Alcala, J. M., Terranegra, L., Wichmann, R., et al., 1996, A&AS, 119, 7

Alcala, J. M., Krautter, J., Covino, E., et al., 1997, A&A, 319, 184

Alves, J. F., Lada, C. J., & Lada, E. A. 2001, Nature, 409, 159

André, P., 1994, The Cold Universe, 179

Becklin, E. E., & Neugebauer, G., 1967, ApJ, 147, 799

Beckwith, S. V. W., Sargent, A. I., Chini, R. S., & Guesten, R., 1990, AJ, 99, 924

Beichman, C. A., Myers, P. C., Emerson, J. P., et al., 1986, ApJ, 307, 337

Beichman, C. A., Neugebauer, G., Habing, H. J., Clegg, P. E., & Chester, T. J., 1988, Infrared Astronomical Satellite (IRAS) Catalogs and Atlases, NASA RP-1190

Bertout, C., 1989, ARA&A, 27, 351

Bok, B. J., & Reilly, E. F., 1947, ApJ, 105, 255

Carpenter, J. M., Bouwman, J., Mamajek, E. E., et al., 2009, ApJS, 181, 197

Cieza, L., Padgett, D. L., Stapelfeldt, K. R., et al., 2007, ApJ, 667, 308

Cohen, M. & Kuhi, L. V., 1979, ApJS, 41, 743

Cohen, M.,Walker, R. G., Carter, B., et al. 1999, AJ, 117, 1864

Currie, T. & Kenyon, S. J., 2009, AJ, 138, 703

Currie, T., Lada, C. J., Plavchan, P., et al., 2009, ApJ, 698, 1

Dobashi, K., Uehara, H., Kandori, R., et al., 2005, PASJ, 57, 1

Dutra, C. M. & Bica, E., 2002, A&A, 383, 631

Evans, N. J., Dunham, M. M., Jørgensen, J. K., et al., 2009, ApJS, 181, 321

Feigelson, E. D., and Decampli, W. M., 1981, ApJ, 243, L89

Feigelson, E. D., 1996, ApJ, 468, 306

Furlan, E., Hartmann, L., Calvet, N., et al., 2006, ApJS, 165, 568

Gramajo, L. V., Whitney, B. A., Gómez, M., & Robitaille, T. P., 2010, AJ, 139, 2504

Gomez, M., Hartmann, L., Kenyon, S. J., & Hewett, R., 1993, AJ, 105, 1927

Güdel, M., Briggs, K. R., Arzner, K., et al., 2007, A&A, 468, 353

Harris, S., Clegg, P., & Hughes, J., 1988, MNRAS, 235, 441

Hartmann, D. & Burton, W. B., 1997, Atlas of Galactic Neutral Hydrogen

Harvey, P., Merín, B., Huard, T. L., et al., 2007, ApJ, 663, 1149

Hayashi, C., Nakazawa, K., & Nakagawa, Y., 1985, Protostars and Planets II, 1100

Herbig, G. H. & Bell, K. R., 1988, Third Catalog of Emission-Line Stars of the Orion Population, Lick Observatory Bulletin, No. 1111

Ishihara, D.,Wada, T., Watarai, H., et al. 2003, Proc. SPIE, 4850, 1008

Ishihara, D., Wada, T., Onaka, T., et al., 2006, PASP, 118, 324

Ishihara, D., Onaka, T., Kaneda, H., et al., 2007, PASJ, 59, S443

Ishihara, D., Onaka, T., Kataza, H., et al., 2010, A&A, 514, A1

Ita, Y., Matsuura, M., Ishihara, D., et al., 2010, A&A, 514, A2

Jones, B. F. & Herbig, G. H., 1979, AJ, 84, 1872

Kataza, H., Alfageme, C., Cassatella, A., et al., 2010, AKARI/IRC All-Sky Survey Point Source Catalogue Version 1.0 Release Note

Kawada, M., Baba, H., Barthel, P. D., et al., 2007, PASJ, 59, S389

Kenyon, S. J., & Hartmann, L., 1995, ApJS, 101, 117

Kenyon, S. J., Gómez, M., & Whitney, B. A., 2008, Handbook of Star Forming Regions, Volume I, 405

Kitamura, Y., Momose, M., Yokogawa, S., et al., 2002, ApJ, 581, 357

Lada, C. J., 1987, in *Star Forming Regions*, IAU Symposium, 115, eds. M. Peimbert & J. Jugaku, 1

Lada, E. A., Bally, J., & Stark, A. A. 1991, ApJ, 368, 432

Landsman, W. B., 1993, Astronomical Data Analysis Software and Systems II, 246

Le Bertre, T., Tanaka, M., Yamamura, I., & Murakami, H., 2003, A&A, 403, 943

Li, J. Z. & Hu, J. Y., 1998, A&AS, 132, 173

Lorente, R., Onaka, T., Ita, Y., et al., 2007, AKARI IRC Data User Manual Version 1.3

Luhman, K. L., Whitney, B. A., Meade, M. R., et al., 2006, ApJ, 647, 1180

Luhman, K. L., Mamajek, E. E., Allen, P. R., & Cruz, K. L., 2009, ApJ, 703, 399

Luhman, K. L., Allen, P. R., Espaillat, C., Hartmann, L., & Calvat, N., 2010, ApJS, 186, 111

Magazzù, A., Martín, E. L., Sterzik, M. F., et al., 1997, A&AS, 124, 449

Mendoza V., & Eugenio, E., 1966, ApJ, 143, 1010

Mizuno, A., Onishi, T., Yonekura, Y., et al., 1995, ApJ, 445, L161

Murakami, H., Baba, H., Barthel, P., et al., 2007, PASJ, 59, S369

Neugebauer, G., Habing, H. J., van Duinen, R., et al., 1984, ApJ, 278, L1

Neuhäuser, R., Sterzik, M. F., Schmitt, J. H. M. M., Wichmann, R., & Krautter, J., 1995a, A&A, 295, L5

Neuhäuser, R., Sterzik, M. F., Schmitt, J. H. M. M., Wichmann, R., & Krautter, J., 1995b, A&A, 297, 391

Neuhäuser, R., Sterzik, M. F., Schmitt, J. H. M. M., Wichmann, R., & Krautter, J., 1995c, A&A, 299, L13

Onaka, T., Yamamura, I., de Jong, T., et al., 1998, Ap&SS, 255, 331

Onaka, T., Matsuhara, H., Wada, T., et al., 2007, PASJ, 59, S401

Onishi, T., Mizuno, A., Kawamura, A., Tachihara, K., & Fukui, Y., 2002, ApJ, 575, 950

Padgett, D. L., Cieza, L., Stapelfeldt, K. R., et al., 2006, ApJ, 645, 1283

Rebull, L. M., Padgett, D. L., McCabe, C. -E., et al., 2010, ApJS, 186, 259

Reipurth, B., 2008, Handbook of Star Forming Regions, Volume II, 847

Sawada, T., Ikeda, N., Sunada, K., et al., 2008, PASJ, 60, 445

Siess L., Dufour E., & Forestini M., 2000, A&A, 358, 593

Silverstone, M. D., Meyer, M. R., Mamajek, E. E., et al., 2006, ApJ, 639, 1138

Skrutskie, M. F., Cutri, R. M., Stiening, R., et al., 2006, ApJ, 131, 1163

Strom, K. M., Strom, S. E., Edwards, S., Cabrit, S., & Skrutskie, M. F., 1989, AJ, 97, 1451

Szczerba, R., Siódmiak, N., Stasińska, G., et al., 2007, A&A, 469, 799

Tachihara, K., Toyoda, S., Onishi, T., et al., 2001, PASJ, 53, 1081

Tachihara, K., Neuhäuser, R., Kun, M., & Fukui, Y., 2005, A&A, 437, 919

Takita, S., Kitamura, Y., Kataza, H., et al., 2009, PASJ, 61, 291

Takita, S., Kataza, H., Kitamura, Y., et al., 2010, A&A, 519, A83

Tanabé, T., Sakon, I., Cohen, M., et al., 2008, PASJ, 60, S375

Voges W., Aschenbach B., Boller T., et al., 1999, A&A, 349, 389

Voges W., Aschenbach B., Boller T., et al., 2000, IAU Circ., 7432, 3

Yamamura, I., Makiuti, S., Ikeda, N., et al., 2010, AKARI/FIS All-Sky Survey Bright Source Catalogue Version 1.0 Release Note

Young, C. H., Jørgensen, J. K., Shirley, Y. L., et al., 2004, ApJS, 154, 396

Yun, J. L., & Clemens, D. P., 1990, ApJ, 365, L73

Verdugo, E., Yamamura, I., Pearson, C., et al., 2007, AKARI FIS Data User Manual Version 1.3

Walter, F. M., Kuhi, L. V., 1981, ApJ, 250, 254

Walter, F. M., Brown, A., Mathieu, R. D., Myers, P. C., & Vrba, F. J., 1988, AJ, 96, 297

Wang, Y., Evans, II, N. J., Zhou, S., & Clemens, D. P., 1995, ApJ, 454, 217

Weingartner, J. C. & Draine, B. T., 2001, ApJ, 548, 296

White, R. J., & Basri, G., 2003, ApJ, 582, 1109

Wichmann, R., Krautter, J., Schmitt, J. H. M. M., et al. 1996, A&A, 312, 439

Wyatt, M. C., Dent, W. R. F., & Greaves, J. S., 2003, MNRAS, 342, 876

Zacharias, N., Urban, S. E., Zacharias, M. I., et al., 2004, AJ, 127, 3043

Zacharias, N., Finch, C., Girard, T., et al., 2010, AJ, 139, 2184